Title
Loop Condensation in Quantum Dimer Models

Author
Herdman, Christopher Mott

Publication Date
2011

Peer reviewed|Thesis/dissertation

Loop Condensation in Quantum Dimer Models

by

Christopher Mott Herdman

A dissertation submitted in partial satisfaction of the

requirements for the degree of

Doctor of Philosophy

in

Physics

in the

Graduate Division

of the

University of California, Berkeley

Committee in charge:

K. Birgitta Whaley, Co-Chair

Ashvin Vishwanath, Co-Chair

Robert A. Harris

Joel E. Moore

Fall 2011

Loop Condensation in Quantum Dimer Models

Abstract

Loop Condensation in Quantum Dimer Models

by

Christopher Mott Herdman

Doctor of Philosophy in Physics

University of California, Berkeley

K. Birgitta Whaley, Co-Chair

Ashvin Vishwanath, Co-Chair

Topologically ordered phases of matter are quantum liquids with a non-local quantum order. Because of their unique properties due to the non-local quantum entanglement present in these phases, topological phases have been proposed as the basis of a physically fault-tolerant quantum computer. The formation of such topological order is well understood in terms of the mechanism of loop condensation in systems with loop-like degrees of freedom. Certain quantum dimer models posses topologically ordered dimer liquid ground states and can be mapped to loop models. In this dissertation we present a study of the geometric properties of the loop condensates of quantum dimer models and related models using classical Monte Carlo as well as ground state quantum Monte Carlo calculations. Additionally, we present an approach for the robust experimental generation of a topologically ordered phase in a system of neutral atoms trapped in an optical lattice.

Contents

1 Introduction **1**
1.1 Quantum Computation 1
1.2 Topologically ordered phases of matter 2
1.3 Loop Condensation 6
1.4 Quantum dimer models 11

2 Numerical Methods **16**
2.1 Classical Monte Carlo Sampling 16
2.2 Quantum Monte Carlo 20
2.2.1 Introduction 20
2.2.2 Continuous-time finite temperature world-line QMC 21
2.2.3 Path Integral Ground State Monte Carlo 24
2.2.4 Monte Carlo Updates for Sampling $\sigma_{\alpha\beta}$ 25
2.3 Proof of principle results for the QDM 31

3 Loop condensation in the triangular QDM **34**
3.1 Mapping a dimer model to a loop model 34
3.2 The dimer liquid at the RK point 36
3.3 Loop order in dimer crystal phases 38
3.4 Interacting dimer loop liquid 42
3.5 d-isotopic quantum loop gas in the triangular lattice QDM 45
3.6 Off-diagonal loop operators in the triangular lattice QDM 47
3.7 The QDM on the triangular lattice away from the RK point 48

4 Loop condensed phases on the square lattice **51**
4.1 Loop condensation from local constraints 51
4.2 Toric code 54
4.3 Square lattice QDM 55
4.4 Fully packed loop model 56

5 QDM with a 3-dimer constraint **59**
5.1 Introduction 59
5.2 Phase diagram 61
5.3 Future Work 62

6 Stroboscopic topological protection **65**
6.1 Introduction 65
6.2 Effective Hamiltonian Evolution 67
6.3 Simulated Thermalization 69
6.3.1 Themalization from non-unitary dynamics 70
6.3.2 Generating thermalization from dissipative pseudospins 72
6.4 Optical Lattice Implementation 76
6.5 Sources of Errors 78
6.6 Outlook 78

Preface

The structure of this dissertation is the following:

- Chapter 1 is a brief review of the relevant background of topological phases, quantum computation, loop condensation, and quantum dimer models.
- Chapter 2 is an overview the the numerical methods used here, in particular classical and quantum Monte Carlo methods. This chapter describes in detail the path integral ground state quantum Monte Carlo code for locally constrained systems that was developed by the author.
- Chapter 3 is a study of loop condensation in the triangular lattice quantum dimer model. Sections 3.1-3.6 is a discussion of classical Monte Carlo calculations of dimer wave functions that was published as reference 49. Section 3.7 presents quantum Monte Carlo calculations that have not appeared elsewhere.
- Chapter 4 presents a classical Monte Carlo study of loop condensed states on the square lattice.
- Chapter 5 presents a quantum Monte Carlo study of the quantum 3-dimer model on the triangular lattice.
- Much of chapter 6 appeared in reference 50 and was done in collaboration with co-authors. Section 6.3 is a greatly expanded version of what appeared in reference 50 and is primarily this author's work.

Chapter 1

Introduction

This chapter gives an overview of the background for quantum computation, topological phases, loop condensation, and quantum dimer models, as relevant to the rest of this dissertation.

1.1 Quantum Computation

Certain classes of problems can not be efficiently solved by any known algorithm that can run on a traditional computer. A famous example of such a problem is the prime factorization of large numbers: the best known classical algorithms require a computation time that grows exponentially with the number of digits in the number. This computational inefficiency is taken advantage of by many encryption schemes used for internet security. However, in the past few decades, several algorithms that take advantage of the law of quantum mechanics have been formulated which would allow for the efficient solution of such "unsolvable" problems [113, 93].

The potential power of quantum algorithms has sparked great interest in building a quantum computer, and much progress has been made towards that goal. The standard paradigm of quantum computation relies on the storage and manipulation of quantum information in localized quantum bits (qubits). The quantum information stored in ordinary qubits fragile, as interactions with the surrounding environment tend to lead to decoherence and loss of the quantum information. The standard approach to building a fault-tolerant quantum computer is to run quantum software that corrects errors as they occur; however, running error correction algorithms in addition to the desired computational algorithm requires extra quantum computational resources that, at the present time, are exceedingly scarce [98, 99].

An alternative approach to designing a fault-tolerant quantum computer is to design it to be physically robust, such that no error-correcting algorithms are required. This idea can be viewed as a quantum analog of the robustness of classical computers, where information is stored and processed somewhat non-locally in a robust phase of matter a such that it is not sensitive to noise and thermal fluctuations. While classical information can be robustly stored

in conventionally-ordered phases of matter (such in one of two ferromagnetic states of an Ising model), the quantum coherence of a many-body system in a conventional, symmetry broken phase of matter would be fragile, as local noise could couple to the local order parameter and cause decoherence.

The solution, originally proposed by Alexi Kitaev and Michael Freedman, is to store and manipulate quantum information non-locally in a quantum liquid state with no-local ordering [64, 42, 43]. To store and process quantum information, such a liquid state must have a degenerate ground state (analogous to a classical magnetic bit) and an energy gap to excitations which may cause errors. Topologically-ordered phases of matter fit these requirements, and Freedman and Kitaev proposed storing and manipulating quantum information in the many-body state of a topological phase [23, 90].

1.2 Topologically ordered phases of matter

Topologically ordered phases of matter are 2+1 dimensional quantum liquids with a non-local quantum order [132, 90]. Unlike conventionally ordered phases, a topological phase has no broken ordinary symmetry, and therefore no characteristic local order parameter which arises from a broken symmetry. Despite this lack of symmetry breaking, topologically ordered ground states have a degeneracy on surfaces of non-trivial topology, which is due to a non-local quantum entanglement; this contrasts with a conventional liquid ground state, which would be expected to be unique.

There are several features of these phases that make them of particular interest for quantum information processing:

- They are quantum liquids with vanishing local correlation functions and no conventional broken symmetry
- The ground state has a robust degeneracy
- There is a finite energy gap to excitations
- The low energy excitations are anyonic quasiparticles with fractional statistics

We will now discuss how topological order, and consequently these properties, arise in systems with loop-like degrees of freedom.

Loop operators in topological phases

Consider a quantum system with a set of loop operators $\{L_\ell^\alpha\}$ that commute with the Hamiltonian:

$$\left\{L_\ell^\alpha\right\} : \left[L_\ell^\alpha, H\right] = 0, \forall \alpha, \ell.$$

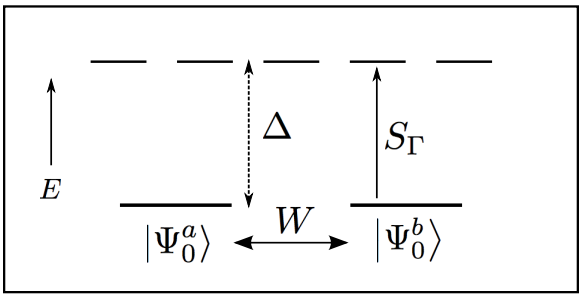

Figure 1.1: Schematic energy spectrum of a model with a topologically ordered ground state. W is a loop operator which connects degenerate ground states, and S_Γ is an open string operator that creates quasiparticle excitations.

Here, α labels the type of loop operator and ℓ defines a closed spatial loop. The symmetries of a liquid phase suggests that the action of these operators depend only on the topological properties of the loops, not their microscopic details; therefore, their action is the same for two loops that are related by isotopy. For contractable loops, these operators commute, and on the sphere there is a single non-degenerate ground state:

$$\left[L_\ell^\alpha, L_{\ell'}^\beta\right] = 0, \quad (\ell, \ell') \in \{\text{contractable loops}\}\,.$$

However, on a torus (or surfaces of higher genus), there are loop operators $W_{1,2}^\alpha$, that are associated with non-contractible loops, $c_{1,2}$ that wind around one of axes of the torus; in general these loop operators may not commute:

$$\left[W_1^\alpha, W_2^\beta\right] \neq 0, \quad \text{for some}\,(\alpha, \beta)\,.$$

In the simplest cases, this distinction is traced to to the intersection number of the loops, $I(\ell, \ell')$: if ℓ or ℓ' is contractable, then $I(\ell, \ell')$ is even, but $I(c_1, c_2)$ is odd.

If $|\Phi_0^a\rangle$ is a ground state on the torus and is an eigenstate of W_1^α with eigenvalue w_1^a, then $|\Phi_0^a\rangle$ is not an eigenvalue of W_2^β, and therefore $W_2^\beta|\Phi_0^a\rangle$ is another orthogonal ground state (note that since $[W_2^\beta, H] = 0$, $W_2^\beta|\Phi_0^a\rangle$ is also a ground state). We see then that the existence of non-commuting winding loop operators that commute with the Hamiltonian leads to a ground state degeneracy (see figure 1.1). The degeneracy of this ground state subspace is determined by the algebra that is represented by $\{W_{1,2}^\alpha\}$.

String operators

Associated with every closed loop operator L_ℓ^α is an open string operator $S_{\Gamma_{i,j}}^\alpha$ which commutes with the Hamiltonian everywhere except at the endpoints of $\Gamma_{i.j}$, (i, j). On a surface Σ with a boundary $\partial\Sigma$, for certain choices of boundary conditions, the boundary Hamiltonian

H_b will commute with all $S^{\alpha}_{\Gamma_{i,j}}$ such that if $\Gamma_{i,j}$ terminates on the boundary, then $S^{\alpha}_{\Gamma_{i,j}}|\Phi^a_0\rangle$ remains a ground state. If Σ has multiple disconnected boundaries, $\{\partial\Sigma_a\}$, then string operators starting and ending with different boundaries will not commute with non-contractible loop operators, and there will be a ground state degeneracy.

If $\Gamma_{i.j}$ terminates in the bulk, then $[S^{\alpha}_{\Gamma_{i,j}}, H] \neq 0$ and $S^{\alpha}_{\Gamma_{i,j}}$ will create quasiparticle excitations at (i, j). A closed loop operator can then be viewed as virtually creating a pair of quasiparticles, transporting one around the loop and annihilating them. If ℓ encloses the endpoint i of $\Gamma_{i,j}$, then L^{β}_{ℓ} can be viewed as braiding a quasiparticle around the particle at i. For bosons or fermions, an exchange generates a statistical phase of ± 1, so a braid, which is a double exchange, is the identity. If $[S^{\alpha}_{\Gamma_{i,j}}, L^{\beta}_{\ell}] \neq 0$, then this braiding operation is not the identity, and there is some statistical phase associated with the braiding operation. Consequently, the quasiparticles have fractional statistics, and the quasiparticles are called "anyons". If a braiding operation simply generates a statistical phase then different braiding operations will commute; in certain models braiding operations don't commute, and the quasiparticles will then have non-Abelian statistics.

Types of topological phases

Topological phases my be classified according to the types anyonic of quasiparticles present in the low energy spectrum [90]. Such anyonic quasiparticles have a well defined behavior when two anyons undergo fusion or are braided (see figure 1.2), and these properties can be used to classify the nature of the topological order. If all braiding operations commute, then the braiding statistics and the topological phase are classified as Abelian; if some braiding operations don't commute, then the phase is said to have non-Abelian topological order. Additionally, the ground state degeneracy on a torus is determined by the types of anyonic quasiparticles present in the spectrum; in the simplest cases, the degeneracy of the ground state on a torus is equal to the number of quasiparticle types (including the vacuum).

The simplest type of topological order, which will be the focus of the rest of this dissertation is so-called Z_2 topological order [64]. This topological order is described by the deconfined phase of a discrete Z_2 gauge theory [69]. In a model with a Z_2 topologically ordered ground state, there are two basic types of quasiparticles, the electric **e**-type particles and magnetic **m**-type particles ("electric" and "magnetic" refer to the electric and magnetic charges in the gauge theory). Both **e** and **m** particles independently act as bosons under exchange and braiding, however, a mutual braiding operation, where an **e** is braided around and **m** (or vice-versa) generates a statistical phase of -1. Thus the self statistics of these particles are bosonic, but their mutual statistics are fractional; they are thus relative Abelian anyons. There are four fundamental topological charges in this case: $\{\mathbb{1}, \mathbf{e}, \mathbf{m}, \mathbf{em}\}$, where $\mathbb{1}$ is the trivial (vacuum) charge and **em** is a bound state of an **e** and **m**. Consequently, there is a four-fold ground state degeneracy of a Z_2 topological phase.

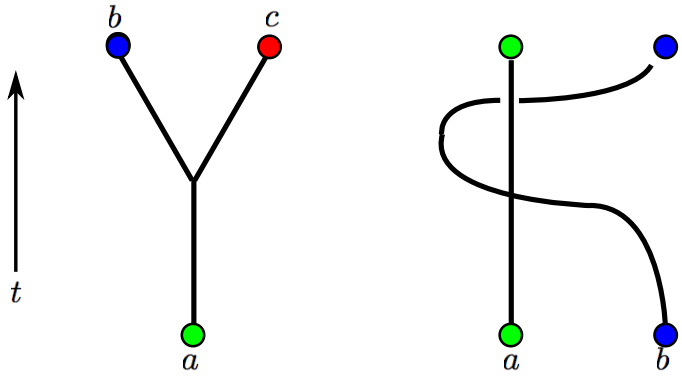

Figure 1.2: Illustration of the worldlines anyonic quasiparticles undergoing fusion and braiding processes in a topologically ordered phase.

Low energy Hilbert space

So far we have only discussed the abstract properties of the loop algebra which underlies a topological phase. To understand a microscopic model which possess topological order, we consider a microscopic Hilbert space which may represent this loop algebra. In the simplest models, the Hilbert space has degrees of freedom that live on the links of the lattice and comprises closed loop coverings of the lattice. Here the ground state is a fluctuating loop gas and the operators L_ℓ^α create or measure loops in the loop gas. To generate phases with non-Abelian statistics, we must generalize the loop Hilbert space to a string-net Hilbert space in which the links may have more than two labels, and with fusion rules which define how labels can meet at the vertices [78].

Topological quantum computation

The model of topological quantum computation proposed by Kitaev and Freedman takes advantage of these features of topologically ordered phases [64, 42]. The degeneracy of the ground state allows for quantum information to be stored in the ground state subspace. The liquid nature of the ground states ensure that the splitting of this degeneracy by local perturbations is exponentially small in the system size. Logical operations are performed by the action of loop operators, which act to braid anyons around non-contractable loops in the system. The action of these braids only depends on the homotopy class of the loop formed, not the fine details of the path of the braid, and therefore logical operations are robust to local deformations of the path. Errors due to perturbations which cause virtual tunneling between ground states are exponentially suppressed due to the finite energy gap to the creation of quasiparticles, and the non-local nature of the loop operators that cause the transitions.

Characterization of topological order

Given the lack of a local order parameter that signifies topological order, detecting topological order in a state (analytically, numerically or experimentally) is challenging. One may indirectly demonstrate the existence of topological order by detecting each of the features enumerated above: a lack of broken symmetry, a robust & finite degeneracy, a finite energy gap, and anyonic quasiparticles. A more direct measure exists in the entanglement entropy: topological ordered phases have a universal constant subleading term in the bipartite entanglement entropy [65, 79]. This constant, known as the topological entanglement entropy, gives a signature not only of the existence of topological order, but the type of topological order present. While entanglement entropy is generally difficult to calculate numerically, recently computational methods have been developed that allow for computing topological entanglement entropy in complex non-soluble lattice models [56, 45, 82].

1.3 Loop Condensation

Quantum models with loop-like degrees of freedom may posses a variety of phases, including ordered loop crystalline phases as well as disordered, fluctuating loop gas phases. The formation of fluctuating loops on all length scales is known as loop condensation; a loop condensate is a scale-invariant, dense loop phase with loops fluctuating on all length scales. The presence of large fluctuating loops may generate the non-local entanglement present in a topological phase, and consequently, loop condensation is a mechanism for the generation of topological order [32, 30, 78, 39]. Here we will discuss the properties of loop condensates.

Classical loop models

Here we consider a classical loop model, where the configuration space consists of closed loop coverings of a lattice (figure 1.3). Such a loop covering may be fully-packed, with every vertex of the lattice touched by a loop, or dilute, with some vertices that are not touched by any loop. Such a model may have disordered loop phases as well as ordered loop phases that break some of the symmetries of the lattice.

Defining the loop density on a link l of the lattice to be n_l, we can consider the loop density-density correlation function,

$$C\left(\vec{r}\right) = \langle n_l n_{l'} \rangle - \langle n_l \rangle \langle n_{l'} \rangle ,$$

where $\vec{r}$ is the displacement between links l and l'. In an ordered phase, $C(\vec{r})$ will detect the symmetry breaking of the loop density, and remain finite. In a disordered loop phase, $C(\vec{r})$ will decay to zero as $|\vec{r}| \to \infty$. We can distinguish two types of disordered loop gases: critical loop gases where $C(\vec{r})$ decays as a power law,

$$C\left(\vec{r}\right) \sim r^{-\nu} \tag{1.1}$$

and disordered loop gases with exponentially decaying correlations,

$$C\left(\vec{r}\right) \sim \exp\Big(-\frac{r}{\xi}\Big),$$

where $r = |\vec{r}|$.

To fully describe a loop configuration, we must consider the loop distribution $P(s)$, the probability a loop has length s. In a short-looped phase, this distribution will decay exponentially,

$$P(s) \sim \exp\left(-\frac{s}{s_0}\right),$$

where s_0 is the characteristic loop length. In a dilute loop phase with vanishing loop density, $C\left(r\right)$ will also decay exponentially. However, in a dense disordered loop phase, if there are loops on all length scales, the loop distribution can be scale-invariant and therefore decay as a power law:

$$P\left(s\right) \sim s^{-\tau}. \tag{1.2}$$

This is what we will refer to as a scale-invariant loop liquid, independent of the nature of the density-density correlations.

In a scale-invariant loop liquid, the scaling of the length of a loop with it's radius $R(\ell)$ determines the fractal dimension D_f of the loops:

$$s\left(\ell\right) \sim R\left(\ell\right)^{D_f}.$$

These geometric exponents may be related by a scaling relation to the two-loop correlation function $G_2(r)$ which determines that probability that two points separated by a distance r lie on the same loop [107]. Since $G_2(r)$ is fundamentally a non-local correlation function (since's determined the existence of single loop connecting the points), this power law may hold even in the absence of local correlations. Consequently, even in loop models with exponentially decaying density-density correlations, there may be a geometric critical exponent describing the fractal behavior of the loop gas, was well as the loop distribution function. The exponent x_2 that governs the power-law decay $G_2\left(r\right) \sim r^{-2x_2}$ determines the geometric exponents τ and D_f [107, 75]:

$$D_f = 2 - x_2, \quad \tau = 1 + \frac{2}{2 - x_2}.$$

The novel behavior of quantum loop liquids arises in phases with scale-invariant loop distributions. The existence of fluctuating loops on all lengths scales in a quantum loop model generates the non-local quantum entanglement that is present in a topologically ordered phase. A loop condensed phase is a quantum loop model with a scale-invariant loop distribution. Therefore, we will study the geometric exponents of loop condensates, as characteristic feature of these models.

Quantum Loop Models

The simplest example of a topological phase is described by a quantum loop gas [30, 32, 39, 64]. Consider a loop algebra with the elements $\{L^x_\ell, L^z_{\bar{\ell}}\}$:

$$L^x_\ell L^z_{\bar{\ell}} = (-1)^{I(\ell,\bar{\ell})} L^z_{\bar{\ell}} L^x_\ell \tag{1.3}$$

where $I(\ell,\bar{\ell})$ is the intersection number of ℓ and $\bar{\ell}$. For contractible loops, $I(\ell,\bar{\ell})$ is even, so $[L^x_\ell, L^z_{\bar{\ell}}] = 0$. However, two non-contractible loops on the torus may have an odd intersection number:

$$\begin{gathered} W^x_1 W^z_2 = -W^z_2 W^x_1, \quad W^x_2 W^z_1 = -W^z_1 W^x_2 \\ \left[W^x_1, W^x_2\right] = 0, \quad \left[W^z_1, W^z_2\right] = 0 \end{gathered} \tag{1.4}$$

where $W^{x,z}_{1,2}$ are loop operators that are associated with loops that wind around one of the non-trivial cycles of the torus, c_1, c_2. This algebra can be implemented in a Hilbert space of closed loop coverings of a lattice (see figure 1.3).

Here we consider a Hilbert space on a lattice, where the degrees of freedom are unoriented loop segments that live on the links of the lattice; each link is an Ising degree of freedom, occupied or unoccupied by a loop segment (or dimer). The Hilbert space comprises closed, non-intersecting loop coverings of the lattice. Defining the dimer creation/annihilation operators as d^+_l and d^-_l on a link l, we define the loop operator L^x_ℓ as a product over the links in ℓ

$$L^x_\ell \equiv \prod_{l\in\ell} \left(d^+_l + d^-_l\right).$$

Therefore L^x_ℓ creates the loop ℓ when acting on the vacuum, and considering $|\emptyset\rangle$ to be the empty lattice, a state $|\{\ell_i\}\rangle$ comprising a set of loops $\{\ell_i\}$ if formed from $|\emptyset\rangle$ by applying a product of L^x_ℓ operators:

$$\left|\{\ell_i\}\right\rangle = \prod_{\ell\in\{\ell_i\}} L^x_\ell \left|\emptyset\right\rangle.$$

We define $\bar{\ell}$ to live on the links of the dual lattice and define $L^z_{\bar{\ell}}$ as

$$L^z_{\bar{\ell}} \equiv \prod_{l\perp\bar{\ell}} 2\left(n^d_l - \frac{1}{2}\right),$$

where $n^d_l = d^+_l d^-_l$ is the dimer number operator. Loop configurations $|\{\ell_i\}\rangle$ are eigenstates of $L^z_{\bar{\ell}}$ with eigenvalues ± 1, and $L^z_{\bar{\ell}}$ measures the parity of the number of loops which intersect $\bar{\ell}$. Subsequently, L^x_ℓ and $L^z_{\bar{\ell}}$ satisfy the algebra defined by (1.3).

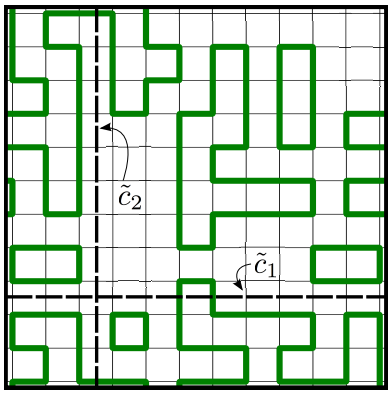

Figure 1.3: An examples of a loop covering of the square lattice

To form a liquid state, we can consider an equal-superposition of all loop coverings of a lattice in a given winding parity sector:

$$\Big|\Psi_{p_1,p_2}\Big\rangle = \sum_{\{\ell_i\}\in(p_1,p_2)} \Big|\{\ell_i\}\Big\rangle. \tag{1.5}$$

In (1.5), (p_1, p_2) defines the parity of the loop winding numbers along the two cycles of the torus. If $\{|\Psi_{p_1,p_2}\rangle\}$ are liquid states for which all correlation functions decay exponentially, then we can imagine that these states can not be distinguished by a local order parameter, since, no local operator can be sensitive to the winding number.

The winding numbers can be changed by ± 2 by a local operation which cuts and reconnected two non-contractable loops, however the parity of the winding number remains invariant under all such local operations. Therefore, the four states labeled by $\Psi_{\pm,\pm}$ are not only eigenstates of all $L^z_{\bar{\ell}}$, but also are $+1$ eigenstates of L^x_ℓ for contractable loops $\bar{\ell}$:

$$\begin{aligned} L^z_{\bar{\ell}}\Big|\Psi_{\pm,\pm}\Big\rangle &= \Big|\Psi_{\pm,\pm}\Big\rangle, \quad \text{for contractable loops } \bar{\ell} \\ L^x_{\ell}\Big|\Psi_{\pm,\pm}\Big\rangle &= \Big|\Psi_{\pm,\pm}\Big\rangle, \quad \text{for contractable loops } \ell \end{aligned}$$

For non-contractable loops, L^x_ℓ may change the winding parity, so the operators $W^x_{1,2}$ will connect the states $|\Psi_{p_1,p_2}\rangle$ which are eigenstates of $W^z_{1,2}$. Therefore we can see that the action of $\{W^{x,z}_{1,2}\}$ on $\{|\Psi_{p_1,p_2}\rangle\}$ satisfies the algebra given in (1.4):

$$\begin{aligned} W^x_1\Big|\Psi_{++}\Big\rangle &= \Big|\Psi_{-+}\Big\rangle \\ W^z_2\Big|\Psi_{-+}\Big\rangle &= -\Big|\Psi_{-+}\Big\rangle \end{aligned}$$

We have shown now how a ground state degeneracy can arise in a loop gas. If the non-contractible loop operators $\{W^{x,z}_{1,2}\}$ commute with the Hamiltonian and $\{|\Psi_{p_1,p_2}\rangle\}$ are energy

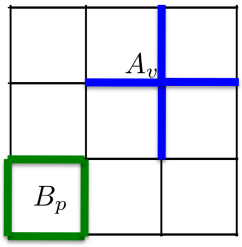

Figure 1.4: Illustration of the 4-body interactions in the toric code on the square lattice

eigenstates, then they will be degenerate. The robustness of this degeneracy depends on the liquid nature of these states: since $\{|\Psi_{p_1,p_2}\rangle\}$ are only distinguished by the non-local winding parity, we don't expect that a local perturbation can break this degeneracy in the thermodynamic limit.

Kitaev's Toric Code

The cannonical model with a quantum loop gas ground state is the toric code [64]:

$$H_{\mathrm{TC}} = -\lambda_e \sum_v A_v - \lambda_m \sum_p B_p,$$
$$A_v \equiv \prod_{j\in v} \sigma_j^z, \quad B_p \equiv \prod_{j\in p} \sigma_j^x.$$

Here, $\{\sigma_j\}$ are spin-1/2 degrees of freedom that are located on the links of a square lattice on a torus. v and p label the vertices and plaquettes of the lattice (see figure 1.4). The ground state, $|\Psi_{\mathrm{TC}}\rangle$, is an eigenstate of all A_v, i.e. $A_v|\Psi_{\mathrm{TC}}\rangle = +|\Psi_{\mathrm{TC}}\rangle$ for all v. These eigenstates of the vertex operators A_v have 0, 2 or 4 down spins touching each vertex. The ground state subspace can be interpreted in terms of a closed loop model by choosing a reference configuration $|R\rangle$ in the σ^z basis (from the subspace of $+1$ eigenstates of all A_v) that is defined as the empty loop state. For example, we may choose $|R\rangle$ to be the spin polarized state, $|\{\forall \sigma_j^z = +1\}\rangle$. Any other configuration in the $A_v = +1$ subspace can be reached by applying a product of closed loop operators:

$$|A\rangle \quad = \prod_{\ell\in\{\ell_A\}_R} L_\ell^x |R\rangle, \quad L_\ell^x \equiv \prod_{j\in\ell} \sigma_j^x, \tag{1.6}$$

where ℓ is a closed loop along the links and $\{\ell_A\}_R$ a closed loop covering of the square lattice. Since $[A_v, L_\ell^x] = 0, \forall v$, $|A\rangle$ is in the $A_v = +1$ subspace for all $\{\ell_A\}$. In this way, the closed loop covering defining $|A\rangle$ is $\{\ell_A\}_R$.

In general $\{\ell_A\}_R$ may comprise both contractible loops and non-contractible loops that wind around the torus. The winding sector $(w_1, w_2)_A$ is defined by the number of windings in $\{\ell_A\}_R$ about the two axes of the torus. Though the the plaquette term B_p causes fluctuations in these loop coverings, the parity of the winding number is conserved. The operator

$$W^z_{1,2} \equiv \prod_{j \in \tilde{c}_{1,2}} \sigma^z_j \tag{1.7}$$

measures the parity of the winding sector and commutes with $H_{\rm TC}$, where $\tilde{c}_{1,2}$ are loops that pass through the faces of the plaquettes and wind about one of the axes of the torus. Therefore, the ground state subspace is divided into four topological sectors that are defined by the parity of these two winding numbers.

The ground state $|\Psi_{\rm TC}\rangle$ is an equal superposition of all loop coverings in a given topological sector, and has fluctuating loops on all length scales. This quantum loop gas has no local order, but does possess topological order and is described by the deconfined phase of Z_2 gauge theory [64]. By considering the limit $\lambda_e \to \infty$, perturbations can drive transitions within the closed loop subspace [124]. For example addition of a magnetic field $H' = -h \sum_j \sigma^z_j$ will drive a transition to a spin polarized phase: for $h > |h_c|$ the ground state is a dilute loop crystal, and for $h < -|h_c|$ the ground state is a fully packed loop crystal. These transitions do not involve spontaneous symmetry breaking; we can alternately consider the effect of adding a loop interaction such as $H' = J \sum_{\langle i,j \rangle} \sigma^z_i \sigma^z_j$ which favors a rotational symmetry broken loop crystal for $J \gg \lambda_m$. We note that loop crystals need neither be dilute nor involve short loops; however, we may choose $|R\rangle$ to reflect the broken symmetries of the crystal phase, such that the resulting loop configuration will involve only short loops.

1.4 Quantum dimer models

In a hard-core dimer model, the degrees of freedom are dimers that live on the links of a lattice (see figure 1.5), and the hard-core constraint forbids more than a single dimer from touching each vertex [87]. Classical dimer models have be studied in statistical mechanics for decades and are known to display unusual disordered phases [5, 66, 29, 6]. Quantum dimer models (QDMs) were first presented in the context of spin-liquids [66, 29, 6]. Anderson proposed the idea of a resonating valence bond (RVB) liquid as a possible quantum liquid state in a frustrated magnet. In a RVB state, spin singlets are formed between nearby spins on the lattice and these singlets resonate around the lattice [6]. In the simplest model of a RVB state, the singlets are taken to be only between nearest-neighbors on the lattice; if one makes the further simplification that these valence bond coverings of the lattice are orthogonal, this reduces to a hard-core quantum dimer Hilbert space. While no naturally occurring material is known to be described by a quantum dimer model, because of their novel properties, there have been several proposals to experimentally engineer QDMs. In particular, certain spin and related Bose-Hubbard models map to QDMs when there is a large local energy penalty

which acts as the dimer constraint [9, 40]. Additionally, Josephson-Junction arrays have been proposed as experimental system where a QDM may be engineered [1, 52].

The quantum dimer model was first introduced on the square lattice by Rokhsar and Kivelson [106]. The Hilbert space of the QDM comprises fully-packed, non-colliding dimer coverings of a lattice, where all dimerizations are by definition orthogonal. The only way to rearrange dimers in a fully-packed dimerization without violating the hard-core constraint is to flip dimers around a closed loop on the links of the lattice, where the links in the loop are alternately occupied and unoccupied by dimers. Consequently, the minimal quantum dynamics give a resonance between the two orientations of dimers around a "flippable" plaquette. On a square lattice this corresponds to to parallel dimers on a square plaquette; on the triangular lattice a flippable plaquette is a length 4 rhombus lattice containing two parallel dimers (see figure 1.5).

The canonical QDM Hamiltonian on the square lattice [106] is:

$$H_{\mathrm{RK}} \equiv \sum_{\square} -t\Big(|\square\rangle\langle\square| + h.c.\Big) + v\Big(|\square\rangle\langle\square| + |\square\rangle\langle\square|\Big),$$

where the sum is over all square plaquettes and $|\square\rangle$ and $|\square\rangle$ represent the two possible flippable dimer configurations around a plaquette. The t term gives the dimers kinetic energy, and the v term represents an interaction between parallel dimers. In this work we will only consider $t > 0$. The QDM Hamiltonian was generalized to the triangular lattice, by Moessner and Sondhi [106, 89], where the minimal flippable loop is a rhombus:

$$H_{\mathrm{RK}} \equiv \sum_{p} -t\Big(|\diamondsuit\rangle\langle\diamondsuit| + h.c.\Big) + v\Big(|\diamondsuit\rangle\langle\diamondsuit| + |\diamondsuit\rangle\langle\diamondsuit|\Big). \tag{1.8}$$

In (1.8), the sum is over all rhombus plaquettes labeled by p (including different orientations in the case of the triangular lattice).

These local plaquette flip dynamics are not ergodic over all dimer configurations, and consequently split the Hilbert space into topological sectors that are defined by quasi-ergodicity of the local dynamics. We may define topological sectors by considering a loop c through the faces of plaquettes that winds around one of the directions of the torus. On the square lattice, we may label the links that cross c alternately as A and B; a plaquette flip (or any other local rearrangement) conserves $N_A - N_B$, where $N_{A,B}$ are the number of links of each type occupied by a dimer. Therefore, on the square, as well as other bipartite lattices, there is an extensive number of topological sectors labeled by $N_A - N_B$ for each of the two directions of the torus. However, on the triangular lattice, plaquette flips conserve merely the parity of the total number of dimers crossing c; on a torus, there are 4 such parity sectors, two for each of the directions around the lattice. There also exist a finite number of symmetry related "staggered" configurations with no flippable plaquettes, which are frozen under plaquette flip dynamics; it is believed that plaquette flips are ergodic in each parity sector excluding these staggered configurations [89].

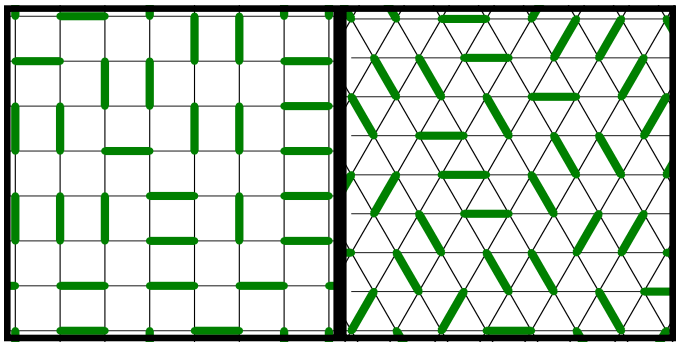

Figure 1.5: Examples of dimerizations of the square and triangular lattices. The thick green dimers are the physical degrees of freedom. The fully-packed, hard-core constraint requires that exactly one dimer touches each vertex of the lattice.

At the point $v = t$, the so-called RK point, the exact zero energy ground state of H_{RK} is the equal superposition of all dimerizations:

$$|RK\rangle = \sum_{C} |C\rangle \tag{1.9}$$

where the sum in equation (4.1) is taken over all dimer configurations C in a topological sector [106]. Consequently, the ground state at the RK point has an extensive degeneracy on the bipartite lattices but a finite degeneracy on non-bipartite lattices.

Since the norm of $|RK\rangle$ is equal to the partition function of the corresponding classical dimer model, expectation values of diagonal observables are identical to those of the classical dimer model. Dimer-dimer correlation functions of the square lattice classical dimer model decay as a power law, however, on the triangular lattice, dimer-dimer correlation functions are known to decay exponentially [31, 53]. Additionally, imaginary-time correlation functions of equation (4.1) can be related to dynamic correlation functions of a Monte Carlo simulation of the classical dimer model [48, 47, 20]. On the square lattice, such a calculation shows that the RK point is gapless, whereas on the triangular lattice H_{RK} has a finite gap [57]. Therefore, the bipartiteness of the lattice determines the nature of the liquid state at the RK point: on bipartite lattices this is a gapless critical dimer liquid, whereas on non-bipartite lattices the RK point is a gapped dimer liquid.

The bipartite (or non-bipartite) nature of the lattice also determines the ground state phase diagram surrounding the RK point. For both the square and triangular lattices, there are staggered states with no flippable plaquettes that are frozen under plaquette flips and therefore are zero energy eigenstates of H_{RK}. For $v > t$ these staggered states are the ground state, and both the square and triangular lattice QDMs in staggered crystalline phases. For $|v| >> t$ and $v/t < 0$, states with the maximum number of flippable plaquettes are favored. On the square lattice, there are only 4 such states that have a columnar ordering; consequently there is a columnar ordered crystalline phase for $v/t < v_c^s < 1$. On

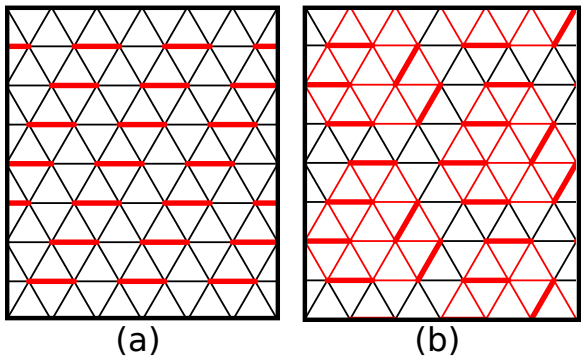

Figure 1.6: Reference dimer configurations that are representative of dimer crystals in the triangular lattice QDM. The thick red dimers represent the reference configurations, R_0. (a) A columnar configuration that defines R_{col}. (b) In the $\sqrt{12} \times \sqrt{12}$ phase dimers resonate in 12 site hexagons, colored red in this figure. The thick red dimers show the reference configuration $R_{\sqrt{12}}$.

the triangular lattice, there are 12 symmetry related columnar configurations (see figure 1.6) have the maximum number of flippable plaquettes, $N_l/6$, where N_l is the number of links in the lattice. Additionally, any configuration reached by translating dimers along any number of rows of a columnar configuration and by rotating all dimers in any number of columns of a columnar configuration, generates another maximally flippable dimerization[89]. References 89 and 103 show that quantum fluctuations favor the columnar order, and that for $v/t \lesssim -0.75$, $H_{\rm RK}$ has a columnar dimer crystalline ground state. The staggered and columnar phases break both translational and rotational symmetries of the lattice.

In addition to these static dimer crystals, the QDMs posses resonating dimer crystals that break translational symmetries but retain some of the rotational symmetries of the lattice. On the square lattice, the plaquette phase has parallel dimers that resonate on the face of plaquettes [77, 121]; there is recently evidence that the plaquette and columnar order overlap in part of the phase diagram of the square QDM [102]. On the triangular lattice there is a resonating dimer crystal phase with a 12-site unit cell (see figure 1.6) termed the $\sqrt{12} \times \sqrt{12}$ phase [89, 104, 103]. In this phase, dimers resonate within 24 link hexagons, and most translational symmetries are broken. However this phase retains a $\pi/3$ rotational symmetry of the lattice. Ralko et. al. showed that the dimer correlation functions are qualitatively reproduced by a wave function that is an equal superposition of all dimerizations within the hexagons [104, 84].

On the square lattice the resonating plaquette phase has been shown to persist up to the RK point [102, 77], and consequently the RK point is an isolated critical liquid point. However, on the triangular lattice, quantum Monte Carlo calculations by Moessner and Sondhi [89] and Ralko *et. al.* [103] demonstrate that the dimer liquid phase extends beyond the RK point for a finite range of v/t for $v < t$ and possesses Z_2 topological order. While

the QDM has been related to Z_2 gauge theory in the literature, no exact mapping from the deconfined phase of a Z_2 gauge theory to the dimer liquid is known [88, 84].

Chapter 2

Numerical Methods

This chapter presents a review the the numerical methods used in the remainder of this dissertation. Section 2.1 gives an overview of classical Monte Carlo methods, including Monte Carlo sampling of quantum dimer wave functions with local and directed loop updates, results of which are presented in later chapters. Section 2.2 gives an introduction to quantum Monte Carlo methods as well as the details of the path integral ground state quantum Monte Carlo code developed by the author.

2.1 Classical Monte Carlo Sampling

To compute the thermal average of an observable $\mathcal{O}$ in a classical lattice model, one needs to compute the sum

$$\langle \mathcal{O} \rangle = \frac{1}{Z} \sum_{\alpha} \mathcal{O}_{\alpha} e^{-\beta E_{\alpha}}, \quad Z = \sum_{\alpha} e^{-\beta E_{\alpha}} \tag{2.1}$$

where α labels the classical configuration, β is the inverse temperature, and Z is the partition function. Since the size of the classical configuration space grows exponentially with the number of degrees of freedom in the system (and therefore exponential in the square of the linear dimension of a 2D lattice model), performing the sum quickly becomes infeasible with increasing system size.

Similarly, to compute the expectation value of a diagonal operator $\hat{\mathcal{O}}$ in a known wavefunction in a lattice system ψ one needs to compute

$$\left\langle \psi \mid \hat{\mathcal{O}} \mid \psi \right\rangle = \frac{1}{Z} \sum_{\alpha} \mathcal{O}_{\alpha} \left| \psi \left(\alpha \right) \right|^2, \quad Z = \sum_{\alpha} \left| \psi \left(\alpha \right) \right|^2 \tag{2.2}$$

Again, since the Hilbert space grows exponentially with the number of degrees of freedom, direct computation of this sum can only be performed for relatively small lattice systems.

As we are often interested in the behavior of the system in the thermodynamic limit, a method whose computational resources scale more slowly (i.e. polynomially) with system size is preferred.

Since $e^{-\beta E_\alpha}/Z$ and $|\psi(\alpha)|^2/Z$ are non-negative, we can treat them as a probability distribution, $\Pi(\alpha)$. To efficiently compute expectation values, we may choose a statical sample of configurations $\{\alpha\}_{\Pi(\alpha)}$, where the probability of choosing a configuration α is proportional to $\Pi(\alpha)$. Accordingly, expectation values can be estimated by computing

$$\langle \mathcal{O} \rangle_{\mathrm{MC}} = \sum_{\{\alpha\}_{\Pi(\alpha)}} \mathcal{O}_\alpha \tag{2.3}$$

For a sufficiently large statistical sample $\{\alpha\}_{\Pi(\alpha)}$ with N_c configurations, we expect that the error in the statistical estimator $\langle \mathcal{O} \rangle_{\mathrm{MC}}$ to decay as $1/\sqrt{N_c}$.

To generate the statistical sample $\{\alpha\}_{\Pi(\alpha)}$, we may use a Markov chain Monte Carlo method, where one generates configurations in the sample sequentially [13, 83]. The statistical sample of configuration generated is therefore an ordered set of configurations: $\{\ldots, \alpha_{i-1}, \alpha_i, \alpha_{i+1} \ldots\}$. Here a subsequent configuration will be generated from the previous configuration by attempting an appropriate update to part of the configuration. We will define one Monte Carlo update as N_{MC} attempted updates to the system such after N_{MC} updates, updates have been attempted on most of the system. Since generally sequential configurations will be correlated, for computational efficiency, we often choose not to measure observables of every configuration, but only a subset of configurations separated by an interval n_{meas}; the frequency of making the measurements is tuned for computational efficiency based on the the autocorrelation time t_{ac} of the relevant observables.

From a given configuration α, we define the transition rate to a configuration β to be $\Gamma_{\alpha\beta}$.To ensure the statistical sampling remains in equilibrium with a probability distribution given by $\Pi(\alpha)$, total balance must be satisfied:

$$\sum_\beta \Gamma_{\alpha\beta} \Pi(\alpha) = \sum_\beta \Gamma_{\beta\alpha} \Pi(\beta) \tag{2.4}$$

The most convenient way to ensure total balance is to enforce detailed balance:

$$\Gamma_{\alpha\beta} \Pi(\alpha) = \Gamma_{\beta\alpha} \Pi(\beta) \tag{2.5}$$

Additionally, the set of updates used to generate subsequent configurations must be ergodic in the relevant configuration space to ensure all configurations can be reached by the Markov chain.

In particular, we use a Metropolis walk to generate such a Markov chain. The Metropolis Monte Carlo method is as follows:

1. Given a configuration α_i, choose a new configuration β with probability $W_{\alpha_i\beta}$

2. Compute the acceptance probability:

$$P_{acc} = \min\left(\frac{W_{\beta\alpha_i}}{W_{\alpha_i\beta}}\frac{\Pi(\beta)}{\Pi(\alpha_i)}, 1\right) \tag{2.6}$$

3. Choose a random number $0 \leq r < 1$

   - If $r < P_{acc}$, accept the transition and set $\alpha_{i+1} = \beta$
   - If $r \geq P_{acc}$, reject the transition and set $\alpha_{i+1} = \alpha_i$

4. If there have been n_{meas} updates since last measurement, measure observables of configuration α_{i+1}

5. Repeat

Monte Carlo sampling of dimer model wave functions with local updates

The simplest approach to Monte Carlo sampling of a dimer model wave function is to use local plaquette flip updates. Since plaquette flips are believed to be ergodic in each topological sector, we may generate subsequent dimer configurations by attempting a local plaquette flip. The simplest algorithm which satisfies detailed balance is

- Choose a plaquette p at random
- If p if flippable, flip the plaquette with probability $P_{\text{acc}} = |\psi(\alpha')|^2/|\psi(\alpha)|^2$
- Measure observables every n_{meas} updates

In the hard-core dimer model, the maximum number of flippable plaquettes on the triangular lattice is $N_p/6$, and therefore the acceptance rate is always less than 1/6 (at the RK point $\langle N_{fp}\rangle \approx 0.09$). We might wish to artificially improve the acceptance rate; one can do this by creating a table of flippable plaquettes, and updating this table after each update, since a plaquette flip only affects the neighboring plaquettes in the table. This approach guarantees that a flippable plaquette is always selected and therefore the acceptance rate can now approach unity. To maintain detailed balance the acceptance rate is changed to

$$P_{\text{acc}} = \frac{N_{fp}}{N'_{fp}}\frac{|\psi(\alpha')|^2}{|\psi(\alpha)|^2} \tag{2.7}$$

However there is some computational overhead in maintaining this list of flippable plaquettes. We find generally that the simple algorithm runs faster for the same statistical errors, despite the lower acceptance rate.

Directed-loop Monte Carlo sampling of dimer model wave functions

While local updates are efficient in a gapped liquid phase such as the RK point of the triangular lattice QDM, in a gapless phase such as the RK point of the square lattice QDM, the local update algorithm will have an autocorrelation time that diverges polynomially in the system size. Additionally, is systems where there are a lot of potential energy minima, a local update algorithm may get stuck near one minima and thus lose ergodicity. In these situations, a non-local update algorithm is necessary.

The directed-loop algorithm [123, 109] generates non-local updates in a dimer model by creating a pair of defects (a doubly occupied vertex and an unoccupied vertex) that violate the fully-packed, hard-core dimer constraint. One of these defects undergoes a directed random walk and, when the two defects coincide once again, this generates a new allowable dimerization, where the dimers have been flipped along the path of the path of the defect [109, 122]. To maintain detailed balance, the probabilities of choosing each direction on a given step of the random walk must satisfy the directed-loop equations [123].

Consider a step in the loop-update where the loop has entered a vertex v from link l. We define the probability of choosing link l' to exit the vertex as $P_{l,l'} \equiv t_{l,l'}/w_l$, where w_l is the weight of the configuration with the dimer on link l. Detailed balance and probability conservation require

$$\sum_{l'} t_{l,l'} = w_l, \qquad t_{l,l'} = t_{l',l} \tag{2.8}$$

For a given set of weights $\{w_l\}$, this leads to a set of directed-loop equations.

The simplest case of the directed-loop algorithm is for the RK wave function. The RK algorithm is a follows:

- Remove a random dimer from link l_0, creating two unoccupied vertices at v_0 & $\tilde{v_0}$
- Randomly choose a new link l_1 at v_0 to place a dimer
- Move to vertex v_1 connected to l_1 and remove the dimer from the previously occupied link
- Repeat until the loop closes back at $\tilde{v}_0$

At the RK point, this algorithm requires no "bouncing" or rejection so the the loop with always close without needed to retrace the previous path, generating a new configuration. In general we must generalize this algorithm to allow for different weights for placing dimers on different links, and thus must allow for bouncing. Here we consider sampling the square of the wavefuction $\Phi_\alpha(l) = \alpha^{-N_{fp}}$. There are three possible weights for a dimer to occupy a

link $\{w_0, w_1, w_2\}$, corresponding to a link with 0, 1 or 2 parallel dimers. The choice $w_2 = 1$, so $w_2 = w_1^2 = \alpha^4$ gives the following directed-loop equations:

$$1 = (6 - n_1 - n_2)\, t_{02} + n_1 t_{12} + (n_2 - 1)\, t_{22} + t_2^b \tag{2.9}$$

$$\alpha^2 = (6 - n_1 - n_2)\, t_{01} + n_2 t_{12} + (n_1 - 1)\, t_{11} + t_1^b \tag{2.10}$$

$$\alpha^4 = n_1 t_{01} + n_2 t_{02} + (6 - n_1 - n_2)\, t_{00} + t_0^b. \tag{2.11}$$

In (2.9-2.11), t_{pq} is the weight for a transition between links with p and q parallel dimers, n_p is the number of links with p parallel dimers at vertex v, and t_p^b is rate to "bounce" back from a link with p parallel dimers. Since these equations are underdetermined, we can choose a solution to (2.9-2.11) for which the bounce probabilities vanish at the RK point ($\alpha = 1$):

$$t_{00} = t_{01} = t_{02} = \tfrac{\alpha^4}{5}, \quad t_{12} = \tfrac{\alpha^2}{5}, \quad t_0^b = 0, \tag{2.12}$$

$$t_{11} = \begin{cases} \frac{\alpha^2\left(\alpha^2 n_1 - \left(1-\alpha^2\right)n_2 + 6\left(1-\alpha^2\right) - 1\right)}{5(n_1 - 1)} & n_1 > 1 \\ 0 & n_1 \leq 1 \end{cases}, \tag{2.13}$$

$$t_{22} = \begin{cases} \frac{\alpha^4 n_2 - \alpha^2\left(1-\alpha^2\right)n_1 + 6\left(1-\alpha^4\right) - 1}{5(n_2 - 1)} & n_2 > 1 \\ 0 & n_2 \leq 1 \end{cases}, \tag{2.14}$$

$$t_1^b = \begin{cases} \frac{\alpha^2\left(1-\alpha^2\right)(5-n_2)}{5} & n_1 = 1 \\ 0 & n_1 \neq 1 \end{cases}, \tag{2.15}$$

$$t_2^b = \begin{cases} 1 - \frac{\alpha^2}{5}\left(5\alpha^2 + (1-\alpha^2)n_1\right) & n_2 = 1 \\ 0 & n_2 \neq 1 \end{cases}. \tag{2.16}$$

We have compared the directed loop algorithm using this solution to (2.9-2.11) to the local update algorithm and is sufficiently efficient in the regimes studied.

2.2 Quantum Monte Carlo

2.2.1 Introduction

The approach of quantum Monte Carlo (QMC) methods [21, 22, 119, 62] is to statistically sample the partition function

$$Z = Tr\ e^{-\beta \hat{H}}$$

where $\hat{H}$ is the quantum Hamiltonian, and β is the inverse temperature. For $\beta \to \infty$, we will be sampling the quantum ground state; ground state expectation values:

$$\langle \hat{O} \rangle_{GS} = \lim_{\beta \to \infty} \frac{1}{Z} Tr\left(\hat{O} e^{-\beta \hat{H}}\right)$$

can be extracted in the limit $\beta \to \infty$.

The three general approaches to calculating ground state properties via QMC depend on the boundary conditions imposed on the imaginary time path integral:

- Periodic: Finite temperature worldline QMC (FTQMC) [21]
- Open: Green's Function QMC [125], Diffusion QMC [120, 120], Reptation QMC [10]
- Fixed: Path Integral Ground State QMC (PIGS) [110]

All of these methods can be formulated by dividing the path integral into a finite time step $\Delta\tau$ and then evaluating an approximate short time propagator $e^{-\Delta\tau H}$ between configurations at each time step [118, 119]. This leads to finite time-step error usually of order $(\Delta\tau)^2$; when a small $\Delta\tau$ is used to reduce finite time step errors, this often leads to slow convergence from the low acceptance rates of local updates. The disadvantages of finite time-step methods can be avoided in discrete quantum systems, where continuous-time versions of all of the above methods are available [28, 62, 108, 100].

2.2.2 Continuous-time finite temperature world-line QMC

We will follow the approach of Prokof'ev, Svistunov, and Tupitsyn [100]. For a discrete Hamiltonian $\hat{H} = \hat{V} + \hat{T}$ where $\hat{V}$ is the diagonal potential energy operator, and $\hat{T}$ is the off diagonal kinetic energy operator, we can choose a basis set $\{\alpha\}$ of the eigenstates of $\hat{V}$:

$$\hat{V}|\alpha\rangle = V_\alpha|\alpha\rangle.$$

Here we consider the kinetic energy to be a sum of local operators $\hat{Q}_s$, with negative matrix elements in the basis $\{\alpha\}$:

$$\hat{T} = \sum_s \hat{Q}_s, \quad \hat{Q}_s|\alpha\rangle = -q_{\gamma\alpha}(s)\,|\gamma\rangle.$$

The imaginary-time propagator in the interaction picture, $\hat{\sigma}(\tau) \equiv e^{\tau\hat{V}}e^{-\tau\hat{H}}$, obeys the following differential equation:

$$\frac{\partial}{\partial\tau}\hat{\sigma}(\tau) = -\hat{T}(\tau)\,\hat{\sigma}(\tau) \tag{2.17}$$

Repeated integration of (2.17) results in the formal expression for $\hat{\sigma}(\tau)$:

$$\hat{\sigma}(\tau) = 1 - \int_0^\tau d\tau \hat{T}(\tau) + \cdots + (-1)^m \int_0^\tau d\tau_m \cdots \int_0^{\tau_2} d\tau_1 \hat{T}(\tau_m) \cdots \hat{T}(\tau_1) + \ldots$$

$$\begin{aligned}\sigma_{\alpha\gamma} \equiv\ & \delta_{\alpha\gamma} + \sum_s \int_0^\beta d\tau q_{\gamma\alpha}(s) e^{\tau V_{\alpha\gamma}} + \ldots \\ & \cdots + \sum_{s_1 \ldots s_m} \int_0^\beta d\tau_m \cdots \int_0^{\tau_2} d\tau_1 q_{\alpha\nu}(s) e^{\tau_m V_{\alpha\nu}} \cdots q_{\lambda\gamma}(s) e^{\tau_1 V_{\lambda\gamma}} + \ldots \\ & (V_{\alpha\gamma} \equiv V_\alpha - V_\gamma)\end{aligned} \tag{2.18}$$

To evaluate thermodynamics properties, we want to statistically sample:

$$\begin{aligned}Z = Tr\ e^{-\beta\hat{H}} &= \sum_\alpha \langle\alpha| e^{-\beta\hat{H}} |\alpha\rangle \\ &= \sum_\alpha \langle\alpha| e^{-\beta\hat{V}} \hat{\sigma} |\alpha\rangle = \sum_\alpha e^{-\beta V_\alpha} \sigma_{\alpha\alpha}\end{aligned}$$

Accordingly, expectation values of operators $\hat{O}$ can be sampled from:

$$\begin{aligned}\langle\hat{O}\rangle &= \frac{1}{Z} Tr\left(\hat{O} e^{-\beta\hat{H}}\right) = \frac{1}{Z} \sum_\alpha \langle\alpha| \left(\hat{O} e^{-\beta\hat{V}} \hat{\sigma}\right) |\alpha\rangle \\ &= \frac{1}{Z} \sum_{\alpha,\gamma} O_{\alpha\gamma} e^{-\beta V_\gamma} \sigma_{\gamma\alpha}\end{aligned}$$

Additionally, we can take advantage of the imaginary time translation invariance. We can define the imaginary-time dependent expectation value $\left\langle \hat{O}(\tau) \right\rangle$:

$$\begin{aligned}\left\langle \hat{O}(\tau) \right\rangle &\equiv \frac{1}{Z} Tr\left(e^{-(\beta-\tau)\hat{H}} \hat{O} e^{-\tau\hat{H}}\right) \\ &= \frac{1}{Z} \sum_{\alpha,\gamma,\lambda} e^{-(\beta-\tau)V_\alpha} \sigma_{\alpha\lambda}(\beta-\tau) O_{\lambda\gamma} e^{-\tau V_\gamma} \sigma_{\gamma\alpha}(\tau)\end{aligned}$$

The imaginary-time averaged estimator of the thermodynamic estimator is then:

$$\left\langle \hat{O} \right\rangle_\beta \equiv \frac{1}{\beta} \int_0^\beta d\tau \left\langle \hat{O}(\tau) \right\rangle.$$

For operators $\hat{O}$ that are diagonal in the $\{\alpha\}$ we have:

$$\langle \hat{O} \rangle_\beta = \frac{1}{Z} \sum_\alpha \frac{1}{\beta} \int_0^\beta d\tau O(\tau) e^{-\beta V_\alpha} \sigma_{\alpha\alpha}.$$

This requires being able to statistically sample $\sigma_{\alpha\alpha}$, the diagonal propagator in the potential energy basis. At finite temperature we want to sample the sum:

$$\begin{aligned} \sum_\alpha e^{-\beta V_\alpha} \sigma_{\alpha\alpha} = & \sum_\alpha e^{-\beta V_\alpha} + \dots \\ \dots + \sum_\alpha \sum_{s_1 \dots s_m} & \int_0^\beta d\tau_m \cdots \int_0^{\tau_2} d\tau_1 e^{-(\beta-\tau_m)V_\alpha} q_{\alpha\nu}(s) e^{-\Delta\tau_m V_\nu} \cdots e^{-\Delta\tau_2 V_\lambda} q_{\lambda\alpha}(s) e^{\tau_1 V_\alpha} + \dots \end{aligned} \tag{2.19}$$

$(\Delta\tau_m \equiv \tau_m - \tau_{m-1})$

Looking at (2.19), we see that an arbitrary term in the sum contains m different $q_{\alpha\gamma}$'s, which correspond to m different off-diagonal matrix elements of $\hat{H}$. An individual term can be represented by a path integral of length β with m "kinks" corresponding to local virtual transitions between the two states connected by the matrix element $\hat{Q}_{\alpha\gamma}$. We can statistically sample this series by appropriately sampling imaginary time paths with different numbers, types, and locations of kinks such that their statistical weight is given by the appropriate term in (2.19).

Now consider taking the expectation value of one of the kinetic energy operators:

$$\begin{aligned} \left\langle \hat{Q}(r) \right\rangle_\beta &= -\frac{1}{Z}\frac{1}{\beta} \sum_{\alpha,\gamma,\lambda} \int_0^\beta d\tau e^{-(\beta-\tau)V_\alpha} \sigma_{\alpha\lambda}(\beta-\tau) q_{\lambda\gamma}(r) e^{-\tau V_\gamma} \sigma_{\gamma\alpha}(\tau) \\ &= -\frac{1}{Z}\frac{1}{\beta} \sum_\alpha \sum_{s_1} \int_0^\beta d\tau_r \int_0^{\tau_r} d\tau_1 e^{-(\beta-\tau_r)V_\alpha} q_{\alpha\nu}(r) e^{-\Delta\tau_2 V_\lambda} q_{\lambda\alpha}(s_1) e^{\tau_1 V_\alpha} - \dots \\ \dots &- \frac{1}{Z}\frac{1}{\beta} \sum_\alpha \sum_{s_1 \dots s_m} \int_0^\beta d\tau_m \cdots \int_0^\beta d\tau_r \cdots \int_0^{\tau_2} d\tau_1 \\ & \quad e^{-(\beta-\tau_m)V_\alpha} \cdots e^{-(\tau_n-\tau_r)V_\nu} q_{\nu\gamma}(r) \cdots e^{\tau_1 V_\alpha} + \dots \end{aligned} \tag{2.20}$$

We can see that (2.20) is proportional to the expectation value of the diagonal expectation value $\delta_{Q(r)}(\tau)$ which is equal to 1(0) if there is (not) a kink of type $\hat{Q}(r)$ at time τ. Therefore the total kinetic energy can be measured as [62]:

$$\left\langle \hat{T} \right\rangle_\beta = -\frac{1}{\beta} \langle n_{kinks} \rangle_\beta$$

2.2.3 Path Integral Ground State Monte Carlo

To calculate ground state properties, clearly we could take the limit of $\beta \to \infty$ and follow the method of the previous section. Because finite temperature QMC methods have periodic boundary conditions in imaginary time, on systems with periodic spatial boundary conditions, the closed world lines of particles have well defined imaginary time winding numbers. For example, by following a particle along it's imaginary time path, we can count the number of times it winds around one axis of a torus. The partition function will include imaginary time paths from all winding sectors, and therefore one must adequately sample from all winding sectors [46]. However, changing the winding sector generally requires a non-local update to a particle's word-line, since the topology of the world line must be changed. While non-local updating methods such as the worm and directed loop algorithms are available for a wide range of models [127], no such methods are known for systems with hard local constraints such as quantum dimer models [92].

However, zero temperature QMC methods do not have periodic boundary conditions in imaginary-time, and therefore there is no imaginary-time winding number. Local updates then may be ergodic, since there are no winding sectors that require non-local updates to access. Consequently, for QDMs, we will use a zero temperature path integral ground state method (PIGS) [110] which statistically samples ground state expectation values. Previous QMC studies of quantum dimer models in the literature have used other zero temperature methods, in particular Green's function QMC [103, 104, 105], diffusion QMC [120, 120], and reptation QMC [121].

For any wave function $|\Psi_T\rangle = \sum_\alpha c_\alpha |\alpha\rangle$ that is not orthogonal to $|\Psi_0\rangle$, $\langle\Psi_T|\Psi_0\rangle \neq 0$ we can reach reach the ground state by propagating $|\Psi_t\rangle$ in imaginary time:

$$|\Psi_0\rangle \propto \lim_{\tau\to\infty} e^{-\tau\hat{H}}|\Psi_T\rangle$$

To compute ground state properties, if we can sample $e^{-\tau\hat{H}}|\Psi_t\rangle$ for large τ, then we can calculate mixed estimates of operators by sampling:

$$\langle\hat{O}\rangle_M = \frac{\langle\Psi_T|\hat{O}|\Psi_0\rangle}{\langle\Psi_T|\Psi_0\rangle} = \lim_{\tau\to\infty} \frac{\langle\Psi_T|\hat{O}e^{-\tau\hat{H}}|\Psi_T\rangle}{\langle\Psi_T|e^{-\tau\hat{H}}|\Psi_T\rangle}$$

$$\begin{aligned}\langle\Psi_T|e^{-\tau\hat{H}}|\Psi_T\rangle &= \langle\Psi_T|e^{-\tau\hat{V}}\hat{\sigma}\left(\tau\right)|\Psi_T\rangle \\ &= \sum_{\alpha\gamma} c_\alpha^* c_\gamma e^{-\tau\hat{V}_\alpha}\sigma_{\alpha\gamma}\left(\tau\right)\end{aligned} \tag{2.21}$$

$$\begin{aligned}\langle\Psi_T|\hat{O}e^{-\tau\hat{H}}|\Psi_T\rangle &= \langle\Psi_T|\hat{O}e^{-\tau\hat{V}}\hat{\sigma}\left(\tau\right)|\Psi_T\rangle \\ &= \sum_{\alpha\gamma} c_\alpha^* c_\gamma e^{-\tau\hat{V}_\alpha}O\left(\alpha\right)\sigma_{\alpha\gamma}\left(\tau\right)\end{aligned} \tag{2.22}$$

To sample ground state expectation values directly, we would like to sample:

$$\langle \hat{O} \rangle_{GS} = \frac{\langle \Psi_0 | \hat{O} | \Psi_0 \rangle}{\langle \Psi_0 | \Psi_0 \rangle}$$

Defining the imaginary time propagation of $|\Psi(\tau)\rangle$ and $\langle \Psi(\tau)|$ as

$$\begin{aligned} |\Psi(\tau)\rangle &\equiv e^{-\tau \hat{H}} |\Psi\rangle = e^{-\tau \hat{V}} \hat{\sigma}(\tau) |\Psi\rangle \\ \langle \Psi(\tau)| &\equiv \langle \Psi | e^{\tau \hat{H}} = \langle \Psi | e^{\tau \hat{V}} \left(e^{(-\tau)\hat{V}} e^{-(-\tau)\hat{H}} \right) = \langle \Psi | e^{\tau \hat{V}} \hat{\sigma}(-\tau), \end{aligned}$$

we can approximate the ground state via propagating the trial wave function in imaginary time:

$$\langle \Psi_0 | \propto \lim_{\tau \to -\infty} \langle \Psi_T(\tau)|. \tag{2.23}$$

Therefore to approximate the ground state observables we want to take matrix elements:

$$\langle \hat{O} \rangle_{GS} = \lim_{\tau_R \to \infty} \lim_{\tau_L \to -\infty} \frac{\langle \Psi_T | e^{\tau_L \hat{V}} \hat{\sigma}(-\tau_L) \hat{O} e^{-\tau_R \hat{V}} \hat{\sigma}(\tau_R) | \Psi_T \rangle}{\langle \Psi_T | e^{\tau_L \hat{V}} \hat{\sigma}(-\tau_L) e^{-\tau_R \hat{V}} \hat{\sigma}(\tau_R) | \Psi_T \rangle}$$

We can sample this expectation value by taking a single imaginary time path $0 \leq \tau \leq \beta$ with $\tau_R = \tau$ and $\tau_L = \tau - \beta$. In this case $\langle \Psi_T(\tau_L)|$ is propagated backwards in imaginary time to τ. If we sample observables at the center of the path $\tau = \beta/2$, we have:

$$\langle \hat{O} \rangle_{GS} = \lim_{\beta \to \infty} \frac{\sum_{\alpha,\lambda,\gamma} c_\alpha^* e^{-\beta/2 V_\alpha} \sigma_{\alpha\lambda}(\beta/2) O(\lambda) e^{-\beta/2 V_\lambda} \sigma_{\lambda\gamma}(\beta/2) c_\gamma}{\sum_{\alpha,\lambda,\gamma} c_\alpha^* e^{-\beta/2 V_\alpha} \sigma_{\alpha\lambda}(\beta/2) e^{-\beta/2 V_\lambda} \sigma_{\lambda\gamma}(\beta/2) c_\gamma} \tag{2.24}$$

To compute the sums in (2.21), (2.22), and (2.24) we need to be able to statistically sample $\sigma_{\alpha\gamma}(\tau)$, the off-diagonal matrix elements of the imaginary-time propagator.

2.2.4 Monte Carlo Updates for Sampling $\sigma_{\alpha\beta}$

For clarity, in what follows, I refer to the path of the entire system in configuration space, not paths of individual particles. This choice is to accommodate models with complex interactions, such that a single kink may change change the state of multiple particles. A segment is defined as an imaginary time interval between two neighboring kinks (i.e. there are no kinks within a segment). As such, a segment has a constant, well defined potential energy. We define "interacting kinks" as kinks that involves spins that interact in the Hamiltonian. To sample (2.19) we will use several types of updates:

(i) Create or annihilate kink-antikink pairs $(Q_0, Q_0^\dagger)$ within an interval containing kinks interacting with Q_0 (see figure 2.1)

(ii) Displace single a kink Q_0 along path between nearest kinks of type $Q_0, Q_0^\dagger$ (see figure 2.2)

(iii) Insert or remove single kinks at the ends of the path

These updates are illustrated in figures (2.1-2.2) To collect statistics, we will attempt a number of updates N_{meas} between each measurement which we define as one MC step. The next sections describe in detail the implementations of these updates.

Creation and annihilation of kink-pairs

Consider two paths (+,-) related by the creation of a kink pair, with statistical weights A_-, A_+. Path (+) is related to (-) by the addition of the kink pair $(Q_0(\tau_a), Q_0^\dagger(\tau_b))$ (see figure 2.1). Following reference 100, detailed balance between these two paths is given by:

$$A_- P^c_{\text{att}} W(\tau_a, \tau_b) P^c_{\text{acc}} d\tau_a d\tau_b = dA_+ P^a_{\text{att}} P^a_{\text{acc}} \tag{2.25}$$

Here $P^a_{\text{att}}, P^c_{\text{att}}$ are the probability of attempting the creation and annihilation updates on this path segment, $W(\tau_a, \tau_b)$ is the probability density of choosing $\{\tau_a, \tau_b\}$ and $P^a_{\text{acc}}, P^c_{\text{acc}}$ are the probabilities of accepting the updates. From (2.19) we have:

$$\frac{dA_+}{A_-} = d\tau_a d\tau_b |q|^2 e^{-(\tau_{i+1}-\tau_a)\Delta \text{V}_i} \left(\prod_{k=i+1}^{j-1} e^{-(\tau_{k+1}-\tau_i k)\Delta \text{V}_i} \right) e^{-(\tau_b - \tau_j)\Delta \text{V}_j} \tag{2.26}$$

Again following reference 100, we define $R(\tau_a, \tau_b)$:

$$R(\tau_a, \tau_b) = \frac{P^a_{\text{att}}}{P^c_{\text{att}}} |q|^2 e^{-(\tau_{i+1}-\tau_a)\Delta \text{V}_i} \left(\prod_{k=i+1}^{j-1} e^{-(\tau_{k+1}-\tau_i k)\Delta \text{V}_i} \right) e^{-(\tau_b - \tau_j)\Delta \text{V}_j} \tag{2.27}$$

We can satisfy detailed balance by choosing:

$$P^c_{\text{acc}} = \min\left(\frac{R(\tau_a, \tau_b)}{W(\tau_a, \tau_b)}, 1 \right)$$
$$P^a_{\text{acc}} = \min\left(\frac{W(\tau_a, \tau_b)}{R(\tau_a, \tau_b)}, 1 \right)$$

The updating procedure is as follows

1. Choose a segment at random.
2. Choose a kink pair $\{Q_0, Q_0^\dagger\}$ to create at random.

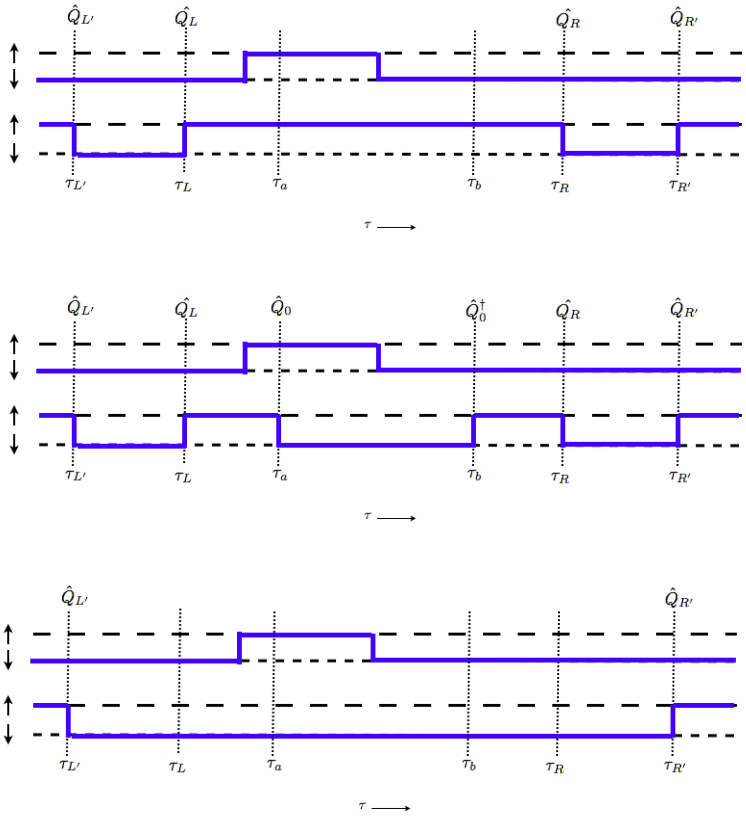

Figure 2.1: Illustration creation and annihilation updates. Top panel: initial configuration. Middle panel: configuration after creation of $Q_0(\tau_a), Q_0^\dagger(\tau_b)$. Bottom panel: configuration after annihilation of $Q_L(\tau_L), Q_R(\tau_R)$ from top. Each configuration shows the world-lines of two neighboring spins.

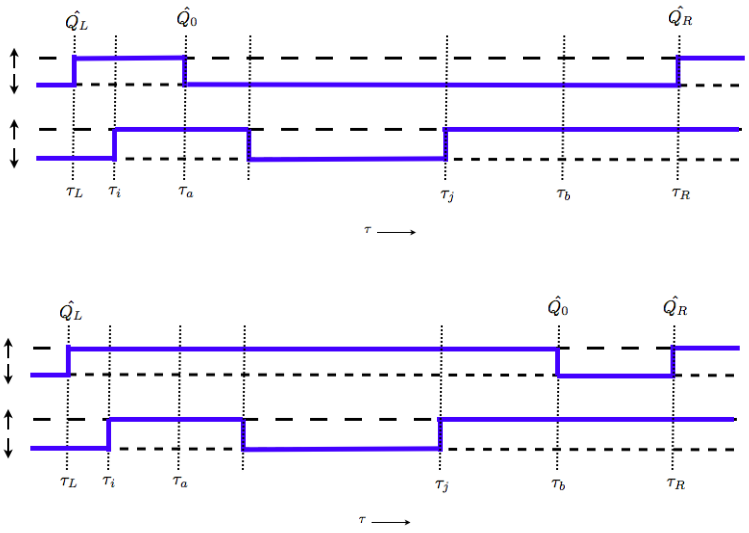

Figure 2.2: Illustration of displacement updates. Two configurations related by displacing Q_0 from τ_a to τ_b. Each configuration shows the worldlines of two neighboring spins.

3. Identify the neighboring kinks of the same type, $\{Q_L(\tau_L), Q_R(\tau_R)\}$ and count the number of segments between (τ_a, τ_b), n_{seg}

4. If $\{Q_L(\tau_L), Q_R(\tau_R)\}$ form a kink-antikink pair, choose to attempt a creation or annihilation update with equation probability ($p_c = 1/2$), otherwise choose a creation update ($p_c = 1$):

   (a) If a creation update is chosen:

      i. Compute the mean potential $\Delta\bar{\mathrm{V}}$ of Q_0 in the interval (τ_L, τ_R):

$$\Delta\bar{\mathrm{V}} \equiv \frac{1}{\Delta\mathrm{T}} \log\left(\frac{A_+(\tau_L, \tau_R)}{A_-}\right) = \frac{1}{\Delta\mathrm{T}} \sum_{k=L}^{R-1} (\tau_{k+1} - \tau_k)\, \Delta\mathrm{V}_k, \quad \Delta\mathrm{T} \equiv \tau_R - \tau_L$$

      ii. Given two random numbers $r_1, r_2 \in (0,1)$ Choose $\Delta\tau$ with statistical weight $w(\Delta\tau) = \frac{\Delta\bar{\mathrm{V}}}{1-e^{-\Delta\bar{\mathrm{V}}\Delta\mathrm{T}}} e^{-\Delta\bar{\mathrm{V}}(\Delta\tau)}$ and $\tau_a \in (\tau_L, \tau_L + (\Delta\mathrm{T} - \Delta\tau))$ with constant probability density:

$$\begin{aligned}
\Delta\tau &= \frac{-1}{d\bar{V}} \log\left(r_1 \left(1 - e^{-\Delta\bar{\mathrm{V}}\Delta\mathrm{T}}\right)\right) \\
\tau_a &= \tau_L + r_2\,(\Delta\mathrm{T} - \Delta\tau) \\
\tau_b &= \tau_a + dt
\end{aligned}$$

This generates

$$W\left(\tau_a, \tau_b\right) = \frac{1}{\Delta \mathrm{T} - \Delta\tau} \frac{\Delta\bar{\mathrm{V}}}{1 - e^{-\Delta\bar{\mathrm{V}}\Delta \mathrm{T}}} e^{-\Delta\bar{\mathrm{V}}(\Delta\tau)}$$

iii. Count n'_{seg}, the number of segments between (τ_a, τ_b).

iv. Compute $R(\tau_a, \tau_b)$ from (2.27), given that the above procedure generates:

$$P^c_{att} = p_c \frac{n_{seg}}{N_{seg}}, \quad P^a_{att} = \frac{1}{2} \frac{n'_{seg}}{N'_{seg}}$$

v. Accept the kink pair creation update with probability:

$$P^c_{\mathrm{acc}} = \min\left(\frac{R\left(\tau_a, \tau_b\right)}{W\left(\tau_a, \tau_b\right)}, 1\right)$$

(b) If an annihilation update is chosen:

i. Remove the kink-pair $\{Q_L(\tau_L), Q_R(\tau_R)\}$.

ii. Identify the nearest kinks of the same type as Q_L, $\{Q_{L'}(\tau'_L), Q_{R'}(\tau'_R)\}$ and count the number of segments between $(\tau_{L'}, \tau_{R'})$, n_{seg}. We define $\Delta\mathrm{T}' = \tau_{L'} - \tau_{R'}$

iii. If $\{Q_{L'}(\tau_{L'}), Q_{R'}(\tau_{R'})\}$ form a kink anti-kink pair, $p_c = \frac{1}{2}$, otherwise $p_c = 1$.

iv. Compute the mean potential $\Delta\bar{\mathrm{V}}$ of Q_L in the interval $(\tau_{L'}, \tau_{R'})$:

$$\Delta\bar{\mathrm{V}} \equiv \frac{1}{\Delta\mathrm{T}'} \log\left(\frac{A\left(\tau_{R'}\right)}{A\left(\tau_{L'}\right)}\right) = \frac{1}{\Delta\mathrm{T}'} \sum_{k=L'}^{R'-1} \left(\tau_{k+1} - \tau_k\right) \Delta\mathrm{V}_k, \quad \Delta\mathrm{T} \equiv \tau_{R'} - \tau_{L'}$$

v. Compute the probability density of selecting (τ_a, τ_b) in the reverse creation process, $W\left(\tau_L, \tau_R\right)$:

$$W\left(\tau_L, \tau_R\right) = \frac{1}{\left(\Delta\mathrm{T}' - \Delta\mathrm{T}\right)\left(\Delta\mathrm{T}'\right)} \frac{\Delta\bar{\mathrm{V}}}{e^{-\Delta\bar{\mathrm{V}}\Delta\mathrm{T}'} - 1} e^{-\Delta\bar{\mathrm{V}}\Delta\mathrm{T}}$$

vi. Compute $R(\tau_L, \tau_R)$:

$$R\left(\tau_L, \tau_R\right) = \frac{P^a_{att}}{P^c_{att}} \frac{A_+\left(\tau_L, \tau_R\right)}{A_-}$$

$$\frac{A_+\left(\tau_L, \tau_R\right)}{A_-} = e^{-(\tau_{i+1} - \tau_L)\Delta\mathrm{V}_i} \left(\prod_{k=i+1}^{j-1} e^{-(\tau_{k+1} - \tau_i k)\Delta\mathrm{V}_i}\right) e^{-(\tau_R - \tau_j)\Delta\mathrm{V}_{j+1}}$$

$$P^a_{att} = \frac{1}{2} \frac{n_{seg}}{N_{seg}}, \quad P^c_{att} = p_c \frac{n'_{seg}}{N'_{seg}}$$

vii. Accept the kink-pair annihilation update with probability:

$$P^a_{\rm acc} = \min\left(\frac{W\left(\tau_L,\tau_R\right)}{R\left(\tau_L,\tau_R\right)},1\right) \tag{2.28}$$

Kink Displacement

Consider a configuration with Q_0 at τ_a and a 2nd configuration with Q_0 shifted to τ_b as in figure 2.2. For use below, we define $\Delta \mathrm{V}_i = V_i^R - V_i^L$ where $V_i^{R,L}$ are given by:

$$\hat{V}|\alpha_i\rangle = V_i^L|\alpha_i\rangle$$
$$\hat{V}\hat{Q}_0|\alpha_i\rangle = V_i^R\hat{Q}_0|\alpha_i\rangle$$

and $|\alpha_i\rangle$ is the state in the interval (τ_i,τ_{i+1}) with the kink Q_0 removed. Here we assume the initial ordering of the kinks is:

$$\ldots Q_i(\tau_i)Q_0(\tau_a)Q_{i+1}\tau_{i+1}\ldots Q_j(\tau_j)Q_{j+1}(\tau_{j+1})$$

and after the displacement:

$$\ldots Q_i(\tau_i)Q_{i+1}\tau_{i+1}\ldots Q_j(\tau_j)Q_0(\tau_a)Q_{j+1}(\tau_{j+1})$$

Detailed balance for such a procedure is given by:

$$A(\tau_a)P^s_{\rm att}W_d\left(\tau_b\right)P^{\tau_a\to\tau_b}_{\rm acc}d\tau = A(\tau_b)P^s_{\rm att}W_d\left(\tau_a\right)P^{\tau_b\to\tau_a}_{\rm acc}d\tau$$

The kink displacement procedure is as follows:

1. Choose a kink Q_0 at random. This gives $P^s_{\rm att} = 1/N_k$.
2. Identify the the nearest non-commuting kinks, $\{Q_L(\tau_L), Q_R(\tau_R)\}$
3. Compute the mean potential $\bar{\Delta \mathrm{V}}$ of Q_0 in the interval (τ_L,τ_R):

$$\bar{\Delta \mathrm{V}} \equiv \frac{1}{\Delta \mathrm{T}}\log\left(\frac{A\left(\tau_R\right)}{A\left(\tau_L\right)}\right) = \frac{1}{\Delta \mathrm{T}}\sum_{k=L}^{R-1}\left(\tau_{k+1}-\tau_k\right)\Delta \mathrm{V}_k, \quad \Delta \mathrm{T} \equiv \tau_R - \tau_L \tag{2.29}$$

4. Choose τ_b with statistical weight $W_d\left(\tau_b\right) = \frac{\bar{\Delta \mathrm{V}}}{e^{\bar{\Delta \mathrm{V}}\Delta \mathrm{T}}-1}e^{\bar{\Delta \mathrm{V}}(\tau_b-\tau_L)}$ by selecting a random number $r \in (0,1)$:

$$\Delta\tau = \frac{1}{\Delta \mathrm{V}}\log\left(1+r\left(e^{\Delta \mathrm{V}\Delta \mathrm{T}}-1\right)\right)$$
$$\tau_b = \tau_L + \Delta\tau$$

5. Compute $R(\tau_a, \tau_b)$:

$$R\left(\tau_a, \tau_b\right) \equiv \frac{A\left(\tau_b\right)}{A\left(\tau_a\right)} = e^{-(\tau_{i+1}-\tau_a)\Delta \mathrm{V}_i} \left(\prod_{k=i+1}^{j-1} e^{-(\tau_{k+1}-\tau_i k)\Delta \mathrm{V}_i} \right) e^{-(\tau_b-\tau_j)\Delta \mathrm{V}_{j+1}} \tag{2.30}$$

6. Accept the displacement update with probability:

$$P_{\mathrm{acc}}^{s} = \min\left(R\left(\tau_a, \tau_b\right) \times e^{\Delta \bar{\mathrm{V}}(\tau_a-\tau_b)}, 1\right) \tag{2.31}$$

2.3 Proof of principle results for the QDM

Since exact diagonalization via the Lanczos method is possible for small lattice systems, we may compare the QMC results for a $L = 4$ toroidal triangular lattice with the exact numerical results; this allows for a proof of principle test of the PIGS QMC algorithm. Figure 2.3 shows PIGS results for $L = 4$ and $\beta t = 10$ for $v/t = 0.8$ using the RK state as the trial wave function. In 2.3a and 2.3b the potential and kinetic energy along the path are plotted vs. imaginary time. The energies have been averaged over bins of width $\delta\tau = 0.01\beta$ (note that the kinetic energy estimator is only defined for an imaginary time bin of finite width, but diagonal quantities such as the potential energy are defined at all points on the path). The exponential convergence of the energies toward the exact values over an imaginary time interval of $\Delta\tau t \sim 4$ is evident. Figure 2.3 shows the expectation values computed at the center of the path compared to the exact values (here a bin of with $\delta\tau = 0.01\beta$ is used for the kinetic energy). We see that the fractional errors relative to the exact values are of the order $10^{-5} - 10^{-4}$, and in all cases is less than the statistical error. Here the statistical errors are computed by a standard binning method [4]. We note that the statistical errors of the kinetic energy are a factor of several larger than those for diagonal quantities.

Figure 2.4 shows the fractional errors relative to exact diagonalization for $L = 4$, $\beta t = 8$ with a RK trial wave function over a range of v/t. The error bars represent the statistical errors–when these extend off the plot, the errors are smaller than the statistical errors. The fraction errors are of order 10^{-3}; while not all errors are smaller than the statistical errors, we expect this due to the finite β which limits the precision of the PIGS ground state results. We have not found any systematic error other than that due to finite β, which can be reduced by using longer imaginary time paths.

In addition to using the RK wave function as the trial wave function at the ends of the imaginary time path, we have also tried using a one-parameter optimized trial wave function to improve convergence at a given β. We consider a variational wave function that accounts for the potential energy: $\Psi_\alpha(a) = \alpha^{-N_f(a)}$, where $N_f(a)$ is the number of flippable plaquettes

of a configuration a. We use a variational Monte Carlo method to minimize the energy of Ψ_α with respect to α for a given v/t; since this is a one parameter optimization, we have implemented a binary search to find the energy minimum. In general there appears to be little benefit from using this simple variation ally optimized wave function as compared to the equal superposition state. Similar precision is obtained with either trial wave function for a given β.

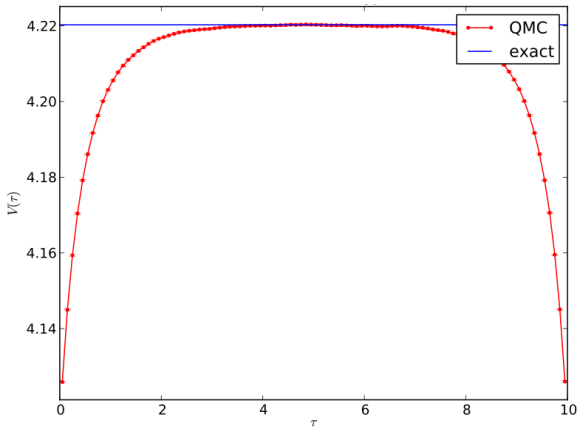

(a) potential energy

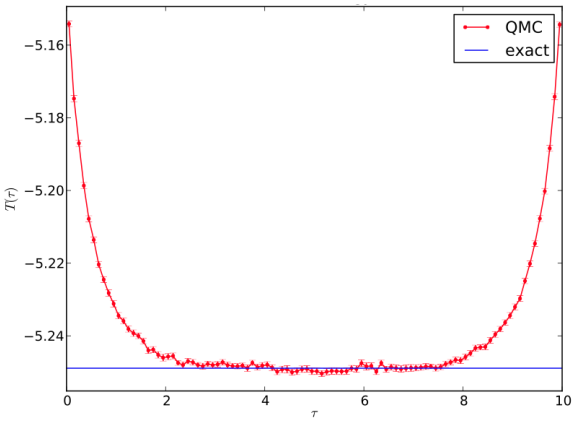

(b) kinetic energy

	T	V	N_{fp}	M^2_{rot}	M^2_{col}
exact	-5.2489	4.22027	5.27534	0.32128	0.37517
QMC	-5.2498	4.22032	5.27541	0.32130	0.37516
stat. err.	0.0009	0.00032	0.00040	0.00006	0.00009
error	-0.0009	0.00006	0.00007	0.00002	-0.00001

(c)

Figure 2.3: PIGS results vs. exact diagonalization for $L = 4$, $\beta t = 10$ using an RK trial wave function. The table displays the expectation values at the center of the path.

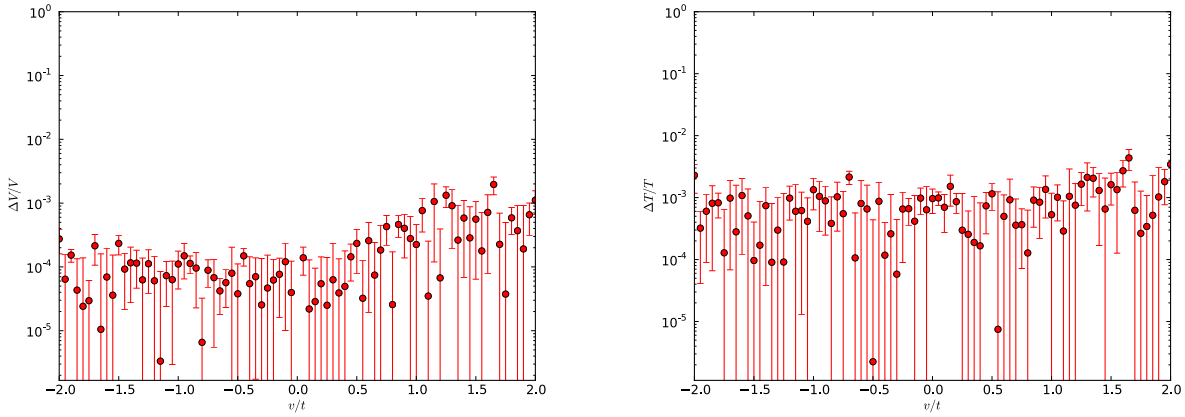

(a) potential energy

(b) kinetic energy

Figure 2.4: PIGS fractional errors for $L = 4$, $\beta t = 8$ using an RK trial wave function. The error bars represent the statistical errors. Error bars that go below the bottom of the plot represent errors that are smaller than the statistical error. Errors larger than the statistical error can be reduced by increasing β.

Chapter 3

Loop condensation in the triangular lattice quantum dimer model

This chapter presents a study of loop condensation in the triangular lattice quantum dimer model. Sections 3.1-3.6 present the results of classical Monte Carlo calculations and appear in reference 49. Section 3.7 presents some PIGS QMC calculations of triangular lattice quantum dimer model.

3.1 Mapping a dimer model to a loop model

A dimerization of a lattice, $|C\rangle$, can be interpreted as a closed loop covering of the lattice by superimposing it with an arbitrary reference dimerization, $|R_0\rangle$ (see figure 3.1) [117, 70]. The resulting doubled dimerization, $\{C : R_0\}$, known as the transition graph, has both a reference and physical dimer touching each vertex; this therefore forms closed loops on the lattice with the exception of where dimers in $|C\rangle$ coincide with those of $|R_0\rangle$. It is necessary to choose a convention for the definition of such coinciding dimers. Two possible interpretations of overlapping dimers are: (a) they are considered to be a loops of length 2, or (b) they are defined as an empty links of the transition graph. Choosing option (a) means that the transition graph is a fully packed loop covering of the lattice and the transition graph $\{R_0 : R_0\}$ comprises all length 2 loops. Choosing (b) means that the transition graph is not fully packed, and that $\{R_0 : R_0\}$ is an empty loop covering. In order to make an analogy with the definitions of loops given in equation (1.6), we will generally choose below the convention (b), except where noted.

Choosing a reference dimerization $|R_0\rangle$ translates a dimer configuration into a loop configuration. However, unlike the toric code, there is no reference configuration that retains all of the lattices symmetries. Therefore we are forced to choose an $|R_0\rangle$ that breaks translational and rotational symmetries of the lattice. Certain properties of the resulting loop model will depend on this choice of a symmetry broken $|R_0\rangle$. All other dimerizations can

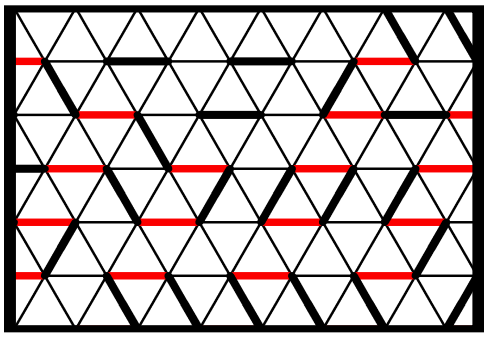

Figure 3.1: A transtion graph loop configuration $\{C : R_0\}$ formed by superimposing a physical dimer configuration $|C\rangle$ (black) with the reference dimerization $|R_{col}\rangle$ (red).

be reached from $|R_0\rangle$ by applying a product of closed loop operators that alternately pass through the links that are occupied and unoccupied by dimers in $|R_0\rangle$:

$$|C\rangle = \prod_{\ell \in \{\ell_C\}_{R_0}} W_\ell |R_0\rangle, \quad W_\ell \equiv \prod_{(r,s)\in\ell} d_r^- d_s^+. \tag{3.1}$$

In equation (3.1), $d_j^+ (d_j^-)$ are dimer creation (annihilation) operators and (r, s) are a pair of links in ℓ that meet at a vertex, that are occupied and unoccupied, respectively, by a dimer in $|R_0\rangle$. The set $\{\ell_C\}_{R_0}$ is simply the transition graph $\{C : R_0\}$, where we interpret links that are occupied in both in $|C\rangle$ and $|R_0\rangle$ as empty links in $\{\ell_{R_0}\}$. We note that the choice of $|R_0\rangle$ restricts the possible loop coverings such that if a loop touches a vertex, it must pass through the link occupied in $|R_0\rangle$. This dimer-loop Hilbert space is not equivalent to the Hilbert space of all loop coverings of the lattice.

The phases of H_{RK} may now be re-interpreted as those of a loop model. $|RK\rangle$ is the equal superposition of all loop coverings that pass through the dimers of $|R_0\rangle$, and therefore is a loop gas. We expect the topological phase adjacent to the RK point to be described by a scale-invariant loop liquid. Static dimer crystal phases, such as the columnar and staggered phases, correspond to loop crystals with a narrow distribution of loop lengths; if $|R_0\rangle$ is chosen to be a dimer configuration with the corresponding broken symmetry, then the loop model is in a short looped dilute phase. The loop order in the resonating $\sqrt{12} \times \sqrt{12}$ phase is less obvious: if $|R_0\rangle$ is chosen to be one of the dimerizations with $\sqrt{12} \times \sqrt{12}$ order, the ideal $\sqrt{12} \times \sqrt{12}$ state will be a dense, fluctuating short looped phase. This transition loop description of the dimer model allows us to make a connection to the loop condensation picture of topological order. A dimer crystal to dimer liquid transition is then described as a transition from a loop crystal to a scale-invariant loop liquid.

3.2 The dimer liquid at the RK point

Here we analyze the geometric properties of the loop description of the RK wavefunction, taking this to be representative of the dimer liquid. This analysis follows a similar approach as that of Sutherland and Kohmoto & Shapir in their studies of the spin-1/2 RVB wavefunction on the square lattice [117, 70, 71, 115, 116, 111]. To understand the loop properties of $|RK\rangle$, we can refer to the classical $O(n)$ loop model [26, 94, 95]. In this model, which can be solved exactly on the honeycomb lattice, configurations are closed loop coverings of the lattice, and the partition function is given by

$$Z_{O(n)} = \sum_C K^{\mathcal{L}} n^{\mathcal{N}}, \tag{3.2}$$

where C is a closed loop configuration comprising $\mathcal{N}$ loops of total length $\mathcal{L}$. In equation (3.2) , K is the weight per length of loops and n is the loop fugacity. For $n \leq 2$, there are two phases separated by a critical line at $K_c = [2+\sqrt{2-n}]^{-1/2}$. K_c separates a dense loop phase for $K > K_c$ and a dilute phase for $K < K_c$. The dense phase is characterized by a power law distribution of loop lengths, $P_\ell(s) \sim s^{-p}$, where $P_\ell(s)$ is the density of loops of length s [25]. Additionally, there is a large spanning loop ℓ_M with fractal dimension D_f, whose length scales with the system size L as $s(\ell_M) \sim L^{D_f}$ [107]. These exponents are related by the scaling dimension x:

$$D_f = 2 - x, \qquad p = 1 + \frac{2}{2-x} \tag{3.3}$$

Within the dense phase, x is given by

$$x = \frac{g}{2} - \frac{1}{2g}(g-1)^2, \quad n = -2\cos(\pi g) \tag{3.4}$$

for $0 < g \leq 1$ where g is the coupling constant of the Coulomb gas description of of the $O(n)$ model [95]. The $O(n)$ loop model on the triangular lattice has been studied by Knops *et. al.*, and is known to possess a critical dense phase of the same universality class as that of the honeycomb lattice [68].

In the $O(1)$ model on the honeycomb lattice, $K_c = 1/\sqrt{3}$, so $K = 1$ is in the dense phase. At $K = 1$, $Z_{O(1)}$ is an equal weighted sum over all loop configurations with the critical exponents $D_f = 7/4$ and $p = 15/7$ [95, 107]. The RK wavefunction can similarly be described as equal superposition of all transition loop configurations within a topological sector, for a given choice of $|R_0\rangle$, and therefore we can relate the loop configuration at the RK point to the critical phase of $O(1)$ model.

To calculate the loop properties of $|RK\rangle$ we choose a reference configuration $|R_0\rangle$, and then compute the distribution of loops in the transition graph, $P_\ell^{R_0}(C,s) = h_\ell^{R_0}(C,s)/L^2$ where $h_\ell^{R_0}(C,s)$ is the number of loops of length s in $\{C : R_0\}$ and L is the linear dimension

of the lattice. We have computed the expectation value of $P_\ell^{R_0}$ by Monte Carlo sampling of $|RK\rangle$ using local plaquette flip updates on triangular lattices of up to $L = 192$, with $N_l = 3 * L^2$ links.

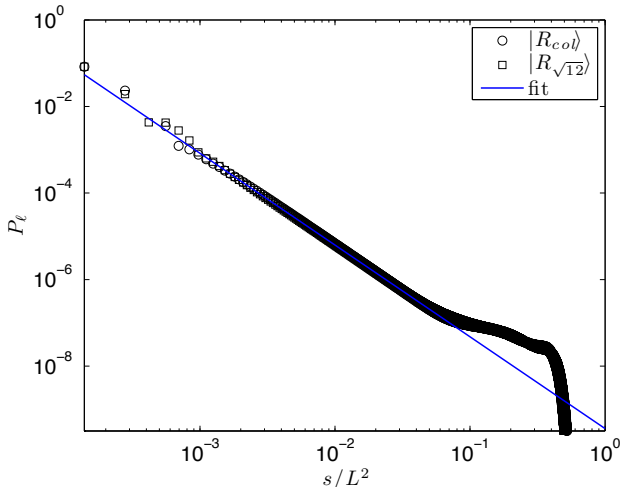

Figure 3.2: Loop distribution P_ℓ vs. loop length s at the RK point on a $L = 120$ triangular lattice using reference configurations $|R_{col}\rangle$ and $|R_{\sqrt{12}}\rangle$ in the (E, E) winding sector. The line shows the fit to a power law decay.

Here we will consider two choices of reference configurations: $|R_{col}\rangle$, the columnar reference state shown by the red links in figure 1.6a, and $|R_{\sqrt{12}}\rangle$, which is the configuration illustrated by the thick red links in figure 1.6b that is one of the equally weighted configurations of the ideal $\sqrt{12} \times \sqrt{12}$ crystal. In figure 3.2, the loop distribution $P_\ell(s)$ is plotted for these choices of $|R_0\rangle$. We see a clear power law over a range of length scales. The best fit power law $p = 2.12 \pm 0.01$; this is consistent with the theoretical value for the $O(1)$ model, $p = 15/7 \simeq 2.14$ [95, 25], considering the imperfect power law behavoir of P_ℓ on lattices of these sizes. Additionally, we see that $P_\ell(s)$ is independent of the choice of $|R_0\rangle$ for lengths longer than about 16. We have computed the distribution of the longest loop ℓ_M, $P_{\ell_M}(s)$, and this is plotted in figure 3.3a. To compute D_f at the RK point, we analyze the finite size scaling of ℓ_M, shown in figure 3.3 (b). The best fit gives $D_f = 1.751 \pm .001$, which agrees with the known fractal dimension of the $O(1)$ model, $D_f = 7/4$ [95, 107].

We can also characterize the loop liquid in terms of the total loop density, $\rho = \mathcal{L}/\mathcal{L}_M$, where $\mathcal{L}_M = L^2$ is the maximum possible total loop length. The value $\rho = 1$ corresponds to the maximum loop density, where no dimers reside on links occupied in $|R_0\rangle$, while ρ strictly vanishes only for $|R_0\rangle$. Consequently, in crystalline phases, ρ depends on the choice of $|R_0\rangle$. At the RK point, all links are occupied with probability 1/6, and the total loop length is twice the average number of dimers on links unoccupied in $|R_0\rangle$, which is $5/6 \times N_l/6$. Therefore at the RK point, $\rho = 5/6$; this agrees with our numerically computed value of

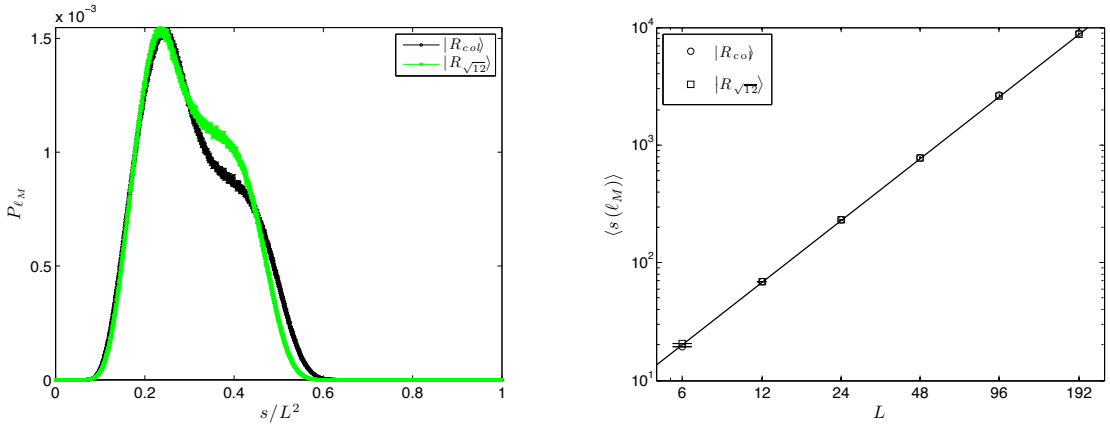

Figure 3.3: (a) Longest loop distribution, P_{ℓ_M} vs. loop length $s(\ell_M)$ at the RK point using reference dimerizations $|R_{col}\rangle$ and $|R_{\sqrt{12}}\rangle$, in the (E,E) winding sector on lattice size $L = 72$. (b) Finite size scaling of the expectation value of the length of the longest loop $s(\ell_M)$ at the RK point for $|R_{col}\rangle$ and $|R_{\sqrt{12}}\rangle$, in the (E,E) winding sector of lattice sizes up to $L = 192$. Errorbars are smaller than the symbols shown. The line shows the fit to $s(\ell_M) \propto L^{D_f}$.

$\rho = 0.83333(3)$ on a $L = 120$ lattice, computed for $|R_{col}\rangle$ and $|R_{\sqrt{12}}\rangle$. The RK wavefunction can be described as a dense loop gas. We note that in this loop gas phase, both the total density and geometric properties of loops are independent of the choice of $|R_0\rangle$.

3.3 Loop order in dimer crystal phases

Here will consider the loop order in transitions from the dimer liquid at the RK point to two dimer crystals that are present in phase diagram of the cannonical QDM as defined in equation (1.8). To analyze these transitions, we will consider a wavefunction that interpolates between $|RK\rangle$ and a given dimer crystalline order:

$$|\Psi(z)\rangle = \frac{1}{\sqrt{Z}} \sum_C z^{N_B} |C\rangle \tag{3.5}$$

Here we will consider two possible colorings of the triangular lattice where the red links define links that are favored by the crystalline order, to which we give weight 1, and N_B is the number of occupied black links, which are given a weight z. In equation (3.5), $Z \equiv \sum_C z^{2N_B(C)}$, which is the partition function of a non-interacting classical dimer model where black links are given a fugacity z^2. Additionally, $|\Psi(z)\rangle$ is the zero energy ground state of a

local, stochastic matrix form [7, 20] Hamiltonian that is generalization of $H_{\rm RK}$:

$$H_z \equiv \sum_p - \quad t\Big(|\boldsymbol{\mathit{\Delta}}\rangle\langle\boldsymbol{\mathit{\nabla}}| + h.c.\Big) + t\Big(z^{\Delta N_B}\,|\boldsymbol{\mathit{\Delta}}\rangle\langle\boldsymbol{\mathit{\Delta}}| + z^{-\Delta N_B}\,|\boldsymbol{\mathit{\nabla}}\rangle\langle\boldsymbol{\mathit{\nabla}}|\Big) \tag{3.6}$$

where $\Delta N_B \equiv N_B(\boldsymbol{\mathit{\nabla}}) - N_B(\boldsymbol{\mathit{\Delta}})$. For $z = 1$, $|\Psi\,(z=1)\rangle$ is the RK wave function, and and for $z = 0$, $|\Psi\,(z=0)\rangle$ is an ideal dimer crystal as defined by the red links of the lattice.

As described in section 1.4, $H_{\rm RK}$ displays two crystalline phases for $v < t$, in addition to the dimer liquid phase. These crystal orders are illustrated in figure 1.6: the red links of panel (a) show one of 12 symmetry related columnar states, and the red links of panel (b) are favored by the $\sqrt{12} \times \sqrt{12}$ resonating crystalline order. We will use these two colorings to define two wave functions described by equation 3.5: $|\Psi_{col}\rangle$and $|\Psi_{\sqrt{12}}\rangle$. We will use $|R_{col}\rangle$ and $|R_{\sqrt{12}}\rangle$ respectively as the reference configurations to define the transition loops. We have computed the loop distributions for both from Monte Carlo sampling of these wave functions.

We can relate $|\Psi(z)\rangle$ to the $O(1)$ model by considering $|\Psi_{col}\rangle$. In this case, since only the occupied links in R_{col} are colored red, the total loop length $\mathcal{L} = 2 * N_B$, and $-Log(z)$ acts as an effective loop tension. Accordingly, we can relate z to K in the $O(1)$ model. As discussed in section 3.2, $z = 1$ sits in the dense phase, corresponding to the dimer liquid, and for some $z_c < 1$ we expect to cross a phase transition into the dilute loop phase, corresponding to the dimer crystal. The relationship is less direct for $|\Psi_{\sqrt{12}}\rangle$, where loop segments within the red hexagons are given unity weight, and only loop segments passing through black links are given a weight $z < 1$. However we still expect a transition from the long loop dense phase, to a short loop phase of finite loop density.

In figure 3.4, the left panels show the total loop density ρ, and the right panels show the expectation value of the longest loop length, $s(\ell_M)$ as a function z, for $|\Psi_{col}\rangle$(top) and $|\Psi_{\sqrt{12}}\rangle$(bottom). Here we have rescaled $s(\ell_M)$ by $L^{7/4}$ where 7/4 is the fractal dimension of the dimer liquid. In both cases $s(\ell_M)/L^{7/4}$ remains finite for z close to 1 and vanishes for small z. Finite size scaling of $s(\ell_M)$ suggests that the corresponding phase transitions occur at $z_c^{col} \approx 0.57$ for $|\Psi_{col}\rangle$ and $z_c^{\sqrt{12}} \approx 0.53$ for $|\Psi_{\sqrt{12}}\rangle$. For $|\Psi_{col}\rangle$, ρ vanishes in the columnar phase, whereas ρ remains finite in the $\sqrt{12} \times \sqrt{12}$ phase of $|\Psi_{\sqrt{12}}\rangle$. This distinction is due to the fact that in the columnar phase, dimers are pinned to $|R_{col}\rangle$, whereas the $\sqrt{12} \times \sqrt{12}$ phase dimers resonate within the hexagons and are not pinned to $|R_{\sqrt{12}}\rangle$. The location of these transitions may be compared with the transition of the honeycomb lattice O(1) model, where $K_c = 1/\sqrt{3} \simeq 0.58$. Figure 3.5a shows the longest loop distributions $P_{\ell_M}(s)$ for $|\Psi_{col}\rangle$ (left) and $|\Psi_{\sqrt{12}}\rangle$ (right) for several values of z. We see that in both cases the broad distribution, which is a signature of the liquid phase, vanishes below the transition at z_c. The fractal dimension within the dimer liquid phase is plotted in figure 3.5b. Deviations from $D_f = 7/4$ in the liquid phase near the transition may be due to the limitations of extrapolating the finite size scaling on lattices of these sizes.

We note that in the crystalline phases, the loop distributions depend on the choice of

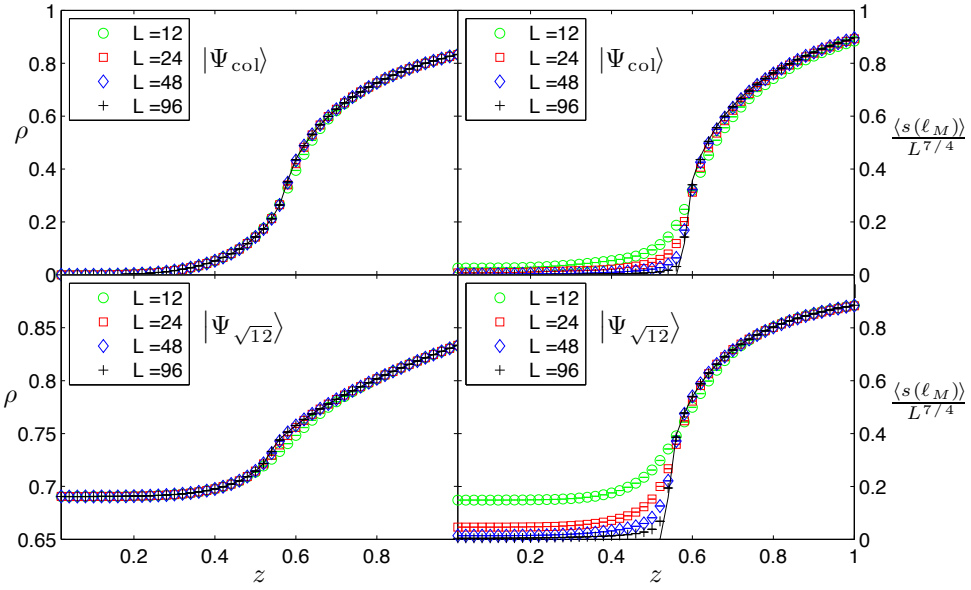

Figure 3.4: Top two panels: The total loop density ρ, and and longest loop length $s(\ell_M)$ for $|\Psi_{col}\rangle$. Bottom two panels: The total loop density ρ, and and longest loop length $s(\ell_M)$ for $|\Psi_{\sqrt{12}}\rangle$. The solid lines are extrapolations to the thermodynamic limit. We have rescaled $s(\ell_M)$ by $L^{7/4}$ for data collapse in the liquid phase.

$|R_0\rangle$; here we have chosen reference dimerizations which reflect the known ordering in each phase. In particular, the vanishing of $s(\ell_M)/L^{D_f}$ in the crystalline phases is due to a choice of $|R_0\rangle$ that is commensurate with the order. While in static crystals such as the columnar phase we may expect that any choice of $|R_0\rangle$ will lead to $s(\ell_M)$ scaling as L^0, L^1, or L^2, in a resonating dimer crystal such as $\sqrt{12}\times\sqrt{12}$, this is not in general true. In fact, we find that for an arbitrary choice of $|R_0\rangle$ the loop distribution in a resonating crystal phase may appear to be that of a liquid phase. This is illustrated in figure 3.6 where we have computed P_{ℓ_M} for the ideal $\sqrt{12}\times\sqrt{12}$ state $|\Psi_{\sqrt{12}}(z=0)\rangle$ for two different columnar reference configurations: $|R_{col}\rangle$ (seen in figure 1.6a) and $|\tilde{R}_{col}\rangle$ which is related to $|R_{col}\rangle$ by translating all dimers one link horizontally. Figure 3.6 shows that for $|R_{col}\rangle$, P_{ℓ_M} appears to be a liquid phase, but for$|\tilde{R}_{col}\rangle$ it is sharply peaked at a single length scale. In fact finite size scaling of the length of ℓ_M shows that for $|R_{col}\rangle$, the fractal dimension is that of the liquid phase ($D_f = 7/4$), but for $|\tilde{R}_{col}\rangle$ $D_f = 1$, indicative of the crystal order. This suggests that one may distinguish a liquid phase by computing D_f for all (in this case 12) configurations that are related by symmetry to $|R_0\rangle$, to ensure that a resonating crystalline order is not hidden by the choice of $|R_0\rangle$. However, for any symmetry broken state, if $|R_0\rangle$ is chosen to be commensurate with the broken symmetry, the length of ℓ_M will be finite.

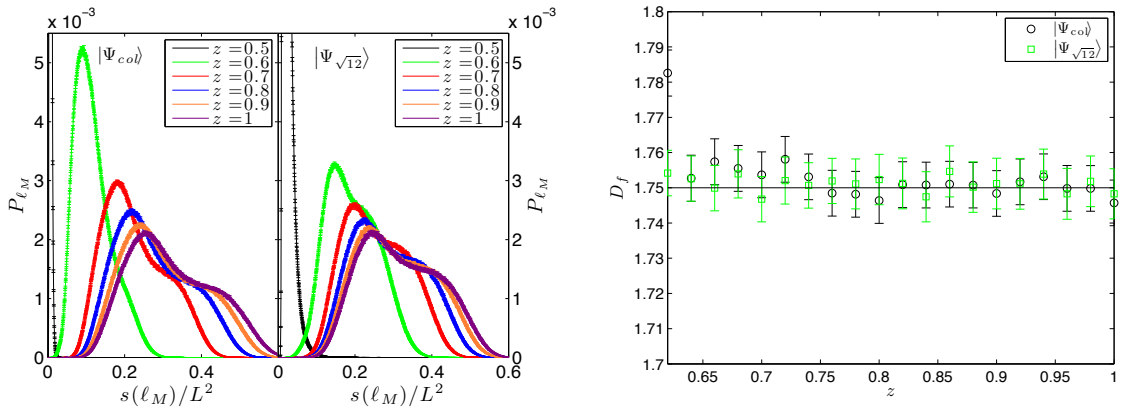

Figure 3.5: (a) Longest loop distribution P_{ℓ_M} of $|\Psi_{col}\rangle$ (left) and $|\Psi_{\sqrt{12}}\rangle$ (right) plotted for several values of z for a $L = 60$ lattice. (b) Fractal dimension D_f of $|\Psi_{col}\rangle$ and $|\Psi_{\sqrt{12}}\rangle$ in the dimer liquid phase computed from the finite size scaling of $s(\ell_M)$ with lattice sizes up to $L = 144$. The line shows the value at the RK point, $D_f = 7/4$. The accuracy of D_f is limited by the lattice sizes studied.

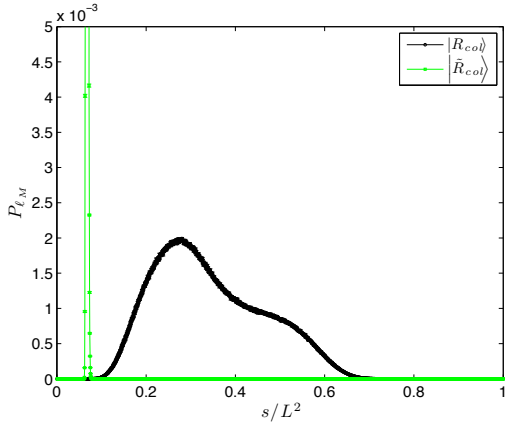

Figure 3.6: The longest loop distribution P_{ℓ_M} in the ideal $\sqrt{12} \times \sqrt{12}$ crystal, $|\Psi_{\sqrt{12}}(z = 0)\rangle$ computed for two different columnar reference configurations $|R_{col}\rangle$ and $|\tilde{R}_{col}\rangle$. In a resonating crystal phase, for some choices of $|R_0\rangle$, P_{ℓ_M} may clearly indicate crystalline order (seen by the peak at a single length scale for the choice $|\tilde{R}_{col}\rangle$) whereas for other choices (e.g. $|R_{col}\rangle$), the distribution P_{ℓ_M} may appear to be that of a liquid.

3.4 Interacting dimer loop liquid

Section 3.3 discusses the addition of an effective loop tension to the RK dimer liquid. Here we consider the effects of a translationally invariant dimer interaction by defining a generalization of the RK wave function:

$$|\Phi_\alpha\rangle = \frac{1}{\sqrt{Z}} \sum_C \alpha^{-N_f(C)} |C\rangle \tag{3.7}$$

In (3.7), $N_f(C)$ is the number of flippable plaquettes in $|C\rangle$. For $\alpha = 1$, $|\Phi_{\alpha=1}\rangle \equiv |RK\rangle$; for $\alpha \ll 1$, configurations with the maximum number of plaquettes are favored. The square norm of $|\Phi_\alpha\rangle$ is the partition function of an interacting classical dimer model [126]:

$$\langle \Phi_\alpha \mid \Phi_\alpha \rangle = Z_{cl} = \textstyle\sum_c e^{-\beta_{cl} E_{cl}(C)} \tag{3.8}$$

$$E_{cl}(C) = -uN_f(C), \quad \alpha = \exp\left(\tfrac{-\beta_{cl} u}{2}\right). \tag{3.9}$$

All equal time correlation functions of $|\Phi_\alpha\rangle$ are equal those of the classical model. This relationship allows us to write down a local RK-like Hamiltonian [7, 20] for which $|\Phi_\alpha\rangle$ is an exact zero energy ground state:

$$H_\alpha \equiv \sum_p -t\Big(|\square\!\!\!\!\square\rangle\langle\square\!\!\!\!\square| + h.c.\Big) + t\Big(\alpha^{-\Delta N_f/2}\,|\square\!\!\!\!\square\rangle\langle\square\!\!\!\!\square| \quad + \alpha^{\Delta N_f/2}\,|\square\!\!\!\!\square\rangle\langle\square\!\!\!\!\square|\Big), \tag{3.10}$$

with $\Delta N_f \equiv N_f(\square\!\!\!\!\square) - N_f(\square\!\!\!\!\square)$ and $N_f(\square\!\!\!\!\square)$ ($N_f(\square\!\!\!\!\square)$) is the total number of flippable plaquettes on the lattice with p in orientation $\square\!\!\!\!\square$ ($\square\!\!\!\!\square$). Here we see that $\alpha = 1 \Rightarrow u = 0$, which is the non-interacting point of the classical model; consequently $H_{\alpha=1} = H_{\rm RK}$ at the RK point ($v = t$). The interacting classical dimer model has previously been studied using transfer matrix techniques by Trousselet *et al.* [126]. For $u > 0$ ($\alpha < 1$), E_{cl} is minimized by configurations which have the maximum number of flippable plaquettes, $N_l/6$. There is a large number of such configurations, including the 12 symmetry related columnar states and all configurations related to these by translating rows of dimers (row shifting modes) or rotating all dimers in a set of columns (column shifting modes). For $\alpha = 0$, this degeneracy prevents the formation of local order. However an "order-by-disorder" mechanism [129] might allow for fluctuations to favor an ordered state for nonzero α. Indeed the results of Ref. [126] are consistent with a first order phase transition from a liquid phase for $\alpha > \alpha_c$ to an ordered phase for $\alpha < \alpha_c$, where the row shifting modes favor configurations with dimers aligned in the same direction.

Local updates do not give access to the global defects that appear as $\alpha \to 0$. Therefore we have implemented a directed loop Monte Carlo algorithm [109, 122] to sample $|\Phi_\alpha\rangle$ on lattice sizes up to $L = 128$, using $|R_{col}\rangle$ as the reference configuration. The dimer model directed-loop algorithm generates non-local updates by creating a pair of defects that violate the hard core, fully packed dimer constraint; these defects undergo a directed random walk

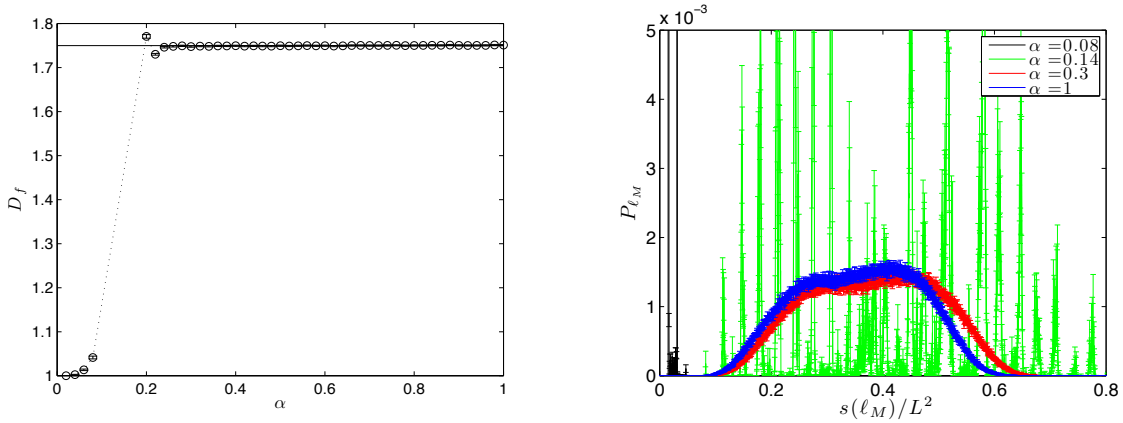

(a) **(b)**

Figure 3.7: (a) Fractal dimension of the largest loop ℓ_M of $|\Phi_\alpha\rangle$ computed with a directed loop algorithm for lattice sizes up to $L = 128$. The solid line corresponds to $D_f = 7/4$, the value at the RK point. The dotted line is a guide for the eye; the gap in data is where the finite size scaling of $s(\ell_M)$ doesn't converge to a power law for the lattice sizes studied. (b) Longest loop distribution of $|\Phi_\alpha\rangle$ on a $L = 64$ lattice, for several values of α, computed using $|R_{col}\rangle$. For very small α, P_{ℓ_M} is peaked at L, consistent with an ordered phase with all dimers aligned in the same direction.

around the lattice until they coincide and annihilate [109]. The path of these defects forms a closed loop, along which the dimer configuration is updated. To sample $|\Phi_\alpha\rangle$, we have chosen the local weights of each step in the random walk to reflect $|\Phi_\alpha\rangle$ [123], and found a solution to the *directed-loop equations* [122]. This algorithm is ergodic in all topological sectors, and therefore the results presented here are computed over all winding sectors.

Figure 3.7 shows that in the presence of interactions, the dimer liquid persists down to $\alpha \sim 0.2$. For much smaller values of α, D_f approaches 1, indicative of a symmetry broken phase. However there is an intermediate regime where the finite size scaling of ℓ_M does not converge to a power law (this is shown by the dotted line in figure 3.7). The longest loop distribution P_{ℓ_M} (right panel of figure 3.7) displays a series of peaks in this intermediate regime, whereas for small α, there is only a single peak at $s(\ell_M) = L$. The small α regime is consistent with the low temperature phase of Ref. [126] where row shifting modes dominate; with this choice of reference dimerization row defects are loops of length L winding around the lattice in the direction of the rows.

To further characterize the appearance of this symmetry breaking order for small α, we define a rotational symmetry breaking order parameter

$$M^2_{\rm rot} \equiv \frac{1}{2N_d^2} \sum_{i,j} \left(N_d^i - N_d^j\right)^2, \tag{3.11}$$

where i and j each represent one of the three possible dimer orientations on the triangular lattice, and N_d^i is the number of dimers in a given orientation. Additionally, we define a columnar order parameter,

$$M_{\rm col}^2 \equiv \frac{1}{N_d^2} \sum_{(r,c)} \left(N_d \left[R_{col}^{(r,c)} \right] - N_d \left[\tilde{R}_{col}^{(r,c)} \right] \right)^2, \tag{3.12}$$

where $R_{col}^{(r,c)}$ is a columnar configuration with rows oriented in direction r and columns in direction c, and $\tilde{R}_{col}^{(r,c)}$ is obtained by translating all dimers by one lattice spacing in direction r. $N_d[R]$ is the number of dimers that coincide with the configuration R. In a columnar ordered phase, the expectation values of both $M_{\rm rot}^2$ and $M_{\rm col}^2$ saturate to 1, whereas $M_{\rm rot}^2 = 1$ and $M_{\rm col}^2 = 0$ in the rotational symmetry broken ordered phase that is favored by the row shifting modes.

Figure 3.8 shows the expectation values of these dimer order parameters in the symmetry broken phases. We see that for small α, $M_{\rm rot}^2$ saturates to 1, whereas $M_{\rm col}^2$ scales to zero for larger system sizes (figure 3.8). This corresponds to the rotational symmetry broken phase where row defects dominate and destroy the columnar order, as discussed in Ref. [126]. However, there is an intermediate regime for larger system sizes where the expectation value of $M_{\rm rot}^2$ reaches at plateau at approximately 1/4, and $M_{\rm col}^2$ is finite and approaching 1/2. This is consistent with a phase for which column shifting modes dominate, such that two dimer directions are preferred. The ideal columnar defect configurations saturate the order parameter

$$M_{\rm cd}^2 \equiv \frac{1}{N_d^2} \sum_{(r,r',c)} \left(N_d \left[R_{col}^{(r,c)} \right] + N_d \left[R_{col}^{(r',c)} \right] - N_d \left[\tilde{R}_{col}^{(r,c)} \right] - N_d \left[\tilde{R}_{col}^{(r',c)} \right] \right)^2 \tag{3.13}$$

to 1, while $M_{\rm rot}^2$ and $M_{\rm col}^2$ are 1/4 and 1/2, respectively. In (3.13), the sum is over $r \neq r' \neq c$. Figure 3.8 shows that, in the intermediate phase, $M_{\rm cd}^2$ approaches 1 with decreasing α. We note that while perfect column defects cost zero (classical) energy, adding a horizontal kink to the column defect costs a finite energy; the increased degeneracy of kinked defects may favor them over perfect defects for sufficiently large α. If kinked column defects proliferate, they will generate a finite (but non-maximal) expectation value of M_{cd}^2. This suggests that for $\alpha \to 0$, global row defects dominate but there is an intermediate regime where kinked column defects dominate. Both of these transitions appear to be first order as shown by the discontinuities seen in these order parameters for larger system sizes (see figure 3.8); we have confirmed this by observing a double peak structure in the histograms of these order parameters at the transitions. Finite size scaling of these transitions suggests that both transitions occur at finite α in the thermodynamic limit.

The distinction between these results and what is seen in Ref. [126] is likely due to the difference in the geometry of the systems studied. We have also studied triangular lattices with $L_x \neq L_y$, where $L_{x,y}$ are the lengths in the two lattice directions. We find that as L_y/L_x

increases, the width of the intermediate regime decreases. This follows from the discussion of Ref. [126]: increasing L_y/L_x increases the number of row-shifting modes, and therefore favors the row defect ordering. Ref. [126] considers lattices with $L_y \gg L_x$, so the results of that work are consistent with ours in this limit.

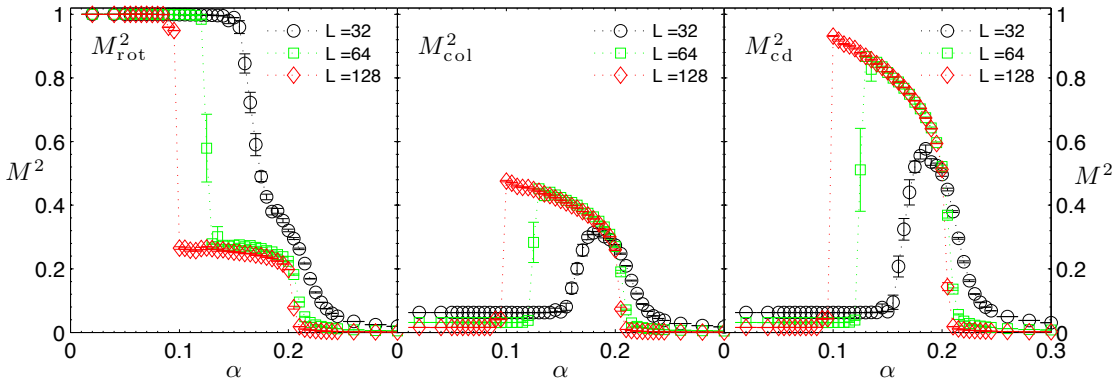

Figure 3.8: Expectation values of dimer order parameters $M^2_{\rm rot}$ (left), $M^2_{\rm col}$(center), $M^2_{\rm cd}$(right) in $|\Phi_\alpha\rangle$ in the symmetry broken phases. For larger values of α, all local order parameters vanish.

3.5 d-isotopic quantum loop gas in the triangular lattice QDM

So far we have only considered transitions out of the $O(1)$ dimer loop liquid to crystalline phases; we now consider a wavefunction that allows us to explore other loop gases in the triangular lattice QDM. In reference [40] Freedman *et. al.* introduced a generalization of the quantum loop gas of the toric code they termed the d-isotopic loop gas [40]. By giving

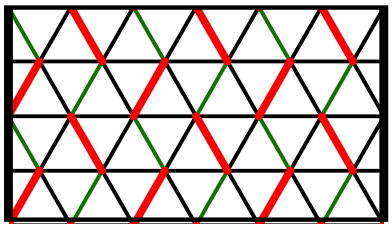

Figure 3.9: The decorated triangular lattice from reference [40] used to define $|\Psi_d\rangle$. Here the staggered configuration defined by the red links is used as the reference dimerization.

a weight d to each contractible loop in the ground state wavefunction, the $O(1)$ loop liquid of the toric code at $d = 1$ can be driven to loop gas phases for $O(n > 1)$:

$$|\Psi_d\rangle = \sum_C d^{\mathcal{N}_c} |C\rangle. \tag{3.14}$$

In equation (3.14), $\mathcal{N}_c$ is the number of contractible loops in $|C\rangle$ and the sum over C is taken over all configurations in the same winding sector. The norm of Ψ_d is equal to classical partition function of the $O(n)$ loop model for $n = d^2$ [41]. Freedman *et. al.* also wrote down an RK-like Hamiltonian, H_d for which $|\Psi_d\rangle$ is the exact zero energy ground state [40]. Every winding sector contains a unique ground state; as such this d-isotopic loop gas has a large degeneracy. For $1 \leq d \leq \sqrt{2}$, $|\Psi_d\rangle$ is a critical loop liquid and it has been shown that H_d is gapless. For $n > 2$, the $O(n)$ model is in a short looped phase [95], and correspondingly, the d-isotopic loop gas is in a short looped phase for $d > \sqrt{2}$. All diagonal local correlation functions in $|\Psi_d\rangle$ vanish exponentially; however Troyer et. al. showed certain that off-diagonal correlation functions have a power-law decay [128]. The original motivation for introducing $|\Psi_d\rangle$ was the search for gapped topological phases beyond the abelian toric code phase. Subsequent work [128] shows that adding local interactions to H_d to open a gap drives the loop gas to the toric code phase. Consistent with the disordered nature of the liquid phase of $|\Psi_d\rangle$, Troyer et. al. showed that the critical phase of the loop liquid could be described by the fractal dimension of the long fractal loop [128].

To implement Ψ_d in a quantum dimer model we color the triangular lattice according to reference [40]. Links occupied in a staggered reference configuration $|R_0\rangle$ are colored red and links connecting the red links are colored green (see figure 3.9). Here we choose a slightly different interpretation of the transition loop graph; dimers in $|C\rangle$ that coincide with $|R_0\rangle$ are considered to be minimal, length 2 loops. As such, the loop coverings defined by the transition graphs are fully packed loop coverings. In this case, Ψ_d is described by a fully packed loop model, which in turn is related to the dense phase of the $O(n)$ model [14]. Consequently, the geometric exponents as defined in section 3.2 are the same in the fully packed loop model as those of the dense phase of the $O(n)$ model with $d^2 = n$ [107, 74].

With this coloring, a local quantum dimer model Hamiltonian, H_d can be defined such that $|\Psi_d\rangle$ defines the unique, zero energy ground state in each winding sector. To allow for the transition to the short looped, staggered crystal phase in the limit $d \to \infty$, 4-dimer dynamics that flip dimers around a length 8 loop are included in H_d to connect the staggered configurations to other configurations. Additionally, following reference [40], we wish to define H_d such that it only connects configurations in the same loop winding sector, not in a parity defined winding sector. This requires removing the plaquette flip terms that can act as a surgery and connect different winding sectors–this is done by excluding plaquette flips in H_d for rhombi that have a green diagonal link. To compensate for a lost ergodicity due to the removal of these plaquette flip terms, a 3-dimer resonance around a length 6 triangular loops is also added to H_d [40].

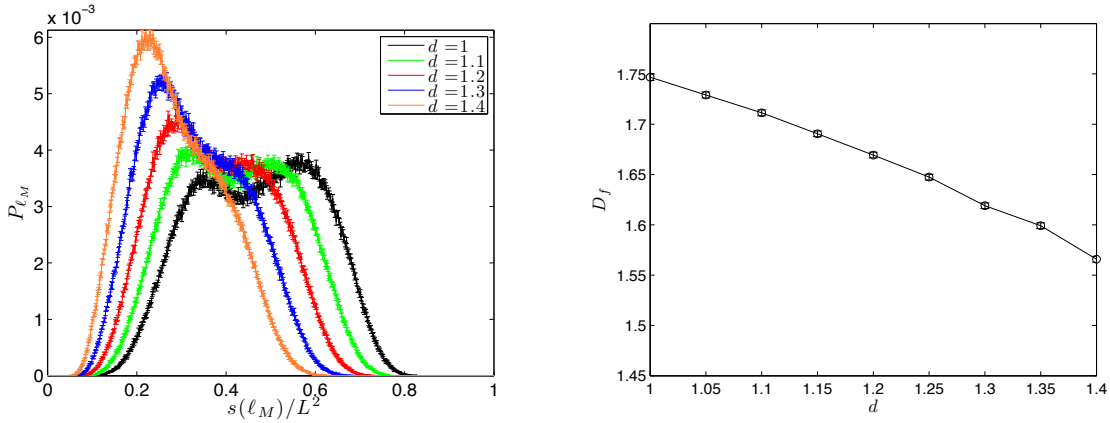

(a) (b)

Figure 3.10: (a) Longest loop distribution P_{ℓ_M} for $|\Psi_d\rangle$ in the zero winding sector on a $L = 24$ lattice for several values of d. (b) Fractal loop dimension of $|\Psi_d\rangle$, computed from finite size scaling of $s(\ell_M)$ on lattice sizes up to $L = 84$.

Figure 3.10a shows the longest loop distribution for several values of d computed by Monte Carlo sampling of $|\Psi_d\rangle$ in the triangular lattice quantum dimer model. We see that a liquid phase persists for $d > 1$. Figure 3.10a shows that the fractal dimension is a continuously varying function of d. Thus $|\Phi_d\rangle$ can describe dimer liquid phases distinct from the Z_2 topologically ordered phase at the RK point.

3.6 Off-diagonal loop operators in the triangular lattice QDM

Off-diagonal operators in a quantum dimer model that do not violate the hard-core constraint are loop operators: two dimer configurations can be connected by flipping dimers along their transition loops, as given in equation (3.1). In the toric code, such loop operators are related to the Wilson loop of the underlying Z_2 gauge theory. In, the ground state $|\Psi_{\rm TC}\rangle$, the expectation value of all loop operators is exactly 1 (a "zero law"). However the addition of a magnetic field will cause the loop operators to decay with the length of the loop (a "perimeter law"). In a quantum dimer model, the fully-packed constraint means that $\langle W_\ell(s)\rangle < 1$ for all loops, even at the RK point [84]. Moessner, Sondhi and Fradkin suggested that $\langle W_\ell(s)\rangle$ will decay as a perimeter law at the RK point due to the extensive entropy of dimerizations of the lattice [88]. Figure 3.11 shows $\langle W_\ell\rangle_{\rm RK}$ computed for a set of parallelograms of differing lengths on the triangular lattice by Monte Carlo sampling of $|RK\rangle$. $\langle W_\ell(s)\rangle$ is seen to display a clear perimeter law at the RK point.

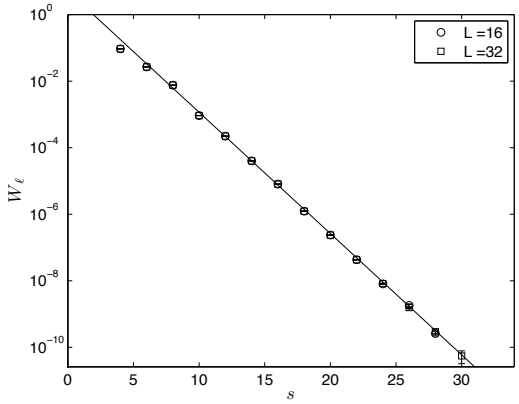

Figure 3.11: Expectation value of off-diagonal loop operator W_ℓ as a function of loop lenth s at the RK point, computed for various parallelograms of different lengths on lattices of size $L = 16, 32$. The line shows a fit to an exponential decay, indicating a clear perimeter law behavior.

3.7 The QDM on the triangular lattice away from the RK point

Here we will consider the canonical triangular lattice QDM away from the RK point. To study the ground state away from the RK point, we have performed PIGS QMC calculations as described above in section 2.2. Prior studies [89, 104, 103] have shown that the topologically ordered quantum liquid phase extends from the RK point down to $v/t \approx 0.86$, where the liquid phase gives way to the $\sqrt{12} \times \sqrt{12}$ resonating dimer crystal, which persists down to $v/t < 0$ [84, 105]. We have computed the transition loop distributions of the ground state as a function of v/t to give insight into the mechanism of loop condensation in this model.

To confirm that a given PIGS calculation has converged to the ground state, we have repeated each calculation with several values of β; once we see convergence of the relevant observables within the statistical errors with increasing β, we conclude these agree with the ground state expectation values within the error bars. Additionally, computing the energies as a function of imaginary time allows for a qualitative check on convergence. Due to the local nature of the Monte Carlo updates, all of these calculations are performed within a single topological sector; while the liquid phase occurs in all sectors, we have chosen the topological sector which can accommodate the relevant crystalline phase. The gap that is relevant to the convergence of these calculations is the lowest gap within the topological sector. As shown by prior studies [104, 105, 57], this gap Δ is of order $0.1t$ and vanishes at the transition. The small size of this gap means that relatively long imaginary time paths are required to ensure convergence to the ground state, since we require $\beta/2 > 1/\Delta$ for convergence. In the small and moderate lattices we have studied the finite size gaps are

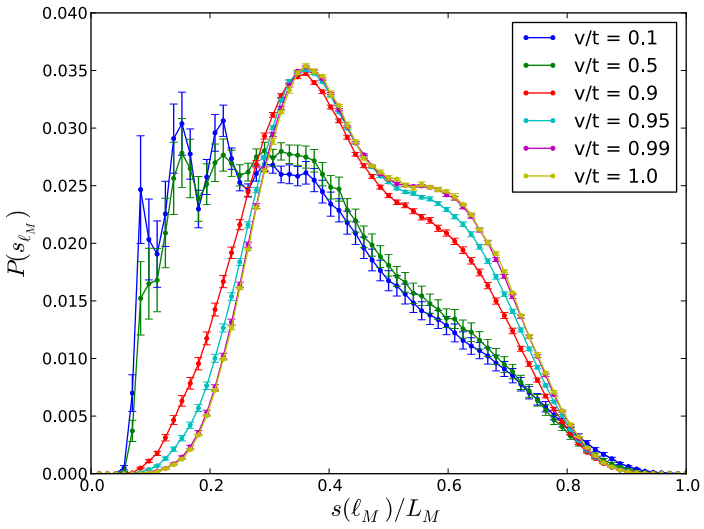

Figure 3.12: Longest loop distribution for $L = 12$, $\beta t = 32$ for several values of v/t using $|R_{\sqrt{12}}\rangle$ as the reference dimerization. The broad distribution of the RK point persists in the liquid phase, but sharp feature that are signatures of the symmetry breaking appear in the $\sqrt{12} \times \sqrt{12}$ phase.

somewhat larger, and therefore the required β grows with lattice size. While a variational wave function may in principle improve convergence at a given β, we have seen little benefit for simple one parameter variational wave functions, so all results presented here use the RK wave function to cap the ends of the imaginary time path. We have performed calculations up to $\beta t = 64$ and found that the energies had converged to within 10^{-2} by $\beta t = 32$ in the liquid phase; only smaller β were required for the crystalline phase.

Figure 3.12 shows the longest loop distribution for a variety of values v/t, including regimes both inside liquid and $\sqrt{12} \times \sqrt{12}$ phases. The liquid phase clearly displays the smooth distribution similar to that of the RK point. For $v/t = 0.1$ and 0.5 which are inside the $\sqrt{12} \times \sqrt{12}$ phase, there are sharp features in $s(\ell_M)$ that are a signature of the symmetry breaking in the crystal. Additionally, we have performed finite size scaling of $s(\ell_M)$ over several lattice sizes. The long imaginary times required due to the smallness of the gap of the liquid phase limit the system sizes accessible to the PIGS QMC algorithm. Computational resources have limited these studies to lattices sizes of $L = 12$ and smaller and these lattice sizes do limit the precision to which we can compute the fractal dimension. In figure 3.13 the finite size scaling of $\langle s(\ell_M)\rangle$ is plotted for values of v/t within the liquid regime. Here we have used $|R_{col}\rangle$ as the reference dimerization, since only lattices with L a multiple of 6 allow for the $R_{\sqrt{12}}$ dimerization. From finite size scaling we have computed the fractal dimension for $v/t = 0.90$, 0.95 and 0.99 to be $D_f = 1.89 \pm 0.01$, 1.84 ± 0.01,

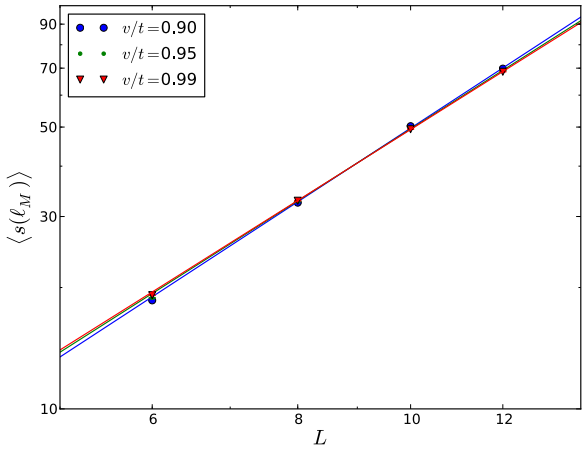

Figure 3.13: Finite size scaling of the expectation value of the longest loop length for $\beta t = 32$ for several values of v/t in the liquid regime using $|R_{col}\rangle$ as the reference dimerization. The lines represent the best power law fits; from these we compute $D_f = 1.89 \pm 0.01$, 1.84 ± 0.01, and 1.82 ± 0.01 for $v/t = 0.90$, 0.95 and 0.99, respectively. However, the lattice sizes studied are too small for a precise determination of the fractal dimension, as the finite size scaling has not converged to a pure power law.

and 1.82 ± 0.01 respectively. However, for these small lattice sizes, the finite size scaling of $\langle s(\ell_M)\rangle$ has not converged to a true power law; larger lattices sizes must be used to accurately determine D_f. Consequently, we cannot conclusively determine the fractal dimension in the liquid regime from these calculations.

Chapter 4

Loop condensed phases on the square lattice

This chapter presents the results of classical directed-loop Monte Carlo calculations of loop condensed states on the square lattice. The wave functions presented here have been well studied in the literature (especially the RK wave function of the square lattice dimer model and toric code ground state); here we focus on the loop condensed nature of these phases, and compute the fractal dimension of the underlying loop gas.

4.1 Loop condensation from local constraints

Lattice models with local geometric constraints can often be mapped to loop models, and consequently display a variety of loop condensed, quantum liquid phases. On the square lattice these loop condensed phases include gapped liquid phases with exponentially decaying loop density correlation functions (such as the toric code ground state [64]) as well as gapless, critical liquid phases with algebraically decaying loop density correlation functions (e.g. the RK wave function of the QDM [106]). Here we explicitly discuss the loop condensed nature of several liquid states in geometrically constrained models on the square lattice; in particular we compute the fractal dimension of the underlying loop gas, as and examine the fractal dimension as distinguishing feature of these phases.

Consider a lattice model with Ising degrees of freedom that live of the links of the lattice: the two states of each link correspond to a link that is occupied or unoccupied by a dimer. A link l (un)occupied by a dimer is the $+1(0)$ eigenstate of the dimer number operator $n_l = d_l^+ d_l^-$, with $d_l^{+/-}$ the dimer creation and annihilation operators. The simplest local constraint is to fix the dimer number at each vertex to be a constant n_0; we define the configuration space $\{C_{n_0}\}$ to be the set of configurations with n_0 dimers touching each vertex (see figure 4.1). On a square lattice there are only two interesting cases: $n_0 = 1$ (or $n_0 = 3$) and $n_0 = 2$. $\{C_1\}$ comprises fully-packed, hard-core dimerizations of the lattice.

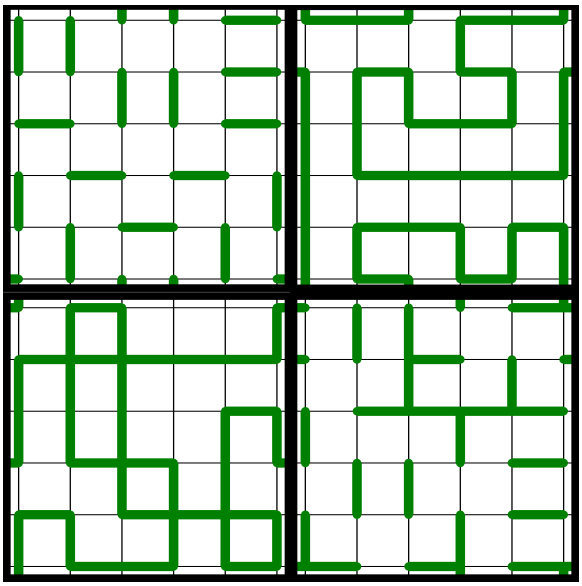

Figure 4.1: Examples of configurations with the local constraints on the square lattice. Clockwise from upper left: $\{C_1\}$, $\{C_2\}$, $\{C_e\}$, $\{C_o\}$, which have local constraints that restrict configurations to have a one, two, an even and odd number of dimers touching each vertex, respectively.

$\{C_2\}$ comprises fully-packed, non-intersecting loop configurations with two dimers touching each vertex.

All fully-packed, hard-core dimerizations in $\{C_1\}$ can be mapped to a non-intersecting closed loop configurations by choosing a reference dimerization R_0 (see figure 4.3). When a dimerization is superimposed over R_0, every vertex will be touched by both one physical dimer and one reference dimer. With the exception of links where a physical dimer coincides with a reference dimer, the doubled dimerization forms a closed loop covering of the lattice, where the loops comprise links that alternatingly occupied by physical and reference dimers. We choose to define links with overlapping physical and reference dimers to be unoccupied in the loop picture.

The simplest liquid state in these constrained Hilbert spaces is given by the Rokhsar-Kivelson wave function[106], which is an equal super-position of all configurations obeying the constraint:

$$\left|\Psi^{n_0}_{\mathrm{RK}}\right\rangle \equiv \frac{1}{\sqrt{\mathcal{N}_{n_0}}} \sum_{C_{n_0}} \left|C_{n_0}\right\rangle. \tag{4.1}$$

On a surface with trivial topology, the sum in (4.1) is over all configurations C that obey the given local constraint and $\mathcal{N}_{n_0}$ is the number of such configurations. For $n_0 = 1$, $|\Psi^1_{\mathrm{RK}}\rangle$ is the Rokshar-Kivelson state in the quantum dimer model. Diagonal expectation values

of $|\Psi^{n_0}_{\rm RK}\rangle$ are equal to those of the corresponding classical model [20]. Consequently, the behaviors of the correlation functions and local order parameters of $|\Psi^{n_0}_{\rm RK}\rangle$ are determined by the statistical mechanics of the related classical models. Diagonal correlation functions of $|\Psi^{1}_{\rm RK}\rangle$ are determined by the classical dimer model [34, 33, 35, 60, 61], and those of $|\Psi^{2}_{\rm RK}\rangle$ by the classical fully-packed loop model, with a loop fugacity (the statistical weight per loop) equal to 1 [73, 74, 58] (which maps to the 6-vertex model [11]). For all such constraints there exists a local RK-like Hamiltonian for which $|\Psi^{n_0}_{\rm RK}\rangle$ is the exact ground state, just as we have seen in the QDM.

In reference 88, Moessner, Sondhi and Fradkin show that a local dimer number constraint generates a local $U(1)$ invariance. If we define the operator $n_v = \sum_{l\in v} n_l$ where n_l is the dimer number operator on the link l, then all states $|\psi_{n_0}\rangle$ that obey the local constraint, are invariant under the local gauge transformation:

$$G^{n_0}_v(\alpha) \equiv \exp\Big(i\alpha\,(n_v - n_0)\Big), \quad G^{n_0}_v(\alpha)\Big|\psi_{n_0}\Big\rangle = \Big|\psi_{n_0}\Big\rangle. \tag{4.2}$$

This suggests that if $|{\rm RK}\rangle$ is in a liquid phase, $H_{\rm RK}$ is related to a $U(1)$ gauge theory. Indeed, $H_{\rm RK}$ has been shown to map to a $U(1)$ gauge theory for both $n_0 = 1$ [36, 37] and $n_0 = 2$ [7].

We now consider relaxing the dimer number constraint to a local dimer parity constraint. Here $\{C_e\}$ and $\{C_o\}$ which comprise configurations with a fixed dimer number parity at each vertex, have an even or odd number of dimers touching each vertex, respectively. The physical states $|\psi_{e,o}\rangle$ that are formed from superpositions of $\{|C_{e,o}\rangle\}$ are invariant under the gauge transformations

$$G^e_v \equiv \exp\big(\pm i\pi n_v\big), \quad G^e_v\Big|\psi_e\Big\rangle = \Big|\psi_e\Big\rangle \tag{4.3}$$

$$G^o_v \equiv \exp\Big(\pm i\pi\,(n_v+1)\Big), \quad G^o_v\Big|\psi_o\Big\rangle = \Big|\psi_o\Big\rangle. \tag{4.4}$$

Note that the $U(1)$ symmetry of $G^{n_0}_v(\alpha)$ has been reduced to a Z_2 symmetry in $G^{e,o}_v$ [88].

We may define a Hamiltonian that commutes with $G^{e,o}_v$

$$H_{\rm TC} = -t\sum_p \prod_{l\in p} d^x_l \tag{4.5}$$

where $d^x_l \equiv 1/\sqrt{2}(d^+_l + d^-_l)$ and $d^{+/-}_l$. This is the magnetic term of the toric code Hamiltonian [64]. In the toric code Hamiltonian the dimer parity constraint is imposed by a local energy cost at each vertex; here we take that energy cost to be infinite so there is hard constraint. The ground state of 4.5 is the equal superposition of all configurations in the given parity sector:

$$\Big|\Psi^{e/o}_{\rm TC}\Big\rangle \equiv \frac{1}{\sqrt{\mathcal{N}_{e/o}}}\sum_{C_{e/o}}\Big|C_{e/o}\Big\rangle. \tag{4.6}$$

In the language of the [88], 4.6 in the even (odd) parity sector corresponds to the even (odd) Ising Gauge theory [69].

We may understand the relationship between the $U(1)$ gauge theory describing 4.1 with a local dimer number constraint, and the Z_2 gauge theory that describes 4.6 with a fixed dimer parity constraint. Since the square lattice is bipartite, the links can be oriented to point from one sublattice to the other; dimers can be viewed as carrying a flux into or out of a vertex according to this orientation. The $n_v = 2$ constraint acts as Gauss's law, such that there is a flux of $+2$ and -2 on each vertex of sub-lattice A and B respectively; correspondingly we can consider there to be a static background charge of ± 2 on the two sub lattices. Now consider if $|\Psi^2_{\mathrm{RK}}\rangle$ is doped with dynamic $n_v = 0, 4$ vertices; these will act as charge ± 2 objects, depending on the sub lattice. Allowing $n_v = 0, 4$ vertices will transform $|\Psi^2_{\mathrm{RK}}\rangle$ into $|\Psi^e_{\mathrm{TC}}\rangle$, which is the toric code ground state, and therefore is described by a Z_2 gauge theory [64]. This transition from a $U(1)$ gauge theory to a Z_2 gauge theory via the introduction of charge 2 objects follows the well know prescription of Fradkin and Shenker who showed that coupling a $U(1)$ gauge field to charge $N > 1$ matter field can break the $U(1)$ gauge symmetry down to Z_N [38]. The same picture applies in the odd sector, where the QDM can be viewed as a $U(1)$ gauge theory with ± 1 background charges on the sublattices; here introducing $n_v = 3$ vertices is equivalent to allowing charge 2 matter fields and generates $|\Psi^o_{\mathrm{TC}}\rangle$ which is described by the odd Ising gauge theory. This construction begs the question of whether other Z_N models may live at the RK points of geometrically constrained models on the square lattice; in particular, doping the QDM with charge ± 3 $n_v = 4$ vertices might lead to a Z_3 liquid phase, purely via geometrical constraints.

4.2 Toric code

As discussed above in section 1.3, the ground state of the toric code, $|\Psi^e_{\mathrm{TC}}\rangle$, may be described as a loop condensate on the square lattice [64]. This gapped liquid phase has exponentially decaying spin-spin correlation functions. The ground state subspace is that of closed loop coverings of the square lattice, with the exception that two loops may meet at a vertex. Since $|\Psi^e_{\mathrm{TC}}\rangle$ is an equal superposition of all loop coverings, we may relate it to the $O(1)$ loop model, by choosing a resolution of the four-loop vertices. Here we choose an orientation of the loops, such that loops do not cross at a $n_v = 4$ vertex (see figure 4.1). In figure 4.2, the finite size scaling of the largest loop of the toric code wave function is plotted. From this we have extracted the fractal dimension to be $D_f = 1.7502 \pm 0.0002$ which agrees with the known value for the $O(1)$ model, $D_f = 7/4$ [27]. Similarly, we have computed the fractal dimension for the odd Ising gauge theory described by $|\Psi^o_{\mathrm{TC}}\rangle$, and found that it is also 7/4. This suggests that the fractal dimension of 7/4 is universal for the Z_2 topological liquid phases, such as those of the toric code, odd Ising gauge theory, as well as that in the triangular lattice quantum dimer model.

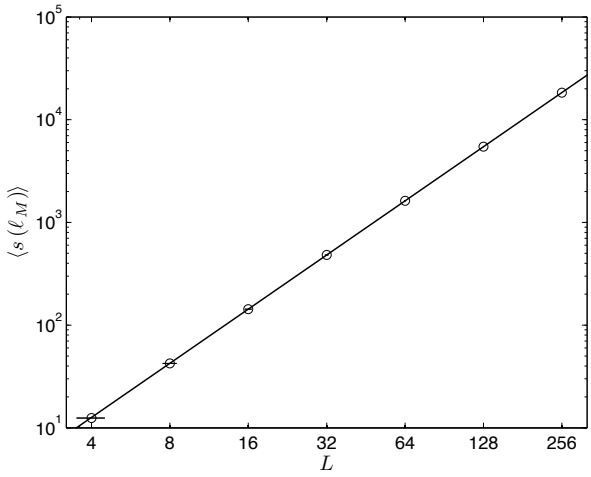

Figure 4.2: Finite size scaling of the longest loop in toric code ground state ($|\Psi^e_{\rm TC}\rangle$). We find $D_f = 1.7502 \pm 0.0002$, consistent with the universality of the fractal dimension of the gapped Z_2 liquid.

4.3 Square lattice QDM

The ground state of the RK point of the square lattice QDM is a gapless critical dimer liquid, with power-law decaying dimer-dimer correlations [106]. As described above in section 4.1, a dimer model may be mapped to a closed loop model by introducing a reference dimerization. As such we may view the RK point of the square lattice QDM as a loop condensed liquid phase. There is a well known phenomenological height model description of the square lattice RK wave function [48, 72, 101]. Here we will give a variant of this height model picture that makes the meaning of the loop picture more transparent (see figure 4.3):

- First we orient the links such that the arrows point from sub-lattice A to B and choose a reference plaquette to assign a height of $h = 0$, as in figure 4.3.
- Heights $h(r)$ may be assigned to all other plaquettes by starting with the reference plaquette and moving along any path crossing the links, where we assign a δh for each link, with $|\delta h| = 1$.
- If a link crossed with the arrow pointing to the right is occupied by a dimer, $\delta h = +1$, occupied by a reference dimer $\delta h = -1$, and vice versa if the link points to the left.
- Flipping parallel dimers on a plaquette will change the local height by ± 1.

With this mapping, the transition loops formed from the reference and physical dimerization act as the contour loops of the height field, as the height only changes when a transition loop is crossed (see figure 4.3).

We then propose an effective gaussian action for a coarse grained height field which captures the local height fluctuations and describes the dimer liquid at the RK point:

$$S_{\mathrm{RK}} = \int dr^2 \frac{K}{2} |\bigtriangledown h|^2 + V(r), \tag{4.7}$$

such that the statistical weight for a given configuration of heights proportional to $exp(-S)$. In (4.7), K is the stiffness and the first term captures the fluctuations of the height field. $V(r)$ is a locking potential which favors certain ordered height configurations. In this picture, at the RK point on the square lattice, the locking potential is irrelevant in the renormalization group sense, and therefore the effective action is gaussian. This gaussian action describes a rough phase of the height model, where h fluctuates along the lattice, and such a phase can be shown to have power law correlation functions. Consequently, the height model can capture the critical correlations of the dimer liquid at the RK point, with an appropriate choice of the stiffness K. We note that this height model description is purely phenomenological–currently there is no well known microscopic derivation of this action for the QDM. The transition loops to the reference dimerization take on a special meaning in the height model: they are the contour loops of the height model, in that the height only changes when a transition loop is crossed (see figure 4.3). It has been shown by Kondev & Henley that the fractal dimension of the contour loops of a gaussian height model is universal (independent of the stiffness K) and equal to 3/2 [75].

We have computed the fractal dimension of the transition loops of the square lattice QDM at the RK point via directed loop Monte Carlo calculations. Figure 4.4 shows the finite size scaling of the fractal loop, and the best fit power law gives $D_f = 1.502 + \pm 0.002$. This acts as a quantitative check on the height model description of the square lattice QDM. Additionally we note that the fractal dimension of the transition loop distinguishes the critical liquid RK point of the from the gapped liquid of the triangular QDM, where we saw the fractal dimension is 7/4.

4.4 Fully packed loop model

The fully packed loop model is a critical liquid state with algebraically decaying loop-loop correlation functions [73, 58]. Just as with the RK point of the square lattice QDM, there is also a phenomenological mapping of this model, which describes the RK wave function with a 2-dimer constraint at each vertex, $|\Psi^2_{\mathrm{RK}}\rangle$, to a height model [58, 73] . Similar to the dimer model case, the loops are oriented and act as the contour loops of the height field. However, in this case the Gaussian action is augmented by an additional relevant (in the renormalization group sense) term (which acts as a background charge in the Coulomb gas description of the height model [73, 58, 95]):

$$S_{\mathrm{FPLM}} = \int dr^2 \Big(\frac{K}{2} |\bigtriangledown h|^2 + V(r) \Big) + S_{BKGD}.$$

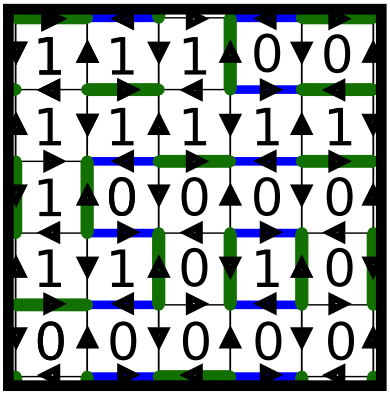

Figure 4.3: An example of the mapping of the square lattice QDM to a height model. The green dimers represent the physical dimers and the blue dimers are the background dimerization. The lower left plaquette is chosen to have $h_0 = 0$ and all other heights are determined by following a path from h_0 through the links of the lattice. If a dimer is crossed with the arrow pointing to the right (left) the height changes by $+1$ (-1) and vice versa for a reference dimer. Flipping dimers on a flippable plaquette changes the local eight of the plaqeutte by ± 1. The transition loops formed by alternating green and blue dimers are the contour loops of the height field.

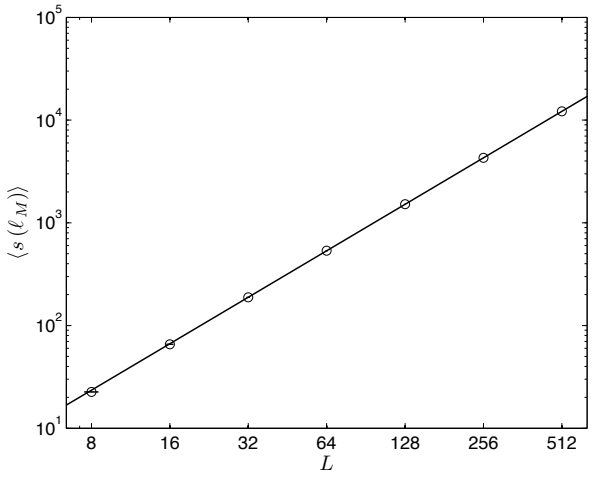

Figure 4.4: Finite size scaling of the length of longest loop, s_M of the ground state of the RK point of square lattice QDM ($|\Psi^e_{\rm TC}\rangle$). The best power law fit gives $D_f = 1.502 \pm 0.002$ which is consistent with the fractal dimension of contour loops of a gaussian height model.

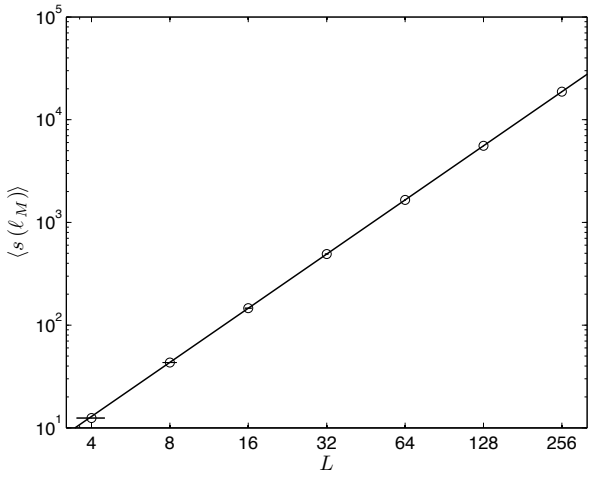

Figure 4.5: Finite size scaling of the length of the longest loop of the fully-pack loop model that describes the 2-dimer constrained RK wave function, $|\Psi^2_{\rm RK}\rangle$. The best power law fit gives $D_f = 1.7501 \pm 0.0002$ which is consistent with the fractal dimension of the effective height model.

As such the universality of the $D_f = 3/2$ for a pure Gaussian model does not apply. Indeed, for the fully packed loop model, the height model mapping predicts a fractal dimension of $D_f = 7/4$; we have confirmed this in figure 4.5 via directed loop Monte Carlo calculations of $|\Psi^2_{\rm RK}\rangle$; we find $D_f = 1.7501 \pm 0.0002$. While the fractal dimension does not distinguish the fully packed loop condensate from the gapped Z_2 loop condensed phase, they are easily distinguished by the density-density correlation function, $C(r)$; the density-density correlation function displays a power law in the critical fully packed loop model, where it vanishes exponentially in the gapped liquid phase.

Chapter 5

A quantum dimer model with a 3-dimer constraint

The chapter presents a preliminary PIGS quantum Monte Carlo study of a quantum dimer model with a local 3-dimer constraint. We thank Matthias Troyer for suggesting this model as an application for QMC calculations.

5.1 Introduction

The 3-dimer model is a variant of the canonical QDM on the triangular lattice with the hard-core dimer constraint replaced by a local constraint that each vertex is touched by 3 dimers. Unlike the square lattice, on the triangular lattice, the 3-dimer constrained Hilbert space does not map to the single dimer constraint, and is therefore a distinct Hilbert space, with distinct ground states. Just with other locally constrained models, we may expect that unusual liquid ground states may be described by a RK wave function in this Hilbert space. We discuss below how the RK wave function describes a gapped, topologically ordered liquid phase with exponentially decaying dimer-dimer correlation functions, just as is the case for the single dimer constrained QDM on the triangular lattice.

As in the canonical QDM, the minimal dynamics that do not violate the local 3-dimer constraint are flipping dimers around a rhombus plaquette with two parallel dimers and two parallel unoccupied links. Therefore, the standard QDM Hamiltonian (Eq. (5.2)) is the simplest model of quantum dynamics in this Hilbert space; here we will present PIGS QMC calculations of the ground state of this system which have allowed us to study the phase diagram of H_3 as a function of v/t.

This 3-dimer model was originally introduced by Balents *et al.* [9] in the context of a spin 1/2 Heisenberg antiferromagnet on the Kagomé lattice. They consider the case where all interactions around each hexagon of the Kagomé lattice are equal strength, such that the nearest-neighbor interaction is the same as the next and next-next neighbor interactions on

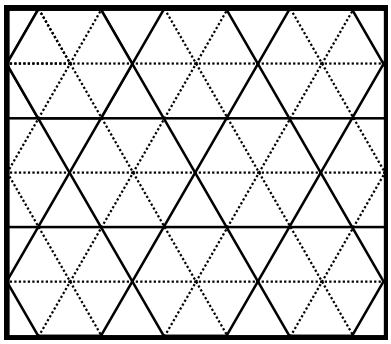

Figure 5.1: Mapping of the XXZ model on the Kagomé lattice (solid lines) to a dimer model on the triangular lattice (dashed lines). A spin on a vertex of the Kagomé lattice with $S^z = +1/2$ is considered to be a dimer on the link of the triangular lattice. The constraint $S^z_{\hexagon} = 0$ in the low energy subspace of the XXZ model becomes a constraint requiring 3 dimers to touch each vertex of the triangular lattice.

the same hexagon:

$$H_{\text{heis}} = \sum_{\hexagon} \sum_{(i,j)\in\hexagon} J\vec{S}_i \cdot \vec{S}_j.$$

Additionally, Balents *et al.* consider the case where the exchange interaction is much stronger in the z direction than in the $x-y$ plane, the so-called easy axis limit. In this limit, the Hamiltonian can be written in terms of the total spin on each hexagon $\vec{S}_{\hexagon}$:

$$H_{\text{XXZ}} = J_z \sum_{\hexagon} (S^z_{\hexagon})^2 + J_\perp \sum_{\hexagon} \Big((S^x_{\hexagon})^2 + \left(S^y_{\hexagon}\right)^2 - 3 \Big), \qquad \vec{S}_{\hexagon} \equiv \sum_{i\in\hexagon} \vec{S}_i$$

Isakov *et al.* [54, 55] used large scale QMC results to study the phase diagram H_{XXZ} as a function of $J_\perp/J_z$. They found that the ground state is a spin liquid phase for $V/t \gtrsim 20$ and undergoes a phase transition to a ferromagnet for smaller values of V/t. Recently, this phase spin liquid phase was conclusively shown to posses Z_2 topological order via QMC calculations of the topological entanglement entropy [65, 79, 56].

The spin liquid phase can be understood by considering the limit $J_z \gg J_\perp$. For $J_\perp = 0$, H_{XXZ} describes a classical model with a highly degenerate ground state, in which every spin configuration has $S^z_{\hexagon} = 0$ on every hexagon. This classical ground state subspace can be mapped to dimerizations of the triangular lattice, as follows if we consider each hexagon to be a vertex of the triangular lattice (see figure 5.1), then the links of the triangular lattice pass through the vertices of the Kagomé lattice. We then may interpret a spin on at a vertex of the Kagomè lattice with $S^z = +1/2(-1/2)$ be a link (un)occupied by a dimer. The $S^z_{\hexagon} = 0$ constraint of the spin model translates to a constraint in the dimer model such that

exactly three dimers touch each vertex. At 2nd order in $J_\perp/J_z$, the effective Hamiltonian in the 3-dimer constrained subspace is:

$$H_{\text{eff}} = -t_{\text{eff}} \sum_p \Big(\Big| \boxslash \Big\rangle \langle \boxslash | + h.c. \Big), \quad J_{\text{eff}} = \frac{J_\perp^2}{J_z}. \tag{5.1}$$

H_{eff} is simply the kinetic term of the QDM Hamiltonian. We note that the terms in equation (5.1) are independent of the link at the center of the plaquette; unlike the 1-dimer constraint, the 3-dimer constraint allows for a flippable plaquette to have a dimer along the center link.

We will now consider the full QDM Hamiltonian in the 3-dimer constrained Hilbert space by adding the usual potential energy term for parallel dimers:

$$H_3 = v \sum_p \Big(\Big| \boxslash \Big\rangle \langle \boxslash | + \Big| \boxslash \Big\rangle \langle \boxslash | \Big) - t \sum_p \Big(\Big| \boxslash \Big\rangle \langle \boxslash | + h.c. \Big), \tag{5.2}$$

where all the terms in (5.2) are independent of the state of the center link in each plaquette. At the RK point ($v = t$) the exact ground state is the equal superposition of all such 3-dimer coverings within a topological sector. Here, a topological sector is defined by the parity of the number of dimers which cross a cut along one of the axes of a torus. Balents *et al.* [9] show that the 3-dimer constrained RK ground state on the triangular lattice is a gapped dimer liquid with exponentially decaying dimer-dimer correlation functions. As with the canonical triangular lattice dimer model, we may expect that this dimer liquid persists away from the RK point for $v/t \leq 1$. Indeed, in reference 112, Sheng and Balents performed exact diagonalization of (5.2) on clusters with up to $N_l = 66$ links. They find that the dimer liquid persists down to $v/t \sim -0.5$ where there is a transition to an ordered phase. Here we will present the results of PIGS QMC calculations of the ground state of (5.2) on lattices with up to $N_l = 768$ ($L = 16$) which confirm that these results hold in the thermodynamic limit.

5.2 Phase diagram

For $v < 0$ and $|v|/t \gg 1$, configurations with the most flippable plaquettes are favored by (5.2). One such configuration is given in figure 5.2a, and it is evident that it has broken the rotational and translation symmetry of the lattice. This configuration (along with its symmetry related configurations) has $N_{fp} = N_l/2$. Additionally, any configuration with all dimers shifted by one link along any line of links with alternating occupied and unoccupied links maintains $N_{fp} = N_l/2$, such as 5.2b. Therefore in the classical limit $t = 0$, the ground state is a highly degenerate set of configurations with broken rotation symmetry.

To detect the rotational symmetry breaking we define the order parameter

$$M_{\text{rot}}^2 \equiv \frac{1}{2N_d^2} \sum_{i,j} \left(N_d^i - N_d^j \right)^2, \tag{5.3}$$

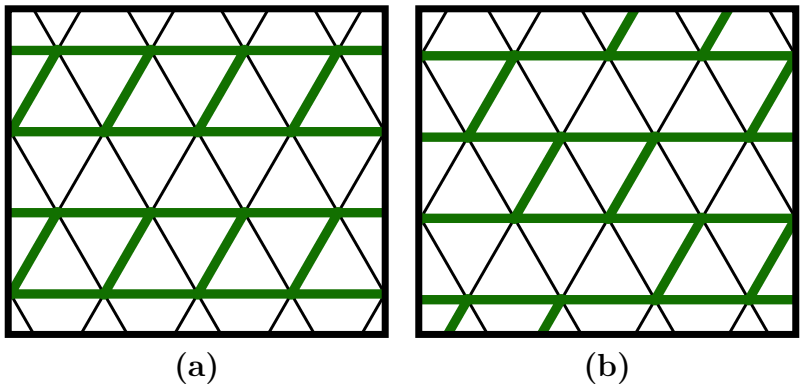

Figure 5.2: Two configurations with the maximum number of flippable plaquettes

where the sum is over the three directions of the triangular lattice. In the maximally flippable, row ordered configurations like those in figure 5.2, $N_d^i = N_l/3$, $N_d^j = N_l/6$, and $N_d^k = 0$ for any choice of i, j, k; consequently $M_{\text{rot}}^2 = 1/3$ in these configurations.

To study the ground state phase diagram way from the RK point ($v/t = 1$), we have performed PIGS QMC calculations using the RK wave function as a trial wave function to cap the imaginary time path. As seen by reference 9 and 112, the energy gap Δ in a topological sector is of the order of t at the RK point (c.f. the standard QDM on the triangular lattice, for which $\Delta \sim 0.1t$), and consequentially only moderate imaginary time paths are required for ground state convergence. We find that for $\beta t = 8$, the energies have converged to within 10^{-2}.

Figure 5.3 shows the rotational symmetry breaking order parameter plotted as a function of v/t for several lattice sizes. M_{rot}^2 appears to be vanishing in the liquid regime adjacent to the RK point ($v/t = 1$), but the rotational symmetry is broken for $v/t \lesssim -0.75$. This is consistent with a transition to the classically ordered phase, where $M_{\text{rot}}^2 = 1/3$, and M_{rot}^2 appears to be approaching $1/3$ as v/t decreases. The transition appears to be 1st order, given the discontinuous nature of the transition of M_{rot}^2 an analysis of the histogram of M_{rot}^2 at the transition would provide more definitive evidence of the order of the transition. The transition is also apparent on looking at the density of flippable plaquettes $n_{fp} = N_{fp}/N_p$, as shown in figure 5.4. These results are constant with reference 112 where the transition was found to be near $v/t \sim 0.5$ for small lattices.

5.3 Future Work

To conclusively determine the order of the phase transition we will perform a detailed analysis of the histogram of the order parameter; a double peak structure in the histogram would provide conclusive evidence of a first order phase transition. We have here presented only

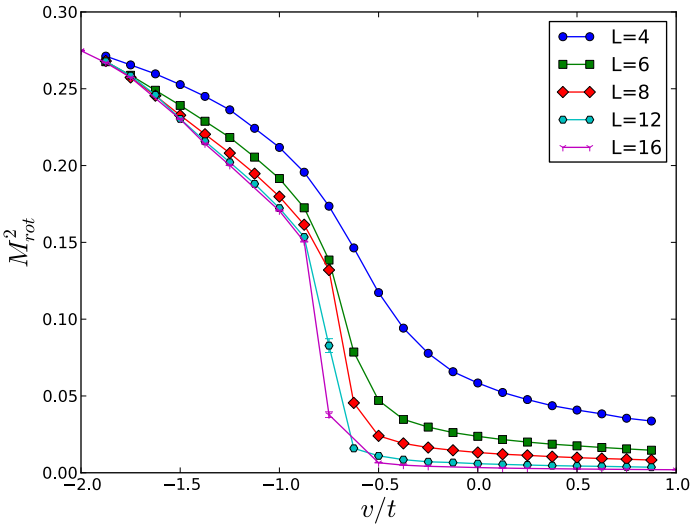

Figure 5.3: Rotational symmetry breaking order parameter for $\beta t = 8$. The dimer liquid phase persists down to $v/t \approx 0.75$, where there is a 1st order phase transition to the ordered phase. M^2_{rot} saturates to 1/3 for the classical limit $v/t \to -\infty$.

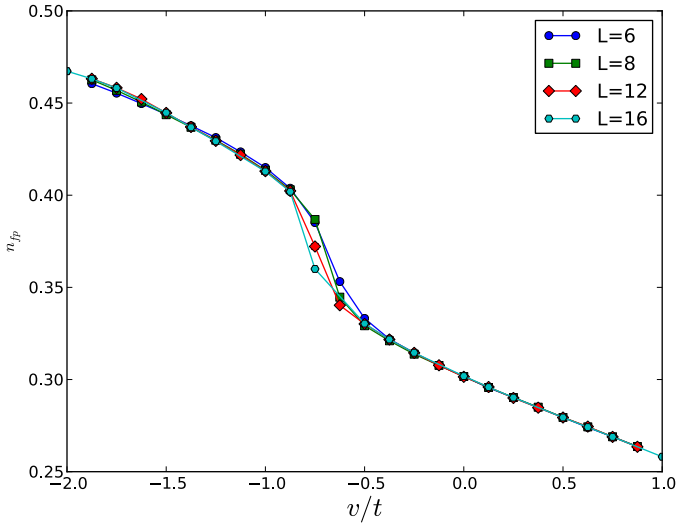

Figure 5.4: Number of flippable plaquettes $n_{fp} = \langle N_{fp}/N_p \rangle$ as a function of v/t for $\beta t = 8$. In the classical limit, the ordered phase has $N_{fp} = N_p/2$

ground state expectation values computed via QMC. The lowest energy gap in a topological sector may be computed from imaginary-time correlation functions in PIGS QMC. In particular this would allow us to compute the gap in both the dimer and vison sectors, which would determine the nature of the lowest energy excitations [57].

Chapter 6

Stroboscopic generation of topological protection

The chapter presents a proposal for the robust experimental generation of a topologically ordered phase in a system of neutral atoms trapped in an optical lattice. Much of this chapter appears in reference 50 and was done in collaboration with co-authors. Section 6.3 is greatly expanded version of what appears in reference 50 and is primarily this author's work.

6.1 Introduction

Among the most exciting aspects of quantum simulation is the possibility of generating and studying exotic quantum phases such as those possessing topological order that can be used to robustly store and process quantum information. The Hamiltonians governing these phases frequently require more-than-2-body interactions that are hard or even impossible to realize naturally. This difficulty has spurred much theoretical and experimental effort in the artificial engineering of Hamiltonians, particularly for trapped neutral atoms [80]. Many proposals have been made for the generation of 2-body Hamiltonians using static emulation schemes and some experimental realizations have appeared [44, 114]. Specific proposals have appeared for generating n-body interactions [18], but have focused on static emulation.

We present here an alternative, dynamic emulation approach to systematic generation of n-body interactions that is based on sequences of control pulses which individually realize 1- and 2-body operations on internal atomic levels. We show that this stroboscopic realization of the Hamiltonian can be implemented simultaneously with a dissipative thermalization protocol to stabilize the system from the effects of imperfect quantum operations and environmental noise. In the zero temperature limit, this can be view as replacing algorithmic error correction in an equivalent quantum circuit model with a dissipative procedure to remove errors [81]. The resource requirements for this thermalization protocol are different

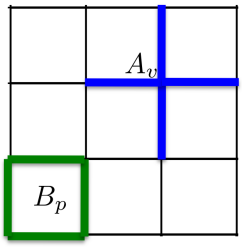

Figure 6.1: Illustration of the 4-body interactions in the toric code on the square lattice

from those of algorithmic error correction, and may be more accessible to experiment in the foreseeable future.

We illustrate the approach here with stroboscopic generation of the 4-body toric code Hamiltonian, which constitutes one of the simplest exactly solvable models with a ground state topological phase [64]:

$$H_0^{TC} = -J_e \sum_v \prod_{j \in v} \sigma_j^z - J_m \sum_p \prod_{j \in p} \sigma_j^x, \tag{6.1}$$

where σ_j denotes a Pauli operator on the links of a square lattice and v/p denote the vertex/plaquette of the lattice. The ground state of this model possesses topological order, and therefore has anyonic quasiparticle excitations and, on a lattice with periodic boundary conditions, an emergent topological degeneracy. Quantum information can be encoded in this ground state degeneracy and manipulated with controlled creation and braiding of anyons [64, 90].

In a finite sized system [97, 96, 19], the topological order of the ground state and gap to excited states protects against decoherence and loss of quantum information due to noise *provided the system is coupled to a low temperature bath*. Maintaining equilibrium with an effective low temperature bath is an essential component of topological protection, as the bath acts as an entropy sink that removes excitations caused by noise. While it is known that topological order is destroyed at any finite temperature in the thermodynamic limit [97, 96], for a finite sized system there will be a finite temperature crossover T^* below which the system will maintain topological order [19]. Consequently, topological robustness requires maintaining an effective temperature below T^* via coupling to an effective low temperature reservoir. Our analysis below will provide a scheme for generating both the toric code Hamiltonian and such an effective low temperature bath, realizing the topological protection characteristic of the toric code.

The physical context for our analysis is a set of ~ 250 individual ^{133}Cs atoms trapped at the sites of an addressable simple cubic optical lattice [91]. A lattice spacing of 5 μm [91] allows essentially perfect addressability [12]. The orbital degrees of freedom are frozen on

the time scales relevant to our analysis and we need consider only internal atomic degrees of freedom. Two hyperfine levels (e.g., $|F, m_F\rangle = |4,4\rangle, |3,3\rangle$) define a 2-level pseudospin system. We realize $H_{\rm TC}$ in the interaction representation defined by the pseudospin energies. Auxiliary internal levels are used to realize 1-spin and 2-spin quantum operations, using optical frequency Raman pulses to generate arbitrary single-spin operations and excitation of one atom to a Rydberg state, e.g., the $n \approx 80$ state, to generate controlled-phase gates, CPHASE [59]. To achieve thermalization or cooling, the Hamiltonian $H_{\rm TC}$ is supplemented by coupling the primary system spins to an ancillary set of pseudospins that will be dissipatively controlled to simulate a thermal reservoir. Since the pseudospins are localized at the sites of a cubic lattice, one can choose to either realize $H_{\rm TC}$ on a single plane using a surface code [15] or in a three-dimensional cubic array with toroidal boundary conditions realized by SWAP operations.

6.2 Effective Hamiltonian Evolution

Given the ability to perform both Rydberg-induced CPHASE gates between atoms in neighboring sites and arbitrary 1-body rotations, $\exp(-i\theta\sigma_j)$, on individual atoms, where θ is a variable phase angle, sequences of these operations can be chosen to generate effective *n-body* interactions through high-order terms in the Magnus expansion [67], allowing stroboscopic simulation of a broad class of Hamiltonians. Consider the operator sequence, $U_n U_{n-1} \cdots U_2 U_1$, where the U_j are the 1- or 2-body gates described above. Effective interactions are found through:

$$\begin{aligned} H_{\rm eff}(t) &\equiv \frac{i\hbar}{t} \ln(U_n U_{n-1} \cdots U_2 U_1) \\ &= \sum_j \frac{i\hbar}{t} \ln U_j - \sum_{j<k} \frac{i\hbar}{2t} [\ln U_j, \ln U_k] + \mathcal{O}\left(||\ln U||^3\right). \end{aligned}$$

Consider now simulation of the 4-body interactions in $H_0^{\rm TC}$. We use the notation $U_j(\phi) \equiv e^{-i\phi\Sigma_j}$ and define $\Sigma_1 = \sigma^z\sigma^y\sigma^0\sigma^0$, $\Sigma_2 = \sigma^0\sigma^x\sigma^y\sigma^0$, and $\Sigma_3 = \sigma^0\sigma^0\sigma^x\sigma^z$, where σ^0 is the identity operator. For simplicity, it is assumed that each $U_j(\alpha)$ takes a time τ to execute. We construct the operator sequence,

$$U_{123}(\alpha,\beta,\gamma) = U_{12}(\alpha,\beta)U_3(\gamma)U_{12}^\dagger(\alpha,\beta)U_3^\dagger(\gamma), \tag{6.2}$$

where $U_{12}(\alpha,\beta) = U_2(\beta)U_1(\alpha)U_2^\dagger(\beta)U_1^\dagger(\alpha)$. This sequence acts over a time 10τ to generate the following effective Hamiltonian at a single vertex, v:

$$\begin{aligned} H_{\rm eff}^{zzzz} =& J_e \prod_{j\in v} \sigma_j^z + \frac{\chi}{\alpha\gamma}\left(\alpha\left[\sigma^0\sigma^x\sigma^z\sigma^z\right]_v + \gamma\left[\sigma^z\sigma^z\sigma^y\sigma^0\right]_v\right) \\ &+ \chi\left(\left[\sigma^0\sigma^x\sigma^y\sigma^0\right]_v - 2\beta/\gamma\left[\sigma^0\sigma^0\sigma^x\sigma^z\right]_v\right) + \mathcal{O}\left(\phi^6\right) \end{aligned}$$

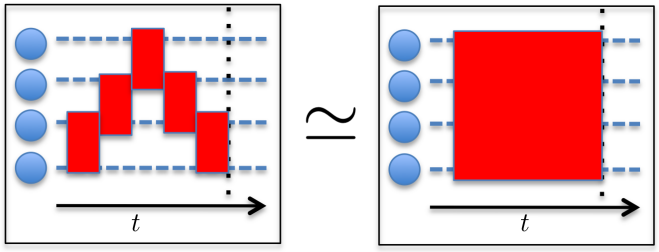

Figure 6.2: Schematic illustration of the stroboscopic generation of 4-body interactions

where $[O]_{v/p}$ denotes the application of the (up to) four-body operator O to the spins meeting at a vertex v or surrounding a plaquette p; we choose $|\alpha| = |\beta| = |\gamma| \equiv \phi$; and $J_e = \chi\left(1-3\phi^2\right)/\alpha\gamma + \mathcal{O}(\phi^6)$ with $\chi \equiv \alpha^2\beta\gamma^2\left(2\hbar/5\tau\right)$. By repeating the operator sequence a second time with sign reversals $\alpha \to -\alpha$ and $\gamma \to -\gamma$, we cancel the fourth order terms in ϕ, giving $U_{123}(-\alpha,\beta,-\gamma)U_{123}(\alpha,\beta,\gamma)$ that acts for a time 20τ to generate the effective Hamiltonian

$$H_{\text{eff}}^{zzzz} = J_e \prod_{j\in v}\sigma_j^z + \chi\left[\sigma^0\sigma^x\sigma^y\sigma^0\right]_v + \mathcal{O}\left(\phi^6\right). \tag{6.3}$$

The sequence $U_{123}(-\alpha,\beta,-\gamma)U_{123}(\alpha,\beta,\gamma)$ is specifically designed to cancel the lowest-order (ϕ^4) perturbation terms without affecting the gap. The remaining ϕ^5 term is a 2-body perturbation to H_{TC}. Repeating this sequence with appropriate sign reversals will cancel these higher order terms. However, the ground state subspace of H_{TC} is robust to these remaining perturbations, as we discuss below. A shorter operator sequence may then be preferable to reduce gate errors. The plaquette operator, H_{eff}^{xxxx}, can be generated by cyclic permutation of the Pauli operators in the above expressions for Σ_1, Σ_2 and Σ_3.

Simulation of H_0^{TC} then requires application of the pulse sequence to all vertices and plaquettes conforming to a two dimensional square lattice with periodic boundary conditions. Vertex and plaquette terms may be applied serially as: $\exp\left(-iH_{\text{eff}}^{xxxx}t/\hbar\right)\exp\left(-iH_{\text{eff}}^{zzzz}t/\hbar\right) \approx \exp -i\left(H_{\text{eff}}^{xxxx}+H_{\text{eff}}^{zzzz}\right)t/\hbar$. Because only the perturbation terms fail to commute, the truncation error in the above expression occurs at orders larger than ϕ^7. For 18 pseudospins, representing a 3×3 system with toroidal boundary conditions, a completely serial implementation yields a stroboscopic cycle time of 720μs using the estimate $\tau \sim 500$ns [131] and the minimal count of one CPHASE and four 1-spin gates to realize all $U_j(\alpha)$ [134]. This may be reduced by implementing some operators in parallel.

6.3 Simulated Thermalization

The pseudospin subspace of the system is an open quantum system that will interact with the external environment through the controlled quantum operations in the above pulse sequences and uncontrolled noisy interactions. Unlike a solid state system, for which system-environment interactions might be expected to lead to thermal equilibration, noise in the optical lattice system will not generally drive the simulation subspace to a state that is thermal under the simulated Hamiltonian.

If the simulation subspace is described in the interaction picture of the system, physical couplings to a thermal reservoir may drive the simulation subspace to either a negative or infinite temperature state, or to a non-thermal state under the simulated Hamiltonian [17]. As a trivial example, consider simulating the Hamiltonian $H_{sim} = 0$ in the interaction picture of a single qubit with a physical energy spitting Δ between states $|0\rangle$ and $|1\rangle$. Under H_{sim} these states are degenerate, but physical coupling to a zero temperature reservoir drives the system to $|0\rangle$, which is non-thermal under H_{sim}.

Additionally, noise in the above sequence of control gates will add entropy and effectively heat the system. To estimate the entropy produced by noisy control gates under a simple a simple model of gate noise, consider a unitary gate $U(\phi) = e^{i\phi\Sigma}$, where Σ is a Hermitian operator with $\Sigma^2 = \mathbb{1}$. We assume that there is weak noise in the rotation angle ϕ such that under the action of $U_\epsilon(\phi)$,

$$\rho_0 \rightarrow \rho'(\phi) \simeq U(\epsilon)\rho(\phi)U^\dagger(\epsilon),$$

where $\rho(\phi) \equiv U(\phi)\rho(\phi)U^\dagger(\phi)$, and $\epsilon \ll 1$ and is normally distributed about 0 with variance EPG (error per gate). The linear entropy,

$$S_{lin} \equiv 2\ln 2(1 - \mathrm{Tr}\,\rho^2), \tag{6.4}$$

is a lower bound on the entropy that is exact for both pure and fully mixed states. To first order in EPG:

$$S_{lin}\big(\rho'(\phi)\big) \simeq 2\ln 2\left[1 - \mathrm{Tr}\left(\rho(\phi)^2\right) + \mathrm{EPG}\Big\{2\mathrm{Tr}\left(\rho(\phi)^2\right) - \mathrm{Tr}\,(\rho_0\Sigma\rho_0\Sigma) - \mathrm{Tr}\,(\Sigma\rho_0\Sigma\rho_0)\Big\}\right]$$

The maximum increase in entropy occurs when ρ_0, and therefore $\rho(\phi)$, are pure states. This gives an estimate for the maximum increase in entropy under $U_\epsilon(\phi)$:

$$\Delta S_{max} \simeq S_{lin}\big(\rho'(\phi)\big) - S\big(\rho_0\big) \simeq 4\ln 2 \times \mathrm{EPG} \tag{6.5}$$

Given a system at temperature T for which $U_\epsilon(\phi)$ is applied at a frequency Ω, the effective heating rate of the system due to the noisy gate is then $\Gamma_e \approx 4\ln 2(\mathrm{EPG})\Omega T$. Quantum circuit models are usually supplemented by error correction schemes to effectively remove entropy from the system. We take a different approach here, stroboscopically constructing an effective system-reservoir interaction to control system entropy and produce a thermal state. We first present the general approach for finite temperature and then a simplification for ground state cooling.

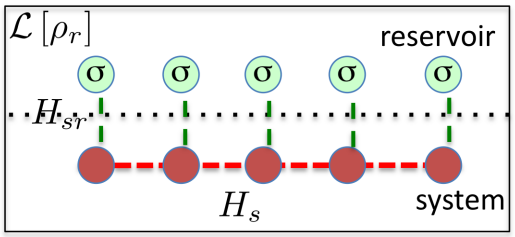

Figure 6.3: Schematic illustration of the coupling to a set of dissipative pseudospings

6.3.1 Themalization from non-unitary dynamics

To maintain the simulated system at a thermal steady state we add a "thermalization" interaction $H_{sys-res}$ of the system pseudospins with a set of ancillary pseudospins. Consider a Hamiltonian with local n-body interactions of the form:

$$H_0 = -\sum_{\nu} A_\nu \sum_{n(i)} h^\nu_{n(i)}. \tag{6.6}$$

In Eq. (6.6), $h^\nu_{n(i)}$ is an n-body operator involving a neighborhood of pseudo-spins, $n(i)$, including spin i, with eigenvalues ± 1, ν labels the type of interaction, and A_ν is a constant. Additionally we define the pseudospin flip operator Σ^ν_i such that $\Sigma^\nu_i |h^\nu_{n(i)} = \pm 1\rangle = |h^\nu_{n(i)} = \mp 1\rangle$. When all $[h^\nu_{n(i)}, h^\mu_{n(j)}] = 0$, as is the case for H_0^{TC} (Eq. (6.1)), we can define the local excitation creation and translation operators:

$$\begin{aligned} E^\dagger_{i,\nu} &= \frac{1}{4}\Sigma^\nu_i \left(\mathbb{1} + h^\nu_{n(i)}\right)\left(\mathbb{1} + h^\nu_{n'(i)}\right) \\ T_{i,\nu} &= \frac{1}{4}\Sigma^\nu_i \left(\mathbb{1} - h^\nu_{n(i)}\right)\left(\mathbb{1} + h^\nu_{n'(i)}\right). \end{aligned} \tag{6.7}$$

where $E^\dagger_{i,\nu}$ and $T_{i,\nu}$ are $(2n-1)$-body interactions; $E^\dagger_{i,\nu}$ creates a pair of excitations about i and $T_{i,\nu}$ translates an excitation about i. The energy gap for creation of a pair of excitations of type ν is $\Delta_\nu = 4A_\nu$.

A route to guaranteeing the thermal equilibration of this system is for it to evolve under the Lindblad master equation

$$\dot{\rho} = -i/\hbar\,[H_0, \rho] + L[\rho], \tag{6.8}$$

where ρ is the density matrix and $L[\rho]$ is the superoperator:

$$L[\rho] = \sum_{\omega} \left(2c_\omega \rho c^\dagger_\omega - c^\dagger_\omega c_\omega \rho - \rho c^\dagger_\omega c_\omega\right), \tag{6.9}$$

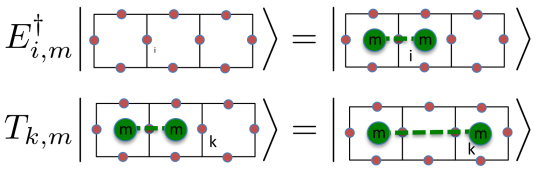

Figure 6.4: Illustration of local excitation creation and translation operators

and where $c_\omega(c_\omega^\dagger)$ are the Lindblad operators. With the following choice:

$$\{c_\omega\} = \{\sqrt{\frac{(1-p_\nu)}{2}\lambda^*}E_{i,\nu}, \sqrt{\frac{p_\nu}{2}\lambda^*}E_{i,\nu}^\dagger, \sqrt{\frac{\gamma^*}{4}}T_{i,\nu}, \sqrt{\frac{\gamma^*}{4}}T_{i,\nu}^\dagger\} \tag{6.10}$$

the unique stationary state of the master equation can be shown to be the thermal state under H_0 [3, 2]. For cooling towards the ground state of H_0, the Lindblad operators can be reduced to the n-body terms [24, 76, 130] $\{\sqrt{\lambda^*}(E_{i,\nu}+T_{i,\nu}), \sqrt{\lambda^*}(E_{i,\nu}+T_{i,\nu}^\dagger)\}$. It may also be possible to approximately generate (6.9) with 2-body system-bath interactions [3, 2].

To explicitly demonstrate that the thermal state is indeed the stationary state of (6.8), we will consider the evolution of the diagonal element $\langle\psi_n|\,\rho^s\,|\psi_n\rangle = P_n$. Here $|\psi_n\rangle$, and the states $|\psi_{n'_{i,\nu}}\rangle$, $|\psi_{n''_{i,\nu}}\rangle$, and $|\psi_{n'''_{i,\nu}}\rangle$, which are defined by:

$$\begin{aligned}
|\psi_{n'_{i,\nu}}\rangle &= E_{i,\nu}|\psi_n\rangle, \quad |\psi_{n''_{i,\nu}}\rangle = E_{i,\nu}^\dagger|\psi_n\rangle \\
|\psi_{n'''_{i,\nu}}\rangle &= \left(T_{i,\nu}+T_{i,\nu}^\dagger\right)|\psi_n\rangle
\end{aligned}$$

are eigenstates of H_0. Under Eq. (6.10), $P_n\,(t)$ evolves according to:

$$\begin{aligned}
\frac{dP_n}{dt} = \lambda^*\sum_{n'_{i,\nu}}\Big(-(1-p_\nu)P_n + p_\nu P_{n'_{i,\nu}}\Big) + \lambda^*\sum_{n''_{i,\nu}}\Big(-p_\nu P_n + (1-p_\nu)P_{n''_{i,\nu}}\Big) \\
+ \frac{\gamma^*}{4}\sum_{n'''_{i,\nu}}\Big(-P_n + P_{n'''_{i,\nu}}\Big)
\end{aligned} \tag{6.11}$$

A stationary state of (6.11) satisfies detailed balance:

$$\frac{P_{n'_{i,\nu}}}{P_n} = \frac{1-p_\nu}{p_\nu}, \quad \frac{P_{n''_{i,\nu}}}{P_n} = \frac{p_\nu}{1-p_\nu}, \quad \frac{P_{n'''_{i,\nu}}}{P_n} = 1$$

Ergodicity of the operators $\{E_{i,\nu}, E_{i,\nu}^\dagger, T_{i,\nu}, T_{i,\nu}^\dagger\}$ in the Hilbert space ensures [63] that the unique stationary solution to Eq. (6.11) is $P_n\,(t\to\infty) = e^{-E_n/T}/Z$, where the temperature T is defined by $T = -\Delta_\nu/\ln p_\nu$, $E_n|\psi_n\rangle = H_0|\psi_n\rangle$, and $Z = \sum_n e^{-E_n/T}$.

Now consider the evolution an off-diagonal density matrix element $\rho^s_{mn} \equiv \langle \psi_m \mid \rho \mid \psi_m \rangle \psi_n$ under Eq. (6.10):

$$\frac{d\rho_{mn}}{dt} = -\Gamma_{mn}\rho_{mn} + \lambda^* \sum_{\left(m'_{i,\nu}, n'_{i,\nu}\right)} p_\nu \rho_{m'_{i,\nu} n'_{i,\nu}} + \lambda^* \sum_{\left(m''_{i,\nu}, n''_{i,\nu}\right)} (1-p_\nu)\rho_{m''_{i,\nu} n''_{i,\nu}} + \frac{\gamma^*}{2} \sum_{\left(m'''_{i,\nu}, n'''_{i,\nu}\right)} \rho_{m'''_{i,\nu} n'''_{i,\nu}} \tag{6.12}$$

where Γ_{nm} is the positive constant:

$$\Gamma_{nm} \equiv \frac{\lambda^*}{2} \sum_{i,\nu} \sum_{q=m,n} (1-p_\nu) \left\langle \psi_q \mid E^\dagger_{i,\nu} E_{i,\nu} \mid \psi_q \right\rangle + \frac{\lambda^*}{2} \sum_{i,\nu} \sum_{q=m,n} p_\nu \left\langle \psi_q \mid E_{i,\nu} E^\dagger_{i,\nu} \mid \psi_q \right\rangle + \frac{\gamma^*}{4} \sum_{i,\nu} \sum_{q=m,n} \left\langle \psi_q \mid T_{i,\nu} T^\dagger_{i,\nu} + T^\dagger_{i,\nu} T_{i,\nu} \mid \psi_q \right\rangle$$

Clearly, $\rho^s_{mn} = 0$ for all $m \neq n$ is a stationary state of Eq. (6.12). The stationary state of both Eqs. (6.11)& (6.12) is the thermal state $\rho^S_{th} \equiv \sum_n e^{-\frac{E_n}{T}} |\psi_n\rangle\langle\psi_n|$. Additionally, Eq. (6.11) describes the brownian motion of excitations. The γ^* term generates incoherent hopping of isolated local excitations, and consequently $\frac{\gamma^*}{2}$ acts as the diffusion constant. For a given choice of mobility μ, γ^* can be chosen such that $\gamma^* = \mu T$. We not that while in principle there could a different temperature for each type of excitation defined by $T_\nu = -\Delta_\nu / \ln p_\nu$, this would lead to a non-thermal equilibrium state, so we assume that $\{p_n u\}$ are chosen such that $T_\nu = T$ for all ν.

6.3.2 Generating thermalization from dissipative pseudospins

To generate Lindbland evolution of the form Eq. (6.10), we'll consider interacting the system locally with an ancillary pseudospin undergoing strong dissipation. Consider two eigenstates of H_0, $|\phi_a\rangle$, $|\phi_b\rangle$ where $|\phi_b\rangle = E^\dagger_{i,\nu} |\phi_a\rangle$. The system will interact locally with an ancillary pseudospin $\sigma_{i_t,\nu}$ via

$$H^{int}_{i_t,\nu} = g E^\dagger_{i,\nu} \sigma^-_{i_t,\nu} + h.c. \tag{6.13}$$

where $\sigma_{i_t,\nu}$ is undergoing dissipation such that the total density matrix of the system and ancilla in the interaction representation of H_0, ρ, evolves according to the master equation:

$$\begin{aligned} \dot{\rho} &= -i/\hbar \left[H^{int}_{i,\nu}, \rho\right] + L[\rho] \\ L[\rho] &= -\frac{1-p}{2}\lambda \left[\sigma^+_{i,\nu}\sigma^-_{i,\nu}\rho - \sigma^-_{i,\nu}\rho\sigma^+_{i,\nu}\right] - \frac{p}{2}\lambda \left[\rho\sigma^-_{i,\nu}\sigma^+_{i,\nu} - \sigma^+_{i,\nu}\rho\sigma^-_{i,\nu}\right] + h.c. \end{aligned} \tag{6.14}$$

Taking the basis states of the system+ancilla pseudospin in the system subspace $\{|\psi_a\rangle, |\psi_b\rangle\}$ to be:

$$
\begin{aligned}
|\phi_0\rangle &= |\psi_a\rangle|\downarrow_{i,\nu}\rangle \\
|\phi_1\rangle &= \frac{1}{\sqrt{2}}\left(|\psi_a\rangle|\uparrow_{i,\nu}\rangle - |\psi_b\rangle|\downarrow_{i,\nu}\rangle\right) \\
|\phi_2\rangle &= \frac{1}{\sqrt{2}}\left(|\psi_a\rangle|\uparrow_{i,\nu}\rangle + |\psi_b\rangle|\downarrow_{i,\nu}\rangle\right) \\
|\phi_3\rangle &= |\psi_b\rangle|\uparrow_{i,\nu}\rangle
\end{aligned}
$$

$\dot{\rho}$ decouples into three independently coupled sets of dynamical equations. We see that ρ_{03} is decoupled from all other terms and decays according to:

$$
\dot{\rho}_{03} = -\frac{\lambda}{2}\Big(1 + i2\frac{g}{\lambda}\Big)\rho_{03} \Rightarrow \rho_{03}(t) = \rho_{03}(t=0)\, e^{-\frac{\lambda}{2}t} e^{-igt}
$$

The second set of coupled equations only involves off-diagonal terms:

$$
\begin{aligned}
\dot{\rho}_{01} &= -\frac{1}{4}\lambda\left((1+2p) + i4\frac{g}{\lambda}\right)\rho_{01} - \frac{1-2p}{4}\lambda\rho_{02} - \frac{1-p}{2}\lambda\rho_{13} - \frac{1-p}{2}\lambda\rho_{23} \\
\dot{\rho}_{02} &= -\frac{1}{4}\lambda\left((1+2p) - i4\frac{g}{\lambda}\right)\rho_{02} - \frac{1-2p}{4}\lambda\rho_{01} + \frac{1-p}{2}\lambda\rho_{13} + \frac{1-p}{2}\lambda\rho_{23} \\
\dot{\rho}_{13} &= -\frac{3}{4}\lambda\left(\left(1 - \frac{2}{3}p\right) - i\frac{4}{3}\frac{g}{\lambda}\right)\rho_{13} - \frac{1-2p}{4}\lambda\rho_{23} - \frac{p}{2}\lambda\rho_{01} + \frac{p}{2}\lambda\rho_{02} \\
\dot{\rho}_{23} &= -\frac{3}{4}\lambda\left(\left(1 - \frac{2}{3}p\right) + i\frac{4}{3}\frac{g}{\lambda}\right)\rho_{23} - \frac{1-2p}{4}\lambda\rho_{13} - \frac{1-p}{2}\lambda\rho_{01} - \frac{1-p}{2}\lambda\rho_{02}
\end{aligned}
\tag{6.15}
$$

The solution to (6.15) is:

$$
\begin{aligned}
\rho_{01}(t) &= \left(\gamma + i4\frac{g}{\lambda}\right) C_1^o e^{-\frac{3}{4}\left(1+\frac{\gamma}{3}\right)\lambda t} + (1-p)\left(\gamma + i4\frac{g}{\lambda}\right) C_2^o e^{-\frac{1+\gamma}{2}\frac{\lambda}{2}t} \\
&\quad + \left(-\gamma + i4\frac{g}{\lambda}\right) C_3^o e^{-\frac{3}{4}\left(1-\frac{\gamma}{3}\right)\lambda t} + (1-p)\left(-\gamma + i4\frac{g}{\lambda}\right) C_4^o e^{-\frac{1-\gamma}{4}\lambda t} \\
\rho_{02}(t) &= -C_1^o e^{-\frac{3}{4}\left(1+\frac{\gamma}{3}\right)\lambda t} + (1-p) C_2^o e^{-\frac{1+\gamma}{2}\frac{\lambda}{2}t} - C_3^o e^{-\frac{3}{4}\left(1-\frac{\gamma}{3}\right)\lambda t} + (1-p) C_4^o e^{-\frac{1-\gamma}{4}\lambda t} \\
\rho_{13}(t) &= C_1^o e^{-\frac{3}{4}\left(1+\frac{\gamma}{3}\right)\lambda t} + pC_2^o e^{-\frac{1+\gamma}{2}\frac{\lambda}{2}t} + C_3^o e^{-\frac{3}{4}\left(1-\frac{\gamma}{3}\right)\lambda t} + pC_4^o e^{-\frac{1-\gamma}{4}\lambda t} \\
\rho_{23}(t) &= \left(\gamma + i4\frac{g}{\lambda}\right) C_1^o e^{-\frac{3}{4}\left(1+\frac{\gamma}{3}\right)\lambda t} - p\left(\gamma + i4\frac{g}{\lambda}\right) C_2^o e^{-\frac{1+\gamma}{4}\lambda t} \\
&\quad + p\left(-\gamma + i4\frac{g}{\lambda}\right) C_3^o e^{-\frac{3}{4}\left(1-\frac{\gamma}{3}\right)\lambda t} + p\left(\gamma - i4\frac{g}{\lambda}\right) C_4^o e^{-\frac{1-\gamma}{4}\lambda t}
\end{aligned}
$$

where $\{C_i^o\}$ are constants that depend on the initial conditions and

$$\gamma \equiv \sqrt{1-16\left(\frac{g}{\lambda}\right)^2} \simeq 1-8\left(\frac{g}{\lambda}\right)^2 \tag{6.16}$$

for $g \ll \lambda$. By tracing over the ancillary pesudospin, we can solve for the evolution of offdiagonal element of the reduced density matrix for the system, $\rho^s(t)$:

$$\begin{aligned}\rho_{ab}^s(t) &= \left(1-\gamma-i4\frac{g}{\lambda}\right)C_2^o e^{-\frac{1+\gamma}{2}\frac{\lambda}{2}t} + \left(1+\gamma-i4\frac{g}{\lambda}\right)C_4^o e^{-\frac{1-\gamma}{4}\lambda t} \\ &= 2C_4^o e^{-\frac{\lambda^*}{2}\lambda t} + \mathcal{O}\left(\frac{g}{\lambda}\right)\end{aligned} \tag{6.17}$$

where $\lambda^* \equiv \frac{1-\gamma}{2}\lambda \simeq 4\left(\frac{g}{\lambda}\right)^2\lambda$. Therefore the effective evolution of $\rho_{ab}^s(t)$ is:

$$\dot{\rho}_{01}^s(t) \simeq -\frac{\lambda^*}{2}\rho_{ab}^s(t). \tag{6.18}$$

The final set of independently coupled equations involves the diagonal elements of ρ:

$$\begin{aligned}\dot{Re}[\rho_{12}] &= -2gIm[\rho_{12}] - \frac{\lambda}{4}(\rho_{33}-\rho_{00}+2Re[\rho_{12}]) - \frac{(1-p)\lambda - p\lambda}{4} \\ \dot{Im}[\rho_{12}] &= 2gRe[\rho_{12}] - \frac{\lambda}{2}Im[\rho_{12}] \\ \dot{\rho_{00}} &= -\left(p\lambda + \frac{(1-p)\lambda}{2}\right)\rho_{00} - \frac{(1-p)\lambda}{2}(\rho_{33}-1) + (1-p)\lambda Re[\rho_{12}] \\ \dot{\rho_{33}} &= -\left((1-p)\lambda + \frac{p\lambda}{2}\right)\rho_{33} - \frac{p\lambda}{2}(\rho_{00}-1) - p\lambda Re[\rho_{12}]\end{aligned} \tag{6.19}$$

The solution to (6.19) is:

$$\begin{aligned}Re[\rho_{12}](t) &= \frac{\gamma}{2}C_3^d e^{-\frac{1+\gamma}{2}\lambda t} - \frac{\gamma}{2}C_3^d e^{-\frac{1-\gamma}{2}\lambda t} \\ Im[\rho_{12}](t) &= -\frac{C_2^d}{8}e^{-\frac{\lambda}{2}t} - 2\frac{g}{\lambda}C_3^d e^{-\frac{1+\gamma}{2}\lambda t} - 2\frac{g}{\lambda}C_3^d e^{-\frac{1-\gamma}{2}\lambda t} \\ \rho_{00}(t) &= (1-p)^2 - (1-p)C_3^d e^{-\frac{1-\gamma}{2}\lambda t} - (1-p)\frac{g}{\lambda}C_2^d e^{-\frac{\lambda}{2}t} - (1-p)C_3^d e^{-\frac{1+\gamma}{2}\lambda t} + C_1^d e^{-\lambda t} \\ \rho_{33}(t) &= p^2 + C_1^d e^{-\lambda t} + pC_2^d\frac{g}{\lambda}e^{-\frac{\lambda}{2}t} + pC_3^d e^{-\frac{1+\gamma}{2}\lambda t} + pC_3^d e^{-\frac{1-\gamma}{2}\lambda t}\end{aligned} \tag{6.20}$$

where $\{C_1^d, C_2^d, C_3^d\}$ are constants that depend on the initial conditions. Tracing over the ancilla pseudospin, in the limit $g \gg \lambda$ we arrive at:

$$\begin{aligned}\rho_{aa}^s(t) &= (1-p) - \frac{C_3^d}{2}(1+\gamma)e^{-\frac{1-\gamma}{2}\lambda t} - \frac{C_3^d}{2}(1-\gamma)e^{-\frac{1+\gamma}{2}\lambda t} + \frac{g}{\lambda}C_2^d e^{-\frac{\lambda}{2}t} \\ &= (1-p) - C_3^d e^{-\lambda^* t} + \mathcal{O}\left(\frac{g}{\lambda}\right)\end{aligned} \tag{6.21}$$

We therefore see that the diagonal elements of ρ^s relax to a thermal population according to:

$$\begin{aligned}\dot{\rho}^s_{aa}(t) &\simeq -\lambda^*\left(\rho^s_{aa} - p\right)\\ \dot{\rho}^s_{bb}(t) &\simeq -\lambda^*\left(\rho^s_{bb} - (1-p)\right)\end{aligned} \tag{6.22}$$

The evolution of Eqs. (6.18)& (6.22) is generated by the Lindblad evolution:

$$L[\rho^s] = -\frac{(1-p)\lambda^*}{2}\left[E^\dagger_{i,\nu}E_{i,\nu}\rho^s - E_{i,\nu}\rho^s E^\dagger_{i,\nu}\right] - \frac{p\lambda^*}{2}\left[\rho^s E_{i,\nu}E^\dagger_{i,\nu} - E^\dagger_{i,\nu}\rho^s E_{i,\nu}\right] + h.c.$$

Similarly, if we couple the system to an ancillary pseudospin that is relaxing to the fully mixed state, $\sigma_{i_m,\nu}$, via:

$$\begin{aligned}\dot{\rho} &= -i/\hbar\left[H^{int}_{i_m,\nu},\rho\right] + L[\rho], \qquad H^{int}_{i_m,\nu} = gT^\dagger_{i,\nu}\sigma^-_{i_m,\nu} + h.c.\\ L[\rho] &= -\frac{\gamma}{4}\left[\sigma^+_{i_m,\nu}\sigma^-_{i_m,\nu}\rho - \sigma^-_{i_m,\nu}\rho\sigma^+_{i_m,\nu}\right] - \frac{\gamma}{4}\left[\rho\sigma^-_{i_m,\nu}\sigma^+_{i_m,\nu} - \sigma^+_{i_m,\nu}\rho\sigma^-_{i_m,\nu}\right] + h.c.\end{aligned} \tag{6.23}$$

the effective Lindblad evolution of the system is:

$$L[\rho^s] = -\frac{\gamma^*}{4}\left[T^\dagger_{i,\nu}T_{i,\nu}\rho^s - T_{i,\nu}\rho^s T^\dagger_{i,\nu}\right] - \frac{\gamma^*}{4}\left[\rho^s T_{i,\nu}T^\dagger_{i,\nu} - T^\dagger_{i,\nu}\rho^s T_{i,\nu}\right] + h.c.$$

with $\gamma \simeq 4\left(\frac{g}{\lambda}\right)^2\gamma$. If each system pseudospin is coupled to a thermally relaxing ancillary pseudospin $\sigma_{i_t,\nu}$ and an ancillary pseudospin relaxing to a fully mixed state, $\sigma_{i_m,\nu}$ for every excitation type, in the $g \ll \lambda, \gamma$ limit, where no correlations can develop between ancillary pseudospins, the total Lindblad evolution is given by Eq. (6.10).

In this limit the ancillary pseudospins become an effective low temperature bath with a cooling rate $\Gamma_c \sim 4g^2/\lambda$ and heating rate determined by gate errors and any environmental noise. Competition between these rates leads to a minimum reachable temperature for the system, which can be estimated as $T_{\min} \sim \Delta/\ln(\Gamma_c/\Gamma_e)$, where $\Gamma_e \sim \text{EPG} \times \Omega$, with EPG and Ω the error per gate and frequency of application of the most noisy gate.

We emphasize here that the discussion above only applies to stabilizer-like Hamiltonians where all the local terms commute; the eigenstates of these Hamiltonians are therefore eigenstates of the local operators, and excitations are localized. Consequently the local system-bath coupling described above can directly generate a thermal stationary state under the Lindblad dynamics, as we have shown above. However, a generic Hamiltonian will have non-commuting terms and thus will not in general have localized excitations. For system with translational invariance, we expect excitations to be propagating modes, and thus it is not clear that such a local-system bath interaction will be able to stabilize a thermal state [8].

6.4 Optical Lattice Implementation

The Lindblad master equation, with operators given by Eq. (6.10), generates a *unitary* system-reservior interaction but *nonunitary* reservoir relaxation. Stroboscopic simulation of $H_{\rm sr}$ is performed in a manner analogous to the $H_{\rm TC}$ simulation described above. Phase angles are chosen in the 1- and 2-body gates to generate an effective static interaction strength g over the time t_{sr} between applications of H_{sr}, such that $gt_{sr}/\hbar < \pi/2$. Nonunitary evolution of the reservoir is generated by encoding the reservoir as two levels of a Λ-system. The pseudospin states are the ground state $|0\rangle$ and the meta-stable state $|1\rangle$. State $|2\rangle$ is chosen to have fast spontaneous emission to $|0\rangle$, with rate Γ_{20}. This spontaneous emission is the decoherence mechanism required to generate the nonunitary Lindblad evolution. The ancillary pseudospin levels can be placed in a thermal state via the following procedure:

1. π-pulse on the $|1\rangle \rightarrow |2\rangle$ transition.
2. Wait for decay to ground state, $|0\rangle$.
3. π-pulse on $|0\rangle \rightarrow |1\rangle$ transition.
4. θ-pulse on the $|1\rangle \rightarrow |2\rangle$ transition.
5. Wait for decay, which now yields the final pseudospin state, $\rho = \mathrm{diag}\left\{\sin^2(\theta), \cos^2(\theta)\right\}$, corresponding to an effective temperature:

$$T_{\rm eff} = \Delta / \left(2 \ln\left(\cot\theta\right)\right). \tag{6.24}$$

The above stroboscopic procedure generates $\lambda^* \approx g^2 t_{sr}/\hbar^2$ in Eq. (6.10). The procedure can be simplified in the limit of cooling towards zero temperature by eliminating steps 3-5, when it becomes similar to the optical pumping scheme employed in measurement of qubit states for trapped ions [133]. This thermalization procedure is then repeated and interleaved with the stroboscopic application of H_0.

$H_0^{\rm TC}$ is in the local form of H_0, with two types of excitations, electric charges and magnetic vortices, ($\nu = {\rm e}, {\rm m}$) that reside on vertices and plaquettes, respectively, of the square lattice. The excitation operators are defined with

$$h_v^e = \prod_{j \in v} \sigma_j^z, \quad h_p^m = \prod_{j \in p} \sigma_j^x, \quad \Sigma_i^{e,m} = \sigma_i^{x,z}. \tag{6.25}$$

Each link must interact with four ancillary pseudospins in the limit $T \ll \chi$ or $\chi \ll g$ to allow thermalization to the ground state or the thermal state of H_0^{TC}, respectively.

The stroboscopic generation of $H_{\rm TC}$ outlined above introduces truncation perturbations in the perturbative expansion, e.g, the second term in Eq. (6.3), which are distinct from

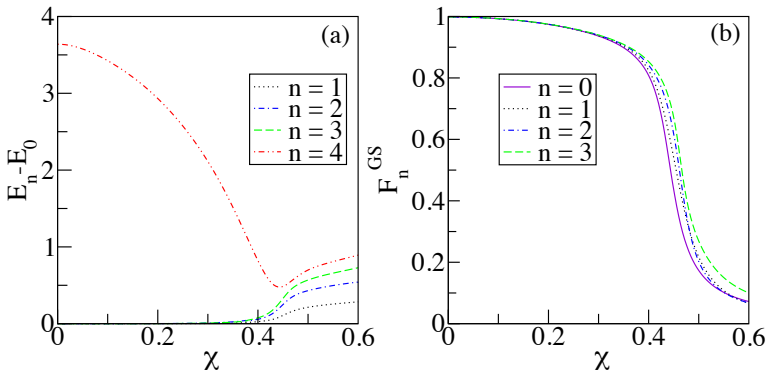

Figure 6.5: (a) Energy spectrum (in units of $J_e = J_m$) and (b) ground state fidelity vs. perturbation strength from exact diagonalization of the 18 site toric code with $h_z = 0.05$.

extrinsic errors due to experimental noise and gate inaccuracies. If sufficiently large, such truncation perturbations could drive the system away from the desired ground state phase. We now show on a finite sized system accessible to current experiments [91], that the intrinsic perturbations can be kept sufficiently small. Figure 6.5(a) plots the gap of

$$H^{TC}_{\chi,h_z} = H^{TC}_0 - h_z \sum_i \sigma^z_i + \chi \sum_{\langle i,j \rangle} \sigma^x_i \sigma^y_j$$

as a function of the strength of the perturbation for a 3×3 planar lattice with toroidal boundary conditions . The Zeeman field is added here to fully split the ground state degeneracy and ensure robust characterization of the eigenstates of H even in the presence of small additional perturbations. We define the ground state fidelity as

$$F^{GS}_n = |\langle \Psi^0_n | \Psi_n(\chi, h_z) \rangle|,$$

where the $|\Psi^0_n\rangle$ are the degenerate ground states of H^{TC}_0 and $|\Psi_n(\chi, h_z)\rangle$ are the nearly degenerate ground states of H^{TC}_{χ,h_z}. Fig. 6.5(b) shows the ground state fidelity as a function of χ. This fidelity determines the robustness of topological operations that will be performed via loop operators [64] to measure or perform gates on the system. We see that for $|\chi| \lesssim 0.4$ the features of the topological phase persist, including the approximate four-fold degeneracy of the ground state and a finite gap to excitations. This corresponds to a maximum value of $\phi \sim 0.4$, which constrains the gate operations in the pulse sequences, Eq. (6.2). This robustness should increase with increasing lattice size, and is consistent with known stability of H^{TC}_0 to perturbations [124].

Increasing ϕ increases J and therefore the gap of the H^{TC}_0; however it also increases χ/J, which reduce the gap of H^{TC}_{χ,h_z} and topological protection for large χ. We also note that $J \sim 1/N_G$ where N_G is the number of sequential gates used to simulate H. For larger lattices, some degree of parallelization is thus desirable to ensure that the gap does not decrease with

the lattice size. Choosing $\chi = 0.2$, the gap achieved by a completely serial implementation is $\Delta \approx 0.6\ \mu\mathrm{K}/N_{\mathrm{sys}}$, where N_{sys} is the number of system atoms used. With the cooling sequence serially interleaved, $\Delta \approx 0.1\ \mu\mathrm{K}/N_{\mathrm{sys}}$ and $\lambda^* \sim 10^4\ \mathrm{s}^{-1}/N_{\mathrm{sys}}$ are achievable. For a minimal system of 18 system atoms, this allows for an effective temperature $T_{\mathrm{eff}} < \Delta$ to be reached with an error rate of EPG $\sim 10^{-4}$ or less.

6.5 Sources of Errors

This scheme is designed to be robust against errors within the pseudospin subspace. The dominant source of residual error in the implementation discussed here is leakage from the Rydberg levels due to spontaneous emission and black body radiation. The latter may be effectively suppressed by working at low temperatures [51], and spontaneous emission is minimized by utilizing states with larger n. With $n \lesssim 180$, we estimate that spontaneous emission errors can be reduced to $\sim 10^{-6}$ per gate, allowing for up to 10^3 stroboscopic cycles.

6.6 Outlook

Although all of the experimental capabilities relied on for the above scheme are not yet available in current optical lattice experiments, the required technologies are rapidly developing [91]. It is possible that the minimal requirements for the generation of toric code Hamiltonian may be available in the near future. In particular the Weiss group at Penn State is currently developing the experimental capabilities required, and is planning on implementing this scheme [91]. While the cooling and thermalization procedure is even more experimentally challenging, it is possible that a simplified scheme using 2-body interactions may be used instead of the more complicated scheme presented here.

This general approach may be applied to other stabilizer-like Hamiltonians with commuting local terms. In particular, the toric code may be generalized to other Hamiltonians have a non-Abelian topologically ordered ground state [16, 64], including models that are universal for quantum computation [85, 86]. While the non-Abelian toric code Hamiltonian has much more complex interactions, they are still 4-body terms that commute; therefore, in principle this stroboscopic approach described here may be used to generate the non-Abelian toric code. An robust experimental realization of the non-Abelian toric code could potentially act as the basis of a universal fault tolerant quantum computer.

An outstanding question is to what extent cooling and thermalization of non-stabilizer-like Hamiltonians is possible via this approach. In general, we expect translationally invariant Hamiltonians to have propagating modes, and it is not clear under what conditions purely local system-bath interactions, which are accessible in this method, can be used to stabilize the ground state or a thermal state of a general interacting model. We are currently attempting to determine the conditions under which generic Hamiltonians may be thermally

stabilized [8].

Bibliography

[1] A. Albuquerque, Helmut Katzgraber, Matthias Troyer, and Gianni Blatter. Engineering exotic phases for topologically protected quantum computation by emulating quantum dimer models. *Physical Review B*, 78(1):014503, July 2008.

[2] R Alicki, M Fannes, and M Horodecki. A statistical mechanics view on Kitaev's proposal for quantum memories. *Journal of Physics A: Mathematical and Theoretical*, 40(24):6451–6467, June 2007.

[3] R Alicki, M Fannes, and M Horodecki. On thermalization in Kitaev's 2D model. *Journal of Physics A: Mathematical and Theoretical*, 42(6):065303, February 2009.

[4] Vinay Ambegaokar and Matthias Troyer. Estimating errors reliably in Monte Carlo simulations of the Ehrenfest model. *American Journal of Physics*, 78(2):150, 2010.

[5] P. W. Anderson. Resonating valence bonds: A new kind of insulator? *Materials Research Bulletin*, 8(2):153–160, February 1973.

[6] P W Anderson. The Resonating Valence Bond State in La2CuO4 and Superconductivity. *Science (New York, N.Y.)*, 235(4793):1196–8, March 1987.

[7] E Ardonne, P Fendley, and E Fradkin. Topological order and conformal quantum critical points. *Annals of Physics*, 310(2):493–551, April 2004.

[8] Jon Aytac, C. M. Herdman, Mohan Sarovar, K. C. Young, and K. B. Whaley. Conditons for thermal equilibration of many-body systems via local system-bath interactions. 2011.

[9] L. Balents, M. P. A. Fisher, and S. M. Girvin. Fractionalization in an easy-axis Kagome antiferromagnet. *Physical Review B*, 65(22):224412, May 2002.

[10] Stefano Baroni and Saverio Moroni. Reptation Quantum Monte Carlo: A Method for Unbiased Ground-State Averages and Imaginary-Time Correlations. *Physical Review Letters*, 82(24):4745–4748, June 1999.

[11] R. Baxter. Exact Isotherm for the F Model in Direct and Staggered Electric Fields. *Physical Review B*, 1(5):2199–2202, March 1970.

[12] T. Beals, J. Vala, and K. Whaley. Scalability of quantum computation with addressable optical lattices. *Physical Review A*, 77(5):052309, May 2008.

[13] Kurt Binder and Dieter W. Heermann. *Monte Carlo Simulation in Statistical Physics: An Introduction*. Springer, 2010.

[14] H. Blöte and B. Nienhuis. Fully packed loop model on the honeycomb lattice. *Physical Review Letters*, 72(9):1372–1375, February 1994.

[15] S. B. Bravyi and A. Yu. Kitaev. Quantum codes on a lattice with boundary. *arXiv:quant-ph/9811052v1*, 1998.

[16] G K Brennen, M Aguado, and J I Cirac. Simulations of quantum double models. *New Journal of Physics*, 11(5):053009, 2009.

[17] Kenneth Brown. Energy protection arguments fail in the interaction picture. *Physical Review A*, 76(2):022327, August 2007.

[18] H. P. Büchler, A. Micheli, and P. Zoller. Three-body interactions with cold polar-molecules. *Nature Physics*, 3(10):726–731, July 2007.

[19] Claudio Castelnovo and Claudio Chamon. Entanglement and topological entropy of the toric code at finite temperature. *Physical Review B*, 76(18):184442, 2007.

[20] Claudio Castelnovo, Claudio Chamon, Christopher Mudry, and Pierre Pujol. From quantum mechanics to classical statistical physics, Generalized Rokhsar Kivelson Hamiltonians and the Stochastic Matrix Form decomposition. *Annals of Physics*, 318(2):316–344, August 2005.

[21] D. M. Ceperley. Path integrals in the theory of condensed helium. *Reviews of Modern Physics*, 67(2):279–355, April 1995.

[22] David Ceperley and Berni Alder. Quantum monte carlo. *Science (New York, N.Y.)*, 231(4738):555–60, February 1986.

[23] Eric Dennis, Alexei Kitaev, Andrew Landahl, and John Preskill. Topological quantum memory. *Journal of Mathematical Physics*, 43(9):4452, 2002.

[24] S. Diehl, A. Micheli, A. Kantian, B. Kraus, H. P. Büchler, and P. Zoller. Quantum states and phases in driven open quantum systems with cold atoms. *Nature Physics*, 4(11):878–883, September 2008.

[25] Chengxiang Ding, Youjin Deng, Wenan Guo, Xiaofeng Qian, and Henk W J Blöte. Geometric properties of two-dimensional O(n) loop configurations. *Journal of Physics A: Mathematical and Theoretical*, 40(13):3305–3317, March 2007.

[26] E Domany, D Mukamel, B Nienhuis, and A Schwimmer. Duality relations and equivalences for models with O (N) and cubic symmetry. *Nuclear Physics B*, 190(2):279–287, 1981.

[27] B. Duplantier and H. Saleur. Exact Fractal Dimernsion of 2D Ising Clusters. *Physical Review Letters*, 63(22):2536–2536, 1989.

[28] H. G. Evertz. The loop algorithm. *Advances in Physics*, 52(1):1–66, January 2003.

[29] P. Fazekas and P. W. Anderson. On the ground state properties of the anisotropic triangular antiferromagnet. *Philosophical Magazine*, 30(2):423–440, August 1974.

[30] P Fendley. Topological order from quantum loops and nets. *Annals of Physics*, 323(12):3113–3136, December 2008.

[31] P. Fendley, R. Moessner, and S. Sondhi. Classical dimers on the triangular lattice. *Physical Review B*, 66(21):214513, December 2002.

[32] Paul Fendley and Eduardo Fradkin. Realizing non-Abelian statistics in time-reversal-invariant systems. *Physical Review B*, 72(2):024412, July 2005.

[33] Michael Fisher. Statistical Mechanics of Dimers on a Plane Lattice. *Physical Review*, 124(6):1664–1672, December 1961.

[34] Michael Fisher and John Stephenson. Statistical Mechanics of Dimers on a Plane Lattice. II. Dimer Correlations and Monomers. *Physical Review*, 132(4):1411–1431, November 1963.

[35] Michael E. Fisher. On the dimer solution of planar Ising models. *Journal of Mathematical Physics*, 7(10):1776, 1966.

[36] E. Fradkin and S. Kivelson. Short Range Resonating Valence Bond Theories and Superconductivity. *Mod. Phys. Lett. B.*, 4(3):225–232, 1990.

[37] Eduardo Fradkin. *Field Theories of Condensed Matter Systems (Advanced Books Classics) (v. 82)*. Westview Press, 1998.

[38] Eduardo Fradkin and Stephen Shenker. Phase diagrams of lattice gauge theories with Higgs fields. *Physical Review D*, 19(12):3682–3697, June 1979.

[39] M Freedman, Chetan Nayak, Kirill Shtengel, Kevin Walker, and Zhenghan Wang. A class of P,T-invariant topological phases of interacting electrons. *Annals of Physics*, 310(2):428–492, April 2004.

[40] Michael Freedman, Chetan Nayak, and Kirill Shtengel. Extended Hubbard Model with Ring Exchange: A Route to a Non-Abelian Topological Phase. *Physical Review Letters*, 94(6):066401, February 2005.

[41] Michael Freedman, Chetan Nayak, and Kirill Shtengel. Line of Critical Points in 2+1 Dimensions: Quantum Critical Loop Gases and Non-Abelian Gauge Theory. *Physical Review Letters*, 94(14):147205, 2005.

[42] Michael H. Freedman. Quantum Computation and the Localization of Modular Functors. *Foundations of Computational Mathematics*, 1(2):183–204, June 2001.

[43] Michael H. Freedman, Michael Larsen, and Zhenghan Wang. A Modular Functor Which is Universal for Quantum Computation. *Communications in Mathematical Physics*, 227(3):605–622, June 2002.

[44] Markus Greiner, Olaf Mandel, Tilman Esslinger, Theodor W Hänsch, and Immanuel Bloch. Quantum phase transition from a superfluid to a Mott insulator in a gas of ultracold atoms. *Nature*, 415(6867):39–44, January 2002.

[45] Matthew B. Hastings, Iván González, Ann B. Kallin, and Roger G. Melko. Measuring Renyi Entanglement Entropy in Quantum Monte Carlo Simulations. *Physical Review Letters*, 104(15):157201, April 2010.

[46] Patrik Henelius, S. Girvin, and Anders Sandvik. Role of winding numbers in quantum Monte Carlo simulations. *Physical Review B*, 57(21):13382–13385, June 1998.

[47] C L Henley. From classical to quantum dynamics at Rokhsar Kivelson points. *Journal of Physics: Condensed Matter*, 16(11):S891–S898, March 2004.

[48] Christopher L Henley. Relaxation time for a dimer covering with height representation. *Journal of Statistical Physics*, 89(3-4):483–507, November 1997.

[49] C M Herdman and K B Whaley. Loop condensation in the triangular lattice quantum dimer model. *New Journal of Physics*, 13(8):085001, August 2011.

[50] C M Herdman, Kevin C Young, V W Scarola, Mohan Sarovar, and K B Whaley. Stroboscopic Generation of Topological Protection. *Physical Review Letters*, 104(23):230501, June 2010.

[51] E. Hessels, D. Homan, and M. Cavagnero. Two-stage Rydberg charge exchange: An efficient method for production of antihydrogen. *Physical Review A*, 57(3):1668–1671, March 1998.

[52] L B Ioffe, M V Feigel'man, A Ioselevich, D Ivanov, M Troyer, and G Blatter. Topologically protected quantum bits using Josephson junction arrays. *Nature*, 415(6871):503–6, January 2002.

[53] A. Ioselevich, D. Ivanov, and M. Feigelman. Ground-state properties of the Rokhsar-Kivelson dimer model on the triangular lattice. *Physical Review B*, 66(17):174405, November 2002.

[54] S. Isakov, Yong Kim, and A. Paramekanti. Spin-Liquid Phase in a Spin-1/2 Quantum Magnet on the Kagome Lattice. *Physical Review Letters*, 97(20):207204, November 2006.

[55] Sergei Isakov, Arun Paramekanti, and Yong Kim. Exotic phase diagram of a cluster charging model of bosons on the kagome lattice. *Physical Review B*, 76(22):224431, 2007.

[56] Sergei V. Isakov, Matthew B. Hastings, and Roger G. Melko. Topological entanglement entropy of a Bose Hubbard spin liquid. *Nature Physics*, 7(10):772–775, July 2011.

[57] D. Ivanov. Vortexlike elementary excitations in the Rokhsar-Kivelson dimer model on the triangular lattice. *Physical Review B*, 70(9):094430, 2004.

[58] J.L. Jacobsen and J. Kondev. Field theory of compact polymers on the square lattice. *Nuclear Physics B*, 532(3):635–688, November 1998.

[59] D Jaksch, J. I. Cirac, P Zoller, R. Côté, and M. D. Lukin. Fast Quantum Gates for Neutral Atoms. *Physical Review Letters*, 85(10):2208–2211, September 2000.

[60] PW Kasteleyn. The statistics of dimers on a lattice:: I. The number of dimer arrangements on a quadratic lattice. *Physica*, 27:1209–1225, 1961.

[61] PW Kasteleyn. Dimer statistics and phase transitions. *Journal of Mathematical Physics*, 4(2):287, 1963.

[62] Naoki Kawashima and Kenji Harada. Recent Developments of World-Line Monte Carlo Methods. *Journal of the Physics Society Japan*, 73(6):1379–1414, June 2004.

[63] Joel Keizer. On the solutions and the steady states of a master equation. *J. Stat. Phys.*, 6(2-3):67–72, 1972.

[64] Alexei Kitaev. Fault-tolerant quantum computation by anyons. *Annals of Physics*, 303(1):2–30, January 2003.

[65] Alexei Kitaev and John Preskill. Topological Entanglement Entropy. *Physical Review Letters*, 96(11):110404, 2006.

[66] Steven Kivelson, Daniel Rokhsar, and James Sethna. Topology of the resonating valence-bond state: Solitons and high-T_{c} superconductivity. *Physical Review B*, 35(16):8865–8868, June 1987.

[67] S. Klarsfeld and J. Oteo. Recursive generation of higher-order terms in the Magnus expansion. *Physical Review A*, 39(7):3270–3273, April 1989.

[68] Yolanda M M Knops, Bernard Nienhuis, and Henk W J Blöte. The O model on the triangular lattice. *Journal of Physics A: Mathematical and General*, 31(13):2941–2966, April 1998.

[69] John B. Kogut. An introduction to lattice gauge theory and spin systems. *Reviews of Modern Physics*, 51(4):659–713, October 1979.

[70] Mahito Kohmoto. Resonating-valence-bond state: Comments on the antiferromagnetic ordering of the two-dimensional Heisenberg model. *Physical Review B*, 37(7):3812–3814, March 1988.

[71] Mahito Kohmoto and Yonathan Shapir. Antiferromagnetic correlations of the resonating-valence-bond state. *Physical Review B*, 37(16):9439–9442, June 1988.

[72] J Kondev and C.L. Henley. Kac-Moody symmetries of critical ground states. *Nuclear Physics B*, 464(3):540–575, April 1996.

[73] Jané Kondev. Liouville Field Theory of Fluctuating Loops. *Physical Review Letters*, 78(23):4320–4323, June 1997.

[74] Jané Kondev, Jan de Gier, and Bernard Nienhuis. Operator spectrum and exact exponents of the fully packed loop model. *Journal of Physics A: Mathematical and General*, 29(20):6489–6504, October 1996.

[75] Jané Kondev and Christopher Henley. Geometrical Exponents of Contour Loops on Random Gaussian Surfaces. *Physical Review Letters*, 74(23):4580–4583, June 1995.

[76] B. Kraus, H. Büchler, S. Diehl, A. Kantian, A. Micheli, and P. Zoller. Preparation of entangled states by quantum Markov processes. *Physical Review A*, 78(4):1–9, 2008.

[77] PW Leung, KC Chiu, and Karl Runge. Columnar dimer and plaquette resonating-valence-bond orders in the quantum dimer model. *Physical Review B*, 54(18):12938–12945, November 1996.

[78] Michael Levin and Xiao-Gang Wen. String-net condensation: A physical mechanism for topological phases. *Physical Review B*, 71(4):045110, January 2005.

[79] Michael Levin and Xiao-Gang Wen. Detecting Topological Order in a Ground State Wave Function. *Physical Review Letters*, 96(11):3–6, 2006.

[80] M. Lewenstein, A. Sanpera, V. Ahufinger, B. Damski, A. Sen, and U. Sen. Ultracold atomic gases in optical lattices: mimicking condensed matter physics and beyond. *Advances in Physics*, 56(2):243–379, 2007.

[81] Seth Lloyd, Benjamin Rahn, and Charlene Ahn. Robust quantum computation by simulation. *arXiv:quant-ph/9912040v1*, 1999.

[82] Roger Melko, Ann Kallin, and Matthew Hastings. Finite-size scaling of mutual information in Monte Carlo simulations: Application to the spin-1/2 XXZ model. *Physical Review B*, 82(10):100409, September 2010.

[83] Nicholas Metropolis, Arianna W. Rosenbluth, Marshall N. Rosenbluth, Augusta H. Teller, and Edward Teller. Equation of State Calculations by Fast Computing Machines. *The Journal of Chemical Physics*, 21(6):1087, February 1953.

[84] Grégoire Misguich and Frédéric Mila. Quantum dimer model on the triangular lattice: Semiclassical and variational approaches to vison dispersion and condensation. *Physical Review B*, 77(13):134421, 2008.

[85] Carlos Mochon. Anyons from nonsolvable finite groups are sufficient for universal quantum computation. *Physical Review A*, 67(2):022315, 2003.

[86] Carlos Mochon. Anyon computers with smaller groups. *Physical Review A*, 69(3):032306, 2004.

[87] R. Moessner and K. S. Raman. Quantum dimer models. *arXiv:0809.3051v1*, 2008.

[88] R. Moessner, S. Sondhi, and Eduardo Fradkin. Short-ranged resonating valence bond physics, quantum dimer models, and Ising gauge theories. *Physical Review B*, 65(2):024504, 2001.

[89] R. Moessner and S. L. Sondhi. Resonating Valence Bond Phase in the Triangular Lattice Quantum Dimer Model. *Physical Review Letters*, 86(9):1881–1884, February 2001.

[90] Chetan Nayak, Ady Stern, Michael Freedman, and Sankar Das Sarma. Non-Abelian anyons and topological quantum computation. *Reviews of Modern Physics*, 80(3):1083–1159, September 2008.

[91] Karl D. Nelson, Xiao Li, and David S. Weiss. Imaging single atoms in a three-dimensional array. *Nature Physics*, 3(8):556–560, June 2007.

[92] E Neufeld. *The Quantum Dimer Model on the Triangular Lattice - A Monte Carlo Study*. Master's thesis, ETH Zurich, 2004.

[93] Michael A. Nielsen and Isaac L. Chuang. *Quantum Computation and Quantum Information*. Cambridge University Press; 10 Anv edition, 2011.

[94] Bernard Nienhuis. Exact Critical Point and Critical Exponents of O(n) Models in Two Dimensions. *Physical Review Letters*, 49(15):1062–1065, October 1982.

[95] Bernard Nienhuis. Critical behavior of two-dimensional spin models and charge asymmetry in the Coulomb gas. *Journal of Statistical Physics*, 34(5-6):731–761, March 1984.

[96] Zohar Nussinov and Gerardo Ortiz. Autocorrelations and thermal fragility of anyonic loops in topologically quantum ordered systems. *Physical Review B*, 77(6):064302, 2008.

[97] Zohar Nussinov and Gerardo Ortiz. A symmetry principle for topological quantum order. *Annals of Physics*, 324(5):977–1057, 2009.

[98] J. Preskill. Reliable quantum computers. *Proceedings of the Royal Society A: Mathematical, Physical and Engineering Sciences*, 454(1969):385–410, January 1998.

[99] John Preskill. Battling decoherence: the fault-tolerant quantum computer. *Physics Today*, 52(6):24–32, 1999.

[100] N. V. Prokofev, B. V. Svistunov, and I. S. Tupitsyn. Exact, complete, and universal continuous time worldline Monte Carlo approach to the statistics of discrete quantum systems. *Journal of Experimental and Theoretical Physics*, 87(2):310–321, August 1998.

[101] R. Raghavan, Christopher L. Henley, and Scott L. Arouh. New two-color dimer models with critical ground states. *Journal of Statistical Physics*, 86(3-4):517–550, February 1997.

[102] A. Ralko, D. Poilblanc, and R. Moessner. Generic Mixed Columnar-Plaquette Phases in Rokhsar-Kivelson Models. *Physical Review Letters*, 100(3):037201, January 2008.

[103] Arnaud Ralko, Michel Ferrero, Federico Becca, Dmitri Ivanov, and Frédéric Mila. Zero-temperature properties of the quantum dimer model on the triangular lattice. *Physical Review B*, 71(22):224109, 2005.

[104] Arnaud Ralko, Michel Ferrero, Federico Becca, Dmitri Ivanov, and Frédéric Mila. Dynamics of the quantum dimer model on the triangular lattice: Soft modes and local resonating valence-bond correlations. *Physical Review B*, 74(13):134301, 2006.

[105] Arnaud Ralko, Michel Ferrero, Federico Becca, Dmitri Ivanov, and Frédéric Mila. Crystallization of the resonating valence bond liquid as vortex condensation. *Physical Review B*, 76(14):140404, 2007.

[106] Daniel S. Rokhsar and Steven A. Kivelson. Superconductivity and the Quantum Hard-Core Dimer Gas. *Physical Review Letters*, 61(20):2376–2379, November 1988.

[107] H. Saleur and B. Duplantier. Exact Determination of the Percolation Hull Exponent in Two Dimensions. *Physical Review Letters*, 58(22):2325–2328, June 1987.

[108] Anders Sandvik and Juhani Kurkijärvi. Quantum Monte Carlo simulation method for spin systems. *Physical Review B*, 43(7):5950–5961, March 1991.

[109] Anders Sandvik and R. Moessner. Correlations and confinement in nonplanar two-dimensional dimer models. *Physical Review B*, 73(14):144504, April 2006.

[110] A. Sarsa, K. E. Schmidt, and W. R. Magro. A path integral ground state method. *The Journal of Chemical Physics*, 113(4):1366, 2000.

[111] Yonathan Shapir and Mahito Kohmoto. Exact mapping of the resonant-valence-bond state to a classical O(4) model in a logarithmic potential: Mean-field theory, magnetic correlations, and excitations. *Physical Review B*, 39(7):4524–4530, March 1989.

[112] D. Sheng and Leon Balents. Numerical Evidences of Fractionalization in an Easy-Axis Two-Spin Heisenberg Antiferromagnet. *Physical Review Letters*, 94(14):146805, 2005.

[113] Peter W. Shor. Polynomial-Time Algorithms for Prime Factorization and Discrete Logarithms on a Quantum Computer. *SIAM Review*, 41(2):303, 1999.

[114] I. Spielman, W. Phillips, and J. Porto. Condensate Fraction in a 2D Bose Gas Measured across the Mott-Insulator Transition. *Physical Review Letters*, 100(12):1–4, March 2008.

[115] B Sutherland. Novel mechanism for superconductivity in the resonanting-valence-bond ground state. *Physical Review B*, 38(10):7192–7195, 1988.

[116] Bill Sutherland. Monte Carlo investigation of the resonating-valence-bond ground state and a lattice statistical model. *Physical Review B*, 38(10):6855–6862, October 1988.

[117] Bill Sutherland. Systems with resonating-valence-bond ground states: Correlations and excitations. *Physical Review B*, 37(7):3786–3789, March 1988.

[118] Masuo Suzuki. Generalized Trotter's formula and systematic approximants of exponential operators and inner derivations with applications to many-body problems. *Communications in Mathematical Physics*, 51(2):183–190, June 1976.

[119] Masuo Suzuki, Seiji Miyashita, and Akira Kuroda. Monte Carlo Simulation of Quantum Spin Systems. I. *Progress of Theoretical Physics*, 58(5):1377–1387, November 1977.

[120] Olav Syljuåsen. Continuous-time diffusion Monte Carlo method applied to the quantum dimer model. *Physical Review B*, 71(2):020401, January 2005.

[121] Olav Syljuåsen. Plaquette phase of the square-lattice quantum dimer model: Quantum Monte Carlo calculations. *Physical Review B*, 73(24):245105, June 2006.

[122] Olav Syljuåsen and M. Zvonarev. Directed-loop Monte Carlo simulations of vertex models. *Physical Review E*, 70(1):016118, July 2004.

[123] Olav F. Syljuåsen and Anders W. Sandvik. Quantum Monte Carlo with directed loops. *Physical Review E*, 66(4):046701, October 2002.

[124] Simon Trebst, Philipp Werner, Matthias Troyer, Kirill Shtengel, and Chetan Nayak. Breakdown of a Topological Phase: Quantum Phase Transition in a Loop Gas Model with Tension. *Physical Review Letters*, 98(7):070602, February 2007.

[125] Nandini Trivedi and D. Ceperley. Green-function Monte Carlo study of quantum antiferromagnets. *Physical Review B*, 40(4):2737–2740, August 1989.

[126] F. Trousselet, P. Pujol, F. Alet, and D. Poilblanc. Criticality of a classical dimer model on the triangular lattice. *Physical Review E*, 76(4):041125, 2007.

[127] Matthias Troyer. Non-local Updates for Quantum Monte Carlo Simulations. In *AIP Conference Proceedings*, volume 690, pages 156–169. AIP, 2003.

[128] Matthias Troyer, Simon Trebst, Kirill Shtengel, and Chetan Nayak. Local Interactions and Non-Abelian Quantum Loop Gases. *Physical Review Letters*, 101(23):230401, 2008.

[129] J Villain, R. Bidaux, J.-P. Carton, and R Conte. Order as an effect of disorder. *Journal de Physique*, 41(11):1263–1272, 1980.

[130] Hendrik Weimer, Markus Müller, Igor Lesanovsky, Peter Zoller, and Hans Peter Büchler. A Rydberg quantum simulator. *Nature Physics*, 6(5):382–388, March 2010.

[131] D. Weiss. private communication, 2009.

[132] X.G. Wen. Topological Orders in Rigid States. *Int. J. Mod. Phys. B*, 4(2):239, 1990.

[133] D J Wineland, J C Bergquist, W M Itano, and R E Drullinger. Double-resonance and optical-pumping experiments on electromagnetically confined, laser-cooled ions. *Optics letters*, 5(6):245–7, June 1980.

[134] Jun Zhang, Jiri Vala, Shankar Sastry, and K. Whaley. Minimum Construction of Two-Qubit Quantum Operations. *Physical Review Letters*, 93(2):020502, July 2004.